NASA/TP–2017-219581

Experimental Study of Convective Heating on the Back Face and Payload of a Hypersonic Inflatable Aerodynamic Decelerator (HIAD) Aeroshell

Brian R. Hollis and Scott A. Berry
Langley Research Center, Hampton, Virginia

Kevin E. Hollingsworth and Shelia A. Wright
Jacobs Technology Inc., Hampton, Virginia

.

March 2017

NASA STI Program . . . in Profile

Since its founding, NASA has been dedicated to the advancement of aeronautics and space science. The NASA scientific and technical information (STI) program plays a key part in helping NASA maintain this important role.

The NASA STI program operates under the auspices of the Agency Chief Information Officer. It collects, organizes, provides for archiving, and disseminates NASA's STI. The NASA STI program provides access to the NTRS Registered and its public interface, the NASA Technical Reports Server, thus providing one of the largest collections of aeronautical and space science STI in the world. Results are published in both non-NASA channels and by NASA in the NASA STI Report Series, which includes the following report types:

- TECHNICAL PUBLICATION. Reports of completed research or a major significant phase of research that present the results of NASA Programs and include extensive data or theoretical analysis. Includes compilations of significant scientific and technical data and information deemed to be of continuing reference value. NASA counter-part of peer-reviewed formal professional papers but has less stringent limitations on manuscript length and extent of graphic presentations.
- TECHNICAL MEMORANDUM. Scientific and technical findings that are preliminary or of specialized interest, e.g., quick release reports, working papers, and bibliographies that contain minimal annotation. Does not contain extensive analysis.
- CONTRACTOR REPORT. Scientific and technical findings by NASA-sponsored contractors and grantees.
- CONFERENCE PUBLICATION. Collected papers from scientific and technical conferences, symposia, seminars, or other meetings sponsored or co-sponsored by NASA.
- SPECIAL PUBLICATION. Scientific, technical, or historical information from NASA programs, projects, and missions, often concerned with subjects having substantial public interest.
- TECHNICAL TRANSLATION. English-language translations of foreign scientific and technical material pertinent to NASA's mission.

Specialized services also include organizing and publishing research results, distributing specialized research announcements and feeds, providing information desk and personal search support, and enabling data exchange services.

For more information about the NASA STI program, see the following:

- Access the NASA STI program home page at http://www.sti.nasa.gov
- E-mail your question to help@sti.nasa.gov
- Phone the NASA STI Information Desk at 757-864-9658
- Write to:
  NASA STI Information Desk
  Mail Stop 148
  NASA Langley Research Center
  Hampton, VA 23681-2199

NASA/TP–2017-219581

Experimental Study of Convective Heating on the Back Face and Payload of a Hypersonic Inflatable Aerodynamic Decelerator (HIAD) Aeroshell

Brian R. Hollis and Scott A. Berry
Langley Research Center, Hampton, Virginia

Kevin E. Hollingsworth and Shelia A. Wright
Jacobs Technology Inc., Hampton, Virginia

National Aeronautics and
Space Administration

Langley Research Center
Hampton, Virginia 23681-2199

March 2017

Available from:

NASA STI Program / Mail Stop 148
NASA Langley Research Center
Hampton, VA 23681-2199
Fax: 757-864-6500

Table of Contents

List of Tables

List of Figures

Abstract

A wind tunnel test program has been conducted to define convective heating environments on the back-face of a Hypersonic Inflatable Aerodynamic Decelerator aeroshell. Wind tunnel testing was conducted at Mach 6 and Mach 10 at unit Reynolds numbers from 0.5×10^6*/ft to* 3.9×10^6*/ft on a 6.3088 in diameter aeroshell model. Global heating data were obtained through phosphor thermography on the aeroshell back face, as well as on the payload and the aeroshell front face. For all test conditions, laminar flow was produced on the aeroshell front face, while the separated wake shear layer and aeroshell back-face boundary layer were transitional or turbulent. Along the leeward centerline of the aeroshell back face and payload centerbody, heating levels increased with both free stream Reynolds number and angle of attack. The Reynolds number dependency was due to increasing strength of wake turbulence with Reynolds number. The angle-of-attack dependency was due to movement of the wake-vortex reattachment point on the aeroshell back face. The maximum heating levels on the aeroshell back face and payload were approximately 5% to 6%, respectively, of the aeroshell front-face stagnation point. To allow for extrapolation of the ground test data to flight conditions, the back face and payload heating levels were correlated as a function of aeroshell front-face peak momentum thickness Reynolds numbers.*

Nomenclature

Symbols

D	maximum diameter (in or m)
h	heat-transfer film coefficient (kg/m^2 · s)
h_{FR}	heat-transfer film coefficient based on Fay-Riddell theory (kg/m^2 · s)
h_{STAG}	heat-transfer film coefficient at stagnation point on nose (kg/m^2 · s)
H_0	wind tunnel total enthalpy (J/kg)
H_{AW}	adiabatic wall surface enthalpy (J/kg)
H_w	surface enthalpy (J/kg)
H_{300K}	enthalpy at 300 K temperature (J/kg)
M_∞	free stream Mach number
p_∞	free stream pressure (Pa)
q	heat transfer rate (W/cm^2)
r	radial coordinate (in or m)
R	maximum body radius (in or m)
Re_∞	free stream unit Reynolds number (1/ft or 1/m)
Re_θ	boundary-layer momentum thickness Reynolds number
T_∞	free stream temperature (K)
U_∞	free stream velocity (m/s)
U_e	boundary-layer edge velocity (m/s)
x, y, z	Cartesian coordinates (in or m)
α	angle of attack (deg)
ϕ	rotation angle (deg)

ρ_∞	free stream density (kg/m^3)
ρ_e	boundary-layer edge density (kg/m^3)
σ	standard deviation
θ	boundary-layer momentum thickness (m)
μ_∞	free stream viscosity (kg/m $\cdot$ s)
μ_e	boundary-layer edge viscosity (kg/m $\cdot$ s)

Subscripts

∞	free stream condition
0	reservoir condition
e	edge condition
FR	Fay-Riddell
sh	shoulder condition
w	wall condition

Acronyms

AGARD	Advisory Group for Aerospace Research and Development
CFD	Computational Fluid Dynamics
F-TPS	Flexible Thermal Protection System
HIAD	Hypersonic Inflatable Aerodynamic Decelerator
IHEAT	Imaging for Hypersonic Experimental Aerothermodynamic Testing
IRVE	Inflatable Reentry Vehicle Experiment
ISS	International Space Station
LAL	Langley Aerothermodynamic Laboratory
LaRC	Langley Research Center
LAURA	Langley Aerothermodynamic Upwind Relaxation Algorithm
MSL	Mars Science Laboratory
OML	Outer Mold Line
SLA	Stereo-Lithographic Apparatus
THOR	Terrestrial HIAD Orbital Reentry
TPS	Thermal Protection System

Introduction

An experimental study has been conducted to define the aeroheating environment of a Hypersonic Inflatable Aerodynamic Decelerator (HIAD) with a flexible thermal protection system (F-TPS). The primary goal of this study was to measure convective heating environments on the back face of the HIAD aeroshell. Additionally, heating data on the payload and front-face of the aeroshell were obtained. These data were generated through testing at Mach 6 and Mach 10 at the NASA Langley Research Center (LaRC) in hypersonic blow-down wind tunnels using global phosphor thermography.

The model geometry for this study was similar to NASA's proposed Terrestrial HIAD Orbital Reentry (THOR) mission. THOR was intended to fly as a secondary payload on a supply mission to the International Space Station (ISS), but the program was terminated due to issues unrelated to HIAD technology development. Although the THOR mission was cancelled, the results of this study are still of value to HIAD technology development. While back-face convective heating environments for blunt bodies such as the THOR aeroshell are generally benign (<10% of stagnation point levels), one of the design goals for any HIAD will be to minimize the F-TPS thickness on the back face in order to save weight and simplify packaging of the un-inflated aeroshell.

Background and Motivation

HIAD Technology Development

HIAD technology offers an effective, mass-saving alternative to conventional aerodynamic decelerators. Relative to a rigid TPS, a HIAD F-TPS has a lower mass and a smaller packaging volume, but when deployed and inflated it provides a large surface area for drag production, resulting in a lower ballistic coefficient than a rigid aeroshell of equivalent surface area. The lower ballistic coefficient of the HIAD results in lower heat fluxes and integrated heat loads, thus reducing the performance demands on the F-TPS material.

The inflatable aeroshell concept was first proposed in the 1960s and was then referred to as a “ballute”, from “balloon” + “parachute”. Since then, various inflatable configurations have been proposed and studied (e.g., Ref. 1) such as attached, trailing, tension cone, ram-inflated, etc. However, no successful hypersonic flight test had ever been conducted with an inflatable system until NASA initiated the Inflatable Reentry Vehicle Experiment (IRVE) test program to mature and validate this technology (Ref. 2).

The first IRVE flight test (Ref. 3) failed to exit the launch vehicle due to an anomaly unrelated to HIAD technology. A duplicate of this vehicle was commissioned and in 2009 the IRVE-II launch resulted in the first successful flight of a HIAD (Ref. 4). The IRVE-II flight test demonstrated exo-atmospheric inflation of the aeroshell and stable flight from hypersonic through subsonic speeds. However, because the IRVE-II vehicle was launched from a small sounding rocket, the aeroheating environment was quite benign. The maximum Mach number was ~5, which produced peak heat fluxes of only ~2 W/cm^2. Nevertheless, the success of IRVE-II provided the foundation for the next step in HIAD technology development, the IRVE-3 flight test[1].

The successful IRVE-3 flight test in 2012 was a direct follow-up to IRVE-II, with the overall goal of demonstrating HIAD performance and gathering flight data in a mission-relevant environment (Ref. 5). The primary requirement for IRVE-3 was to demonstrate F-TPS survivability during the hypersonic segment of the flight at heating levels an order-of-magnitude higher than IRVE-II, and so it was launched on a larger, three-stage sounding rocket to obtain greater entry velocity (maximum Mach 10). This objective was achieved with the vehicle reaching a peak heat flux of 15 W/cm^2 at a Mach number of 7.

The next HIAD flight test proposed by NASA was the THOR program (Ref. 6). Although this flight test was cancelled, it was intended to demonstrate the performance of an F-TPS capable of withstanding aerothermal environments relevant to a Mars human exploration mission or ISS down-mass return. For such missions, the heat flux could be a factor of 2 to 3 greater than

---

[1] Although the nomenclature for the flight test numbers differs, i.e., IRVE, IRVE-II and IRVE-3, these are the official designations.

IRVE-3 peak heat flux, and the integrated heat load could be a factor of 20 to 35 times greater than for IRVE-3. The THOR vehicle was intended to fly as a secondary payload on a resupply mission to the ISS and would have been deployed from the launch vehicle's second stage after the cargo carrier separated to proceed toward the ISS. The THOR reentry vehicle concept is shown in Figure 1.

Blunt Body Wake Flows

The motivation for this study was the lack of reliable data on blunt body wake flow fields and aftbody/back-face aeroheating environments. Several studies (e.g., Refs. 7–11) in the 1990s, coordinated or motivated by NATO's Advisory Group for Aerospace Research and Development (AGARD) Working Group 18, demonstrated the complex nature of hypersonic, blunt body wake flow fields through testing in multiple wind tunnels around the world. These features include unsteadiness, separation and impingement of shear/boundary layers, rarefaction, and turbulence (e.g. Figure 2).

Hypersonic, blunt body wake flows with large regions of separated flow challenge current capabilities for routine, validated simulations using Computational Fluid Dynamics (CFD) tools. Similarly, experimental measurements can be difficult due to the unsteady nature of the flow, the very low aftbody surface temperatures and pressures, and the lack of facilities capable of simulating actual flight conditions. As a result of these challenges, the aftbody TPS of reentry vehicles typically are designed with very high uncertainty margins. For instance, the Mars Science Laboratory (MSL) aftbody TPS design was based on a 200% uncertainty for heating and shear stress and a 100% uncertainty for pressure (Ref. 12).

For the current study of THOR aeroshell back-face heating environments, the decision was made to focus on experimental methods, rather than computational simulations. This decision was due to some of the unique features of HIAD systems as compared to typical reentry vehicles. The first is that a HIAD such as THOR would fly a less stressful trajectory with respect to heating due to the large aeroshell surface area and low mass of the vehicle. Thus, flight conditions would be closer to conditions achievable in ground-based facilities. The second is that a HIAD lacks the enclosed aftbody section such as that of the MSL vehicle. This open-back configuration of a HIAD aeroshell creates a large, concave region that greatly increases the challenges in developing a structured grid topology for numerical simulations.

Experimental Tools and Methods

Model Geometry and Fabrication

Model Geometry

The geometry for this test program, shown in Figure 3, was based on a preliminary THOR concept designated as THOR 70-F, which differed slightly (mainly in nose radius) from the final proposed THOR flight configuration. The THOR 70-F geometry was a 70-deg sphere-cone aeroshell with an open back face mounted on a cylindrical payload section. The overall wind tunnel model diameter was 6.3088 in, the nose radius was 0.75 in, and the shoulder radius was 0.0971 in. The wind tunnel model was 4.4% of the proposed full-scale flight vehicle size. The payload section was simplified to a 1.250 in diameter cylinder and was filleted at the junction to the aeroshell to provide additional strength. The geometry represented an idealized, rigid outer mold line without the deformations that could be produced due to in-flight aerodynamic loads acting on the inflatable aeroshell.

Model Fabrication

Ceramic wind tunnel models of the THOR 70-F geometry were fabricated following the process discussed in Ref. 13. First, a pattern was generated using a rapid-prototyping stereolithography apparatus (SLA). An investment mold was then constructed from the SLA pattern and cured. Next, a silica-ceramic slip casting was made from the mold and sintered at high temperature. Finally, the slip-cast ceramic model was fired at high temperature and coated with a thermographic phosphor compound. The ceramic models were then mounted on a stainless steel sting through the aft end of the payload section.

Test Facilities and Conditions

Wind Tunnel Test Conditions

Two wind tunnel tests were performed in the Langley Aerothermodynamics Laboratory (LAL) facilities in support of this program: a low unit Reynolds number test in the 31-Inch Mach 10 Air Tunnel and a high unit Reynolds number test in the 20-Inch Mach 6 Air Tunnel. These facilities are described in brief below, and more detailed information on the LAL can be found in Refs. 14 and 15. Data were obtained at Mach 10 for three unit Reynolds numbers from 0.5×10^6/ft to 2.0×10^6/ft and at Mach 6 for four unit Reynolds numbers from 1.0×10^6/ft to 3.9×10^6/ft. Angle of attack was varied from -10 deg to +10 deg depending on facility and Reynolds number. Owing to schedule and resource limitations, it was not possible to obtain data at all angles of attack for every unit Reynolds number condition.

Free stream conditions are listed in Table 1 for Test 504 in the 31-Inch Mach 10 Air Tunnel and in Table 2 for Test 7002 in the 20-Inch Mach 6 Air Tunnel. Entries in these tables are sorted by angle of attack and by free stream unit Reynolds number. The heat-transfer film coefficient (h_{FR}) values listed in these tables are based on Fay-Riddell (Ref. 16) calculations for the 0.75 in nose radius of the model at cold-wall (300 K) conditions. The enthalpy difference (ΔH_{tot}) is based on the difference between the free stream total enthalpy and the wall enthalpy at 300 K. The conditions listed in these tables are nominal values based on averages of all runs at a given condition. As the run-to-run variations in test conditions were very slight (~1%), all supporting analyses were performed using these nominal values.

NASA LaRC 31-Inch Mach 10 Air Tunnel

The NASA LaRC 31-Inch Mach 10 Air Tunnel (Figure 4 and Figure 5) is a perfect-gas, blowdown facility in which dried, filtered air is used as the working fluid. The tunnel has been calibrated for reservoir conditions varying from 150 psi to 1450 psi at an operating temperature of 1850°R, which produces free stream unit Reynolds numbers from 0.25×10^6/ft to 2.2×10^6/ft. The nozzle is water-cooled, has a three-dimensional contour, and ends with a 1.07×1.07 in square throat. The 31×31 in square test section features optical access through side, top, and bottom windows for visual imaging techniques and has a side-mounted injection system with a ±45 deg pitch range and ±5 deg yaw range. The test core varies from approximately 12×12 in at the lowest unit Reynolds number to 14×14 in at the highest unit Reynolds number. This tunnel has the highest Mach number of the LAL facilities and is mainly employed in aerodynamic and fluid-mechanics studies. The high stagnation temperature of the facility also makes it suitable for aftbody/wake heating studies where the temperature rise is much lower than on the forebody.

NASA LaRC 20-Inch Mach 6 Air Tunnel

The NASA LaRC 20-Inch Mach 6 Air Tunnel (Figure 6 and Figure 7) is a blow-down facility in which heated, dried, and filtered air is used as the test gas. The tunnel has a two-dimensional contoured nozzle that opens into a 20.5×20.0 in test section. The tunnel is equipped with a bottom-mounted injection system with a –5 deg to +55 deg pitch range and ±5 deg yaw range that can transfer a model from a sheltered model box to the tunnel centerline in less than 0.5 sec. Run times of up to 15 minutes are possible in this facility, although for the current aeroheating study run times of only a few seconds were required. The nominal reservoir conditions of this facility produce perfect-gas free stream flows with Mach numbers between 5.8 and 6.1 and unit Reynolds numbers of 0.5×10^6/ft to 8.3×10^6/ft. With the wide Reynolds number operating range capable of producing laminar, transitional, or turbulent flow on most geometries, this tunnel is primarily used for heat-transfer and boundary-layer transition studies.

Data Acquisition, Reduction, Uncertainty and Presentation

Data Acquisition

Aeroheating data were obtained using the two-color, relative-intensity, global thermographic phosphor method (Ref. 17) and reduced using the Imaging for Hypersonic Experimental Aerothermodynamic Testing (IHEAT) code (Ref. 18). In this method, a model is illuminated by ultraviolet light sources that produce temperature-dependent fluorescence of the phosphor coating. Images of the model are taken in the tunnel before and during a run using a three-color, charge-coupled device camera and the images are processed to determine temperature and heat-transfer distributions.

In order to obtain both front-face and back-face heating data, separate runs were made with the camera positioned ahead of and behind the model. However, because of the model geometry and optical access limits in the wind tunnels, it was not possible to view the entire model surface for either front or back camera setups. The camera view directions for both setups are illustrated in Figure 8 along with the x-y-z coordinate system and definitions for angle of attack (α) and rotation angle (ϕ) about the centerbody. For most cases, the lower side (relative to the camera) of the aeroshell front face was out of the camera's field of view and in back views, the lower part of the aeroshell back face was blocked by the centerbody payload section.

Data Reduction

The IHEAT code uses calibrations to convert the intensity data from each image pixel to temperatures. Heat-transfer film coefficients are then determined by assuming a step function in heat transfer beginning at injection of the model into the tunnel, which corresponds to a parabolic temperature-time history. Heat transfer data from IHEAT are typically reported in terms of the ratio h/h_{FR}, where h_{FR} is the heat-transfer film coefficient resulting from a Fay-Riddell computation for a reference hemisphere of specified radius (in this case, the 0.75 in radius of the nose). The heat-transfer film coefficient is defined in terms of enthalpy as

$$h = q/\Delta H_{tot} = q/\left(H_{AW} - H_{300K}\right) = q/\left(H_0 - H_{300K}\right) \tag{1}$$

In the calculation of the heat-transfer film coefficient, it is assumed that, for a blunt body, the adiabatic wall enthalpy H_{AW} is equal to the free stream total enthalpy of the tunnel, H_0. This heat transfer coefficient definition provides a theoretically near-constant value over the course of a run, since the decrease in time of the heat transfer rate in the numerator as the model surface becomes hotter is balanced by the decrease of the enthalpy term in the denominator.

The two-dimensional (2-D) image data obtained from IHEAT are corrected for optical perspective effects and mapped to a three-dimensional (3-D) surface representation of the model geometry. To accomplish this mapping, perspective, translational, and rotational transformations are first performed on the 3-D surface representation until its 2-D projection matches that of the 2-D image data. The image data are then assigned transformed (x, y, z) coordinates based on interpolation between the image and surface geometry and then the transformation is inverted to obtain an orthographic, 3-D heating distribution map. A sample 2-D image file from IHEAT, sample 3-D surface geometry, and the mapping of the image data onto the geometry are shown in Figure 9 through Figure 11.

Data Presentation

As noted in the Data Reduction section, the aeroshell front-face heating data will be presented in the usual manner for phosphor thermography studies in terms of h/h_{FR} where h_{FR} is the film coefficient based on Fay-Riddell theory for the nose radius of the model. However, a different representation, h/h_{STAG}, will also be employed for the back-face heating data. In order to provide better perspective on the relationship between aeroshell back-face and front-face heating levels, the back-face heating was normalized by h_{STAG} instead of h_{FR}. The value h_{STAG} is the predicted heating for the nose-cap at $\alpha = 0$ deg as determined from a Navier-Stokes solution (as detailed in the subsequent Computational Method section). For the THOR 70-F geometry, h_{STAG} is approximately 61% of h_{FR}. The difference between h_{STAG} and h_{FR} is due to the fact that Fay-Riddell theory is based on the idealized assumption of a stagnation-point pressure gradient for a hemisphere, while in fact, the pressure gradient at the nose of a large angle sphere-cone (where the boundary-layer edge Mach number is subsonic) differs from that of a true hemisphere. As will be shown subsequently, the measured and predicted nose-cap stagnation point heating levels were in close agreement.

Another difference in the presentation of front-face and back-face aeroshell heating data is the use of locally-weighted, least-square fits to better characterize the back-face data. As noted previously, the back-face measurements showed much more scatter than front-face measurements owing to the very low temperature rise of the back face. To develop these curve fits, data were extracted from the 3-D mapped global images along the $\phi = 10$ deg increment rays over the aeroshell back face (as was defined in Figure 8). For $\alpha = 0$ deg angle-of-attack cases, the fits were determined using all rays since the distributions were (nominally) axisymmetric. For the nonzero angle of attack cases, the curve fits were generated using the data from the –20 deg through +20 deg rays, which represents an approximate average of data on the leeward centerline of the aeroshell back face, i.e., along the +*z*-axis. Note that the stagnation point on the aeroshell front face moved away from the nosetip ($z = 0$) in the $-z$ (windward) direction with increasing angle of attack. These curve fits will be shown along with the measured data points for each condition.

Centerbody payload heating data will be presented in the same manner as the aeroshell back-face data. For the payload, the heating analysis is based on averaging the data over a spanwise region of $y = \pm 25\%$ of the centerbody radius at each *x*-location.

Data Uncertainty

The experimental uncertainty of front-face and back-face aeroshell heating data must be characterized separately due to the large differences in flow field characteristics between the two regions. The flow field over the front fac of the aeroshell was steady and, for these test conditions, laminar. Additionally, the temperature rise over the duration of each run was large (25–75 K at Mach 6 conditions and 50–100 K at Mach 10 conditions) thus providing a very high signal-to-noise ratio for the measurement. These aeroshell front-face conditions were well within the standard range of application of the phosphor thermography system (see Ref. 18) for which the uncertainty has been characterized in previous studies. The only issue with the aeroshell front-face data is that for the highest unit Reynolds number condition in the Mach 10 tunnel (Test 504, Run 8 at $\mathrm{Re}_{\infty} = 2.0\times10^{6}/\mathrm{ft}$), temperature levels on the nose exceeded the calibration range of the phosphor thermography system and thus no usable data were obtained there.

For the measurements on the front face of the aeroshell, the experimental uncertainty for heating was estimated from a root-sum-square calculation of the component uncertainties due to the data acquisition method (±10%), the flow quality and test-condition repeatability (±5%), and the accuracy of the 3-D mapping process (±10%), which resulted in an overall value of ±15%. Experience with this technique indicates that these values are usually conservative and, as will be shown later, the predicted and measured heating distributions on the front face of the aeroshell were in closer agreement than the uncertainty estimate.

Because of the complexity of blunt body wake flow fields, the determination of heating rates on the back face of a vehicle through either measurement or simulation is very challenging. In the previous AGARD-18 studies (Refs. 7–11), it was shown that blunt body wake flow fields typically are characterized by large regions of separated flow that are likely to be both unsteady and turbulent. As such, the invariance with Reynolds number of normalized heating rates expected for attached forebody flows will not be present for wake flows. This behavior was demonstrated by data (Ref. 8) from the AGARD WG-18 aeroshell geometry (Figure 12). Normalized heating distributions on the forebody (Figure 13) were essentially constant with Reynolds numbers, while distributions on the sting (Figure 13) and aeroshell back face (Figure 13 and close-up in Figure 14) increased with Reynolds number.

Additionally, heating rates on the back side of blunt bodies are typically less than 10% of those on the front of the vehicle, which results in a very low temperature rise (less than 10 K for the current study, as shown in Table 3) and thus low signal-to-noise ratios. For such low temperatures, the optical signal intensity from the phosphor emission is very low, leading to a much higher uncertainty than for forebody flows. In the plots of estimated uncertainty vs.

surface temperature given in Ref. 18, the curves are nearly asymptotic for the temperature range on the aeroshell back face in this study and thus cannot be used as a basis for uncertainty estimates.

Although the aeroshell back-face heating measurement uncertainty was expected to be very high, analysis of the data showed reasonably consistent results for the effects of Reynolds number and angle of attack. Therefore, in lieu of a theoretical basis for uncertainty estimates, the uncertainty was based on a statistical analysis of the scatter of the data, as follows:

For each of the 0 deg angle-of-attack, back-view runs in the Mach 6 and Mach 10 tunnels, data were extracted along radial lines at ϕ = 10 deg increments around the circumference of the model (see Figure 8) providing a data set of approximately 600 to 800 points per image. Standard deviations (σ) were then computed for selected radial (r/R) locations. Additionally, weighted, least-square curve fits were generated for the aeroshell back-face heating distributions. Comparisons between the complete sets of data points and the curve fits are shown for the Mach 10 conditions in Figure 15 through Figure 17 and for the Mach 6 conditions in Figure 18 through Figure 21. For each case, these comparisons are shown with uncertainty error bars of $1\times\sigma$ and $3\times\sigma$. In all cases, after obvious outlier points (due to coating scratches or null signal points) were eliminated, almost all data points fell within the $3\times\sigma$ band. Thus, depending on the level of conservatism desired, the curve fits can be used in conjunction with either the $1\times\sigma$ or $3\times\sigma$ uncertainty bounds, which are listed in Table 4, to estimate back-face heating levels.

Also, an alternative weighted uncertainty formulation was determined by normalizing the standard deviation by the average heating levels on the aeroshell back-face to obtain $(1\times\sigma)/(h/h_{\mathrm{STAG}})$ and $(3\times\sigma)/(h/h_{\mathrm{STAG}})$. These values are also provided in Table 4.

The overall average $1\times\sigma$ and $3\times\sigma$ uncertainty levels for the standard deviation were 0.0059 and 0.0178, respectively, and for the normalized standard deviations the values were 26.2% and 78.5%, respectively. These uncertainty estimates for the aeroshell back face are also considered to be applicable to the centerbody payload as the environments were very similar.

Computational Method

Flow field predictions over the forebody of the THOR 70-F geometry were performed using the Langley Aerothermodynamic Upwind Relaxation Algorithm (LAURA) code (Refs. 19–20) to generate heating values for comparisons with the experimental data. LAURA is a three-dimensional, finite-volume solver that includes perfect-gas and non-equilibrium chemistry options, a variety of turbulence models, and ablation and radiative transport capabilities. In this study, the laminar, perfect-gas air model was used for the wind tunnel predictions. An axisymmetric grid geometry was used and grid adaption to the solution features was performed to align the grid outer boundary with the shock and to cluster cells near the surface to produce wall cell Reynolds numbers on the order of 1 to 10. Free stream conditions were set to the nominal wind tunnel conditions listed in Table 1 and Table 2 and the wall temperature was set to a constant 300 K. The use of a constant wall temperature is acceptable because the heat-transfer film coefficient varies only very slightly over the range of wall temperatures produced in this facility. Computed heat-transfer film coefficients were normalized by the Fay-Riddell value for the test condition to determine h/h_{FR}.

From the computational perspective, blunt body wake flow grid topology presents an additional challenge to those already discussed of unsteadiness, separation and turbulence. Aftbody and wake flows are ill-suited to solvers using structured grid topologies (e.g., LAURA) due to the difficulty in defining grids to capture the forebody bow shock and boundary layer, the free shear layer and reattached back-face boundary layer, and the concavities of the aft portion of the vehicle. For these reasons, the computational domain was limited to the front of the aeroshell and no wake-flow simulations were performed. While unstructured grid solvers represent a potential solution to the topology problem, the state-of-the-art with respect to unstructured solver validation for hypersonic heating is less advanced than for structured grid solvers.

Results and Analysis

Overview

Aeroheating data from the two tests are presented in both a qualitative format as global images and in a quantitative format as line plots. Two groups of images and plots have been provided for each view direction to illustrate both the effects of Reynolds number at a given angle of attack and the effects of angle of attack for a given unit Reynolds number on each part of the model. Aeroshell front-face heating data are shown in Figure 22 through Figure 26 in terms of h/h_{FR}. Aeroshell back-face data are shown in Figure 27 through Figure 56 and centerbody payload data are shown in Figure 57 through Figure 73, both in terms of h/h_{STAG}.

Additionally, full-page global images of the measured heating distributions from each run are shown in the appendices (in terms of h/h_{FR} for all cases). Data from the 31-Inch Mach 10 Air Tunnel Test 504 are presented in Appendix A and data from the 20-Inch Mach 6 Air Tunnel Test 7002 are presented in Appendix B. These images are of higher resolution than those in the main text to better show the details of the heating distributions. Run conditions are also given in each figure for ease of reference.

All test conditions produced laminar flow on the front face of the aeroshell as verified (see next section) by invariance of the normalized heating distributions with Reynolds number, as expected for laminar, attached flow on a blunt body. No such invariance could be expected (as discussed in the “Data Uncertainty” section) for separated wake flows and since no flow-field diagnostics were performed, the state of the wake shear layer and aeroshell back-face and payload boundary layers was not explicitly determined. However, based on AGARD WG-18 results, the separated wake shear layer and reattached back-face boundary layer were assumed to be transitional or turbulent at all test conditions.

Aeroshell Front-Face Data

Based on past experience it was expected, and confirmed in these tests, that the flow over the front face of the aeroshell would remain laminar. As shown by the global images in Figure 22 and the centerline plots of Figure 23 and Figure 24, the normalized heating distributions, h/h_{FR}, were nearly constant (less than 5% variation) across the range of both Mach 6 and Mach 10 run conditions, which is characteristic of laminar flow. The data and predictions were in close agreement as shown by the comparisons in Figure 25 and Figure 26, and peak h/h_{FR} values at the stagnation point for both experiment and computation were approximately 0.61 for all conditions. These aeroshell front-face comparisons provide baseline validation of the experimental and computational methods.

Aeroshell Back-Face Data

Distinctive effects on the heating distributions due to both angle of attack and Reynolds number were observed in the back-face data. These effects can best be seen in the plots of the least-square fits for the aeroshell back-face leeward side centerline heating vs. unit Reynolds number in Figure 53 and Figure 54 and vs. angle of attack in Figure 55 and Figure 56. The values of interest are those inward ($r/R < 0.8$) of the back-face corner (for a flight vehicle design front-face F-TPS would be carried around the shoulder to the back-face corner, while a lower capability F-TPS would be applied inward of the corner). For this region, at Mach 10, h/h_{STAG} values varied from ~0.001 at the lowest unit Reynolds number and angle-of-attack case ($\mathrm{Re}_\infty = 0.5\times10^6$/ft, $\alpha = -10$ deg) to ~0.030 at the highest unit Reynolds number and angle-of-attack case ($\mathrm{Re}_\infty = 2.0\times10^6$/ft, $\alpha = +5$ deg). At Mach 6, h/h_{STAG} values varied from ~0.02 at the lowest unit Reynolds number and angle-of-attack case ($\mathrm{Re}_\infty = 1.1\times10^6$/ft, $\alpha = 0$ deg) to ~0.055 at the highest unit Reynolds number and angle-of-attack case ($\mathrm{Re}_\infty = 3.9\times10^6$/ft, $\alpha = -5$ deg).

The normalized aeroshell back-face leeward side centerline heating distributions increased with Reynolds number for all angles-of-attack. This result is consistent with data from the previously referenced AGARD WG-18 activity and other wake flow studies, such as that for the proposed Mars Sample Return Orbiter (Ref. 21). As documented in that study, one of the reasons for this effect is the behavior of the wake flow-field structure. As the Reynolds number increases, the turning angle of the shear layer that separates from the shoulder of the vehicle becomes greater — i.e., the shear layer turns more inward toward the aft end of the vehicle. This turning of the shear layer shrinks and pressurizes the separated flow region and as a result the overall heating on the back of the vehicle increases. An additional factor contributing to the heating is that with increasing Reynolds number, transition of the wake shear layer occurs sooner, which increases the strength of turbulence in the flow.

With respect to angle-of-attack effects, data at Mach 10 showed an increase in heating with angle of attack on the leeward side centerline of the aeroshell back face. However, owing to the limited angle-of-attack range in the Mach 6 tests, the effects could not be determined for that data set. The Mach 10 results, which may seem counter-intuitive in that the heating was higher on the leeward side of the back face (as opposed to the front-face peak location on the windward side), can be explained through examination of the wake flow-field structure. In Figure 74, computed wake-flow streamlines are shown for various angles of attack for a "flight-like" THOR configuration with a more realistic payload geometry and no model support sting[2]. Flow vortices are formed in the wake of the vehicle, and at $\alpha = 0$ deg they impinge and stagnate on the end of the centerbody payload. But, as the angle of attack increases, the back-face stagnation point, where the heating is highest, moves off the centerbody end cap and onto the back-face of the aeroshell leeward side, thus producing higher heating on the back face side of the aeroshell opposite that of front-face stagnation point location.

---

[2] These results were generated as part of the THOR project, courtesy of Adam Wise at NASA LaRC

Centerbody Payload Data

As with the aeroshell back face, the payload heating environment was also very dependent on Reynolds number and angle of attack. These effects are summarized in the least-squares fit plots of heating vs. Reynolds number (Figure 70 and Figure 71) and heating vs. angle of attack (Figure 72 and Figure 73) for the leeward side centerline of the payload. Similarly to the aeroshell back-face heating, the payload heating on the leeward side centerline increased with both Reynolds number and angle of attack. At Mach 10, h/h_{STAG} values varied from ~0.001 at the lowest unit Reynolds number and angle-of-attack case ($\mathrm{Re}_\infty = 0.5\times10^6$/ft, $\alpha = -10$ deg) to ~0.036 at the highest unit Reynolds number and angle-of-attack case ($\mathrm{Re}_\infty = 2.0\times10^6$/ft, $\alpha = +5$ deg). At Mach 6, h/h_{STAG} values varied from ~0.008 at the lowest unit Reynolds number and angle-of-attack case ($\mathrm{Re}_\infty = 1.1\times10^6$/ft, $\alpha = -5$ deg) to ~0.050 at the highest unit Reynolds number and angle-of-attack case ($\mathrm{Re}_\infty = 3.9\times10^6$/ft, $\alpha = 0$ deg). An important caveat with respect to the payload data is that heating measurements could not be made on the end-cap of the payload due to the presence of the support sting. For flight at low angles of attack, the end-cap could be exposed to considerably higher heating levels than shown in this data set because of impingement of the wake vortices.

Extrapolation to Flight

Methods of extrapolating this ground test dataset to flight conditions were investigated to support development of future HIAD vehicles. The simplest method is to correlate the data by free stream Reynolds number and these results are shown for the aeroshell back face in Figure 75 for the $\alpha = 0$ deg cases, which was the nominal flight condition for THOR. The data shown are for three selected points on the aeroshell at r/R values of 0.5, 0.7, and 0.9. The $r/R = 0.5$ and 0.7 points are inside the aeroshell back-face cavity, whereas the $r/R = 0.9$ point is on the back of the aeroshell shoulder where higher heating rates occur. As would be expected, heating increases with Reynolds number, although there is a clear discontinuity between the Mach 10 and Mach 6 trends. However, correlation by free stream Reynolds number provides, at best, a qualitative result because the free stream conditions do not include information on the post-shock surface conditions. These post-shock conditions are strongly dependent on compressibility and chemical-kinetic effects that are not scalable by free stream Reynolds number alone.

A more appropriate means of correlating and extrapolating ground test heating data to flight conditions is based on the boundary-layer momentum thickness Reynolds number defined as

$$\mathrm{Re}_\theta = \frac{\rho_e U_e \theta}{\mu_e} \tag{2}$$

This parameter is determined from the CFD simulations and provides a more relevant set of conditions for use in correlating the data. Momentum thickness Reynolds number distributions extracted from the CFD solutions are shown in Figure 76. Values for correlating the data were taken at a point just ahead of the aeroshell forebody shoulder, which is the location of the maximum value, and are denoted as $\mathrm{Re}_{\theta,\mathrm{sh}}$. Correlations of the aeroshell back-face heating data (using both the $r/R = 0.5$ and 0.7 points, but excluding the $r/R = 0.9$ back-corner point) are given in Figure 77 with curve fits of a power-law form. Note that the discontinuities between Mach 6 and Mach 10 data noted in the previous free stream Reynolds number plots were considerably reduced in the momentum-thickness Reynolds number plots.

The first plot in Figure 77 includes all test conditions, while the second plot has the data from the two lowest unit Reynolds number Mach 6 test conditions excluded. This exclusion can be justified by examination of the aeroshell back-face global heating images from these two test points, in which it can be seen that these data exhibited a great deal of scatter in comparison to the data at the other test conditions owing to the lower temperatures at these conditions. While the curve fits generated for both data sets were reasonably good (correlation coefficients > 0.9), the fit was much better with these two low unit Reynolds number Mach 6 points excluded. Similar correlations are shown for the payload heating in Figure 78, with curve fits for both the entire data set and the data set exclusive of the lowest unit Reynolds number Mach 6 points.

The curve fit formulas for the aeroshell back face and payload centerbody are, respectively,

$$h/h_{STAG} = 1.8225\times10^{-5}\left(\mathrm{Re}_{\theta,sh}\right)^{1.7335} \quad \text{aeroshell back-face} \tag{3}$$

$$h/h_{STAG} = 5.6145\times10^{-6}\left(\mathrm{Re}_{\theta,sh}\right)^{1.8759} \quad \text{payload} \tag{4}$$

It is recommended that these curve fits be used to extrapolate the wind tunnel data to flight conditions using $\mathrm{Re}_{\theta,\mathrm{sh}}$ values generated by CFD simulations for the flight conditions. To aid in uncertainty estimation for flight conditions, these fits are reproduced in Figure 79 and Figure 80 with multipliers of $[1 + (1\times\sigma)/(h/h_{\mathrm{STAG}})]$ and $[1 + (3\times\sigma)/(h/h_{\mathrm{STAG}})]$ applied to the predicted heating fits, (which represent mutiples of 126.2% and 178.5%, respectively, as per the overall averages in Table 4). It should be noted that the estimated peak-heating flight condition for THOR would have produced an $\mathrm{Re}_{\theta,\mathrm{sh}}$ value less than the lowest value from the ground test conditions, although values further along the trajectory would fall within the test range.

Summary and Conclusions

A wind tunnel test program has been conducted to define heating environments on the back face of a blunt body aeroshell in support of the future HIAD development. Testing was conducted at unit Reynolds numbers from $\mathrm{Re}_\infty = 1.1\times10^6$/ft to 3.9×10^6/ft at Mach 6 and $\mathrm{Re}_\infty = 0.5\times10^6$/ft to 1.0×10^6/ft at Mach 10 on a 6.3088 in diameter model. Global aeroheating data were obtained on the front and back faces of the aeroshell and on the centerbody payload using phosphor thermography.

Comparisons of laminar predictions with aeroshell front-face data confirmed laminar flow on the forebody at all conditions, while back-face data were likely transitional or turbulent. Leeward side back-face and payload heating levels were dependent on free stream Reynolds number and angle of attack. In general, heating in both regions increased with Reynolds number and with angle of attack. The highest aeroshell back-face heating levels were measured on the leeward side ($+z$ direction), which is opposite of the peak heating location on the windward side ($-z$ direction) of the front face. The reason for this behavior was impingement of the wake shear layer on the leeward side of the back face. The highest measured levels, relative to the aeroshell front-face stagnation point, were h/h_{STAG} ~0.05 on the aeroshell back face and h/h_{STAG} ~0.06 on the payload.

Back-face and payload heating levels were correlated (for $\alpha = 0$ deg) as a function of the maximum momentum thickness Reynolds number $Re_{\theta,sh}$ ahead of aeroshell front-face shoulder. Heating uncertainty estimates based on normalized $1\times\sigma$ and $3\times\sigma$ levels were determined to be ±26% and ±78%, respectively. Based on the $Re_{\theta,sh}$ correlations, the relative h/h_{STAG} heating levels measured in this study were expected to be higher than those at the peak heating point on the THOR flight trajectory.

References

1. Rohrschneider, R. R. and Braun, R. D., "Survey of Ballute Technology for Aerocapture," *Journal of Spacecraft and Rockets*, Vol. 44, No. 1, January–February 2007, pp.10–23.
2. Hughes, S. J., Cheatwood, F. M., Dillman, R. A., Wright, H. S., DelCorso, J. A. and Calomino, A. M., "Hypersonic Inflatable Aerodynamic Decelerator (HIAD) Technology Development Overview," AIAA Paper 2011-2525, 21st AIAA Aerodynamic Decelerator Systems Technology Conference and Seminar, Dublin, Ireland, May 23–26, 2011.
3. Hughes, S. J, Dillman, R. A., Starr, B. R., Stephan, R. A., Lindell, M. C., Player, C. J. and Cheatwood, F. M., "Inflatable Re-entry Vehicle Experiment (IRVE) Design Overview," AIAA Paper 2005-1636, 18th Aerodynamic Decelerator Systems Technology Conference and Seminar, Munich, Germany, May 25 2005.
4. O'Keefe, S. A. and Bose, D. M., "IRVE-II Post-Flight Trajectory Reconstruction," AIAA Paper 2010-7515, AIAA Atmospheric Flight Mechanics Conference, Toronto, Ontario Canada, August 2–5, 2010.
5. Olds, A. D., Beck, R. E., Bose, D. M., White, J. P., Edquist, K. T., Hollis, B. R., Lindell, M. C., Cheatwood, F. C., Gsell, V. T. and Bowden, E. L., "IRVE-3 Post-Flight Reconstruction," AIAA Paper 2013-1390, AIAA Aerodynamic Decelerator Systems Conference, Daytona Beach, FL, March 25–28, 2013.
6. Dillman, R., Hughes, S., DiNonno, J., Bodkin, R., White, J., DelCorso, J. and Cheatwood, F. M., "Planned Flight of the Terrestrial HIAD Orbital Reentry," 11th International Planetary Probe Workshop, Pasadena, CA, June 16–20, 2014.
7. Muylaert, J., Kumar, A. and Dujarric, C. (editors), *Hypersonic Experimental and Computational Capability, Improvement and Validation*", Chapters 3–4, AGARD Advisory Report 319, Vol. II, December 1998.
8. Horvath, T. J., McGinley, C. B. and Hannemann, K-Body Near-Wake Flow Field at Mach 6," AIAA Paper 1996-1935, AIAA 27th Fluid Dynamics Conference, New Orleans, LA, June 17–20, 1996.
9. Horvath, T. and Hannemann, K., "Blunt-Body Near-Wake Flow Field at Mach 10," AIAA 35th Aerospace Sciences Meeting and Exhibit, Reno NV, January 6–9, 1997.
10. Holden, M., Harvey, J., Body, I., George, I. and Horvath, T., "Experimental and Computational Studies of the Flow Over a Sting Mounted Planetary Probe Configuration," AIAA Paper 1997-0768, 35th Aerospace Sciences Meeting and Exhibit, Reno NV, January 6–9, 1997.
11. Hollis, B. R. and Perkins, J. N., "Transition Effects on Heating in the Wake of a Blunt Body," *Journal of Spacecraft and Rockets*, Vol. 36, No. 5, September-October 1999, pp. 668–674.

12. Edquist, K. T., Dyakonov, A. A., Wright, M. J., and Tang, C. Y., "Aerothermodynamic Design of the Mars Science Laboratory Backshell and Parachute Cone," AIAA Paper 2009-4078, 41st AIAA Thermophysics Conference, San Antonio, TX, June 22–25, 2009.
13. Buck, G. M., "Rapid Model Fabrication and Testing for Aerospace Vehicles," AIAA Paper 2000-0826, 38th AIAA Aerospace Sciences Meeting and Exhibit, Reno, NV, January 10–13, 2000.
14. Hollis, B. R., Berger, K. T., Berry, S. A., Brauckmann, G. J., et al, "Entry, Descent, and Landing Aerothermodynamics: NASA Langley Experimental Capabilities and Contributions," AIAA Paper 2014-1154, AIAA 52nd Aerospace Science Meeting, National Harbor, MD, January 13–17, 2014.
15. Berger, K., Rufer, S., Hollingsworth, K. and Wright, S., "NASA Langley Aerothermodynamic Laboratory: Hypersonic Testing Capabilities," AIAA Paper 2015-1337, 53rd AIAA Aerospace Sciences Meeting, Kissimmee, FL, January 5–9, 2015.
16. Fay, J. A., and Riddell, F. R., "Theory of Stagnation Point Heat Transfer in Dissociated Air," *Journal of Aeronautical Sciences*, Vol. 25, No. 2., February 1958, pp. 73–85.
17. Buck, G. M., "Surface Temperature/Heat Transfer Measurement Using a Quantitative Phosphor Thermography System," AIAA Paper 91-0064, 29th Aerospace Sciences Meeting, Reno, NV, January 7–10, 1991.
18. Merski, N. R., "Global Aeroheating Wind-Tunnel Measurements Using Improved Two-Color Phosphor Thermography Methods," *Journal of Spacecraft and Rockets*, Vol. 36, No. 2, March-April 1999, pp. 160–170.
19. Gnoffo, P. A., "An Upwind-Biased, Point-Implicit Algorithm for Viscous, Compressible Perfect-Gas Flows," NASA TP-2953, February 1990.
20. Mazaheri, A., Gnoffo, P. A., Johnston, C. O., and Kleb, B., "LAURA User's Manual: 5.5-65135," NASA TM-2013-217800, February 2011.
21. Horvath, T. J., Heiner, N. C., Olguin, D. M., Cheatwood, F. M. and Gnoffo, P. A., "Aftbody Heating Characteristics of a Proposed Mars Sample Return Orbiter," AIAA Paper 2001-3608, AIAA 35th Thermophysics Conference, Anaheim, CA, June 11–14, 2001.

Table 1. Test 504, 31-Inch Mach 10 Air Tunnel conditions.

Run	**α** (deg)	Re_∞ **(1/ft)**	M_∞	T_∞ **(K)**	ρ_∞ **(kg/m^3)**	U_∞ **(m/s)**	ΔH_{tot} **(J/kg)**	h_{FR} **(kg/m$^2 \cdot$ s)**	**View**
34	–10	5.008E+05	9.87	50.2	4.203E-03	1402	7.322E+05	2.059E-01	Back
31	–10	1.049E+06	9.81	51.0	8.926E-03	1403	7.349E+05	3.004E-01	Back
33	–10	1.049E+06	9.81	51.0	8.926E-03	1403	7.349E+05	3.004E-01	Back
32	–10	2.038E+06	9.96	49.8	1.691E-02	1405	7.360E+05	4.140E-01	Back
24	–5	5.008E+05	9.87	50.2	4.203E-03	1402	7.322E+05	2.059E-01	Back
23	–5	1.049E+06	9.81	51.0	8.926E-03	1403	7.349E+05	3.004E-01	Back
25	–5	2.038E+06	9.96	49.8	1.691E-02	1405	7.360E+05	4.140E-01	Back
10	0	5.008E+05	9.87	50.2	4.203E-03	1402	7.322E+05	2.059E-01	Back
9	0	1.049E+06	9.81	51.0	8.926E-03	1403	7.349E+05	3.004E-01	Back
11	0	2.038E+06	9.96	49.8	1.691E-02	1405	7.360E+05	4.140E-01	Back
28	5	5.008E+05	9.87	50.2	4.203E-03	1402	7.322E+05	2.059E-01	Back
26	5	1.049E+06	9.81	51.0	8.926E-03	1403	7.349E+05	3.004E-01	Back
27	5	1.049E+06	9.81	51.0	8.926E-03	1403	7.349E+05	3.004E-01	Back
29	5	2.038E+06	9.96	49.8	1.691E-02	1405	7.360E+05	4.140E-01	Back
30	5	2.038E+06	9.96	49.8	1.691E-02	1405	7.360E+05	4.140E-01	Back
6	0	5.008E+05	9.87	50.2	4.203E-03	1402	7.322E+05	2.059E-01	Front
5	0	1.049E+06	9.81	51.0	8.926E-03	1403	7.349E+05	3.004E-01	Front
8	0	2.038E+06	9.96	49.8	1.691E-02	1405	7.360E+05	4.140E-01	Front

Table 2. Test 7002, 20-Inch Mach 10 Air Tunnel conditions.

Run	**α** (deg)	**Re_∞** **(1/ft)**	**M_∞**	**T_∞** **(K)**	**ρ_∞** **(kg/m^3)**	**U_∞** **(m/s)**	**ΔH_{tot}** **(J/kg)**	**h_{FR}** **(kg/m$^2 \cdot$ s)**	**View**
16	–5	1.074E+06	5.90	61.5	1.677E-02	927	1.904E+05	2.510E-01	Back
19	–5	2.066E+06	5.97	62.5	3.218E-02	945	2.083E+05	3.560E-01	Back
18	–5	3.049E+06	5.99	62.7	4.736E-02	950	2.133E+05	4.346E-01	Back
17	–5	3.915E+06	6.01	63.2	6.096E-02	956	2.199E+05	4.972E-01	Back
13	0	1.074E+06	5.90	61.5	1.677E-02	927	1.904E+05	2.510E-01	Back
14	0	2.066E+06	5.97	62.5	3.218E-02	945	2.083E+05	3.560E-01	Back
15	0	3.049E+06	5.99	62.7	4.736E-02	950	2.133E+05	4.346E-01	Back
12	0	3.915E+06	6.01	63.2	6.096E-02	956	2.199E+05	4.972E-01	Back
7	0	1.074E+06	5.90	61.5	1.677E-02	927	1.904E+05	2.510E-01	Front
11	0	1.074E+06	5.90	61.5	1.677E-02	927	1.904E+05	2.510E-01	Front
8	0	2.066E+06	5.97	62.5	3.218E-02	945	2.083E+05	3.560E-01	Front
9	0	3.049E+06	5.99	62.7	4.736E-02	950	2.133E+05	4.346E-01	Front
10	0	3.915E+06	6.01	63.2	6.096E-02	956	2.199E+05	4.972E-01	Front

Table 3. Average aeroshell back-face temperature rise.

	Condition		
Test	**Re_∞ (1/ft)**	**M_∞**	**ΔT_∞ (K)**
504	5.008E+05	9.87	1
504	1.049E+06	9.81	3
504	2.038E+06	9.96	6
7002	1.074E+06	5.90	1
7002	2.066E+06	5.97	3
7002	3.049E+06	5.99	4
7002	3.915E+06	6.01	6

Table 4. Aeroshell back-face heating data uncertainty estimates.

	Condition					
Test	**Re_∞ (1/ft)**	**M_∞**	**1×σ**	**3×σ**	**1×σ/(h/h$_{stag,av}$)**	**3×σ/(h/h$_{stag,av}$)**
504	5.008E+05	9.87	0.0041	0.0123	51.3%	153.8%
504	1.049E+06	9.81	0.0042	0.0126	27.8%	83.4%
504	2.038E+06	9.96	0.0042	0.0126	20.0%	60.0%
7002	1.074E+06	5.90	0.0079	0.0237	31.3%	94.0%
7002	2.066E+06	5.97	0.0063	0.0189	17.7%	53.2%
7002	3.049E+06	5.99	0.0064	0.0192	17.2%	51.6%
7002	3.915E+06	6.01	0.0085	0.0255	17.9%	53.7%
Test 504 averages			0.0042	0.0125	33.0%	99.1%
Test 7002 averages			0.0073	0.0218	21.0%	63.1%
Overall averages			0.0059	0.0178	26.2%	78.5%

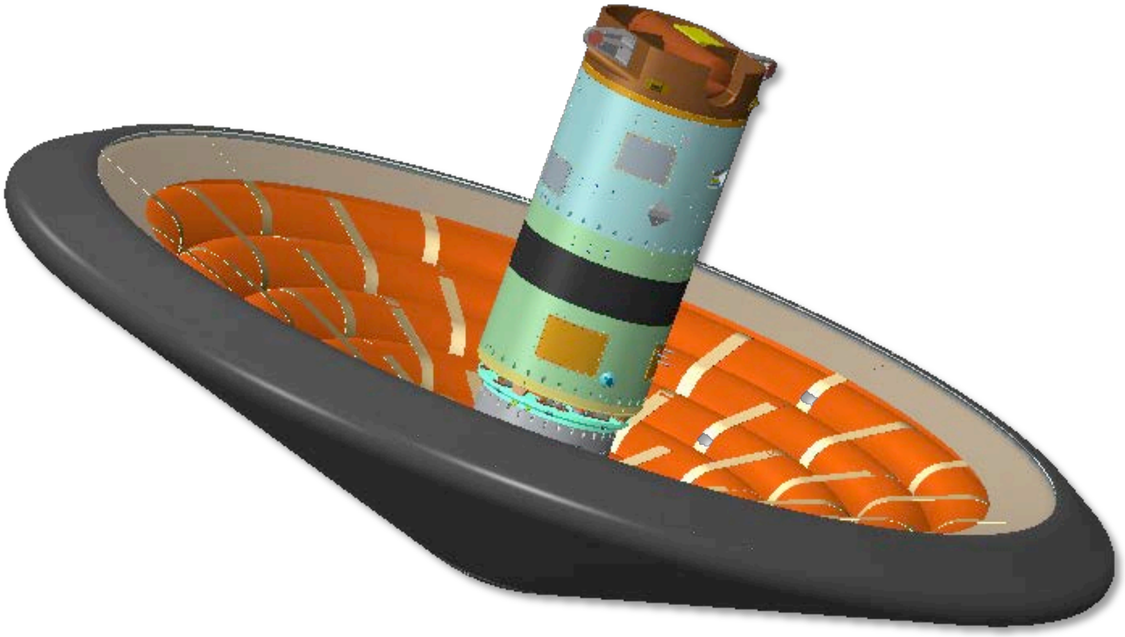

Figure 1. Artist's concept of THOR reentry vehicle.

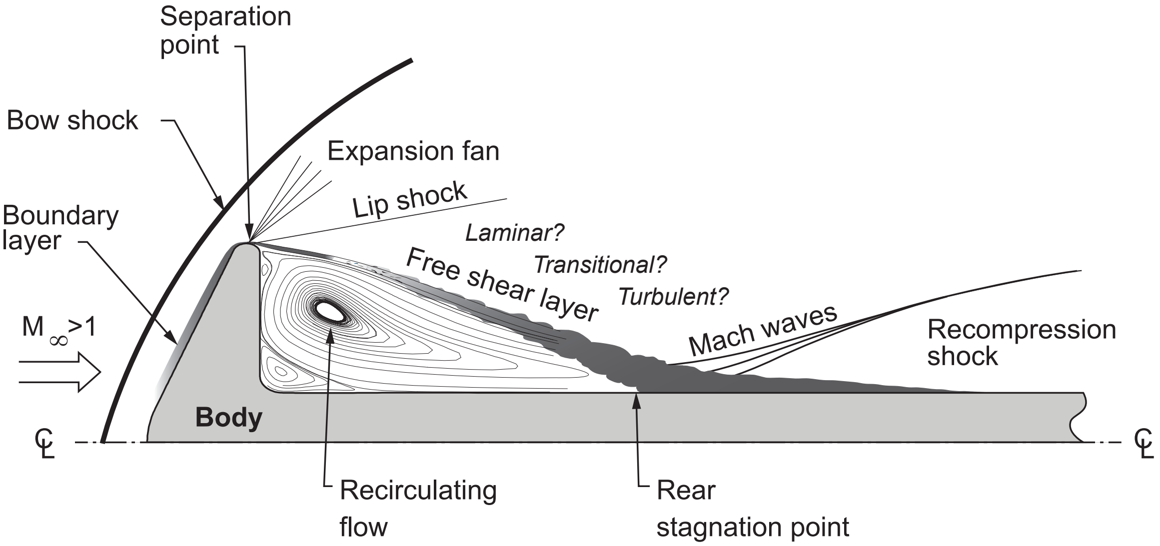

Figure 2. Blunt body wake flow features. (redrawn from Ref. 8)

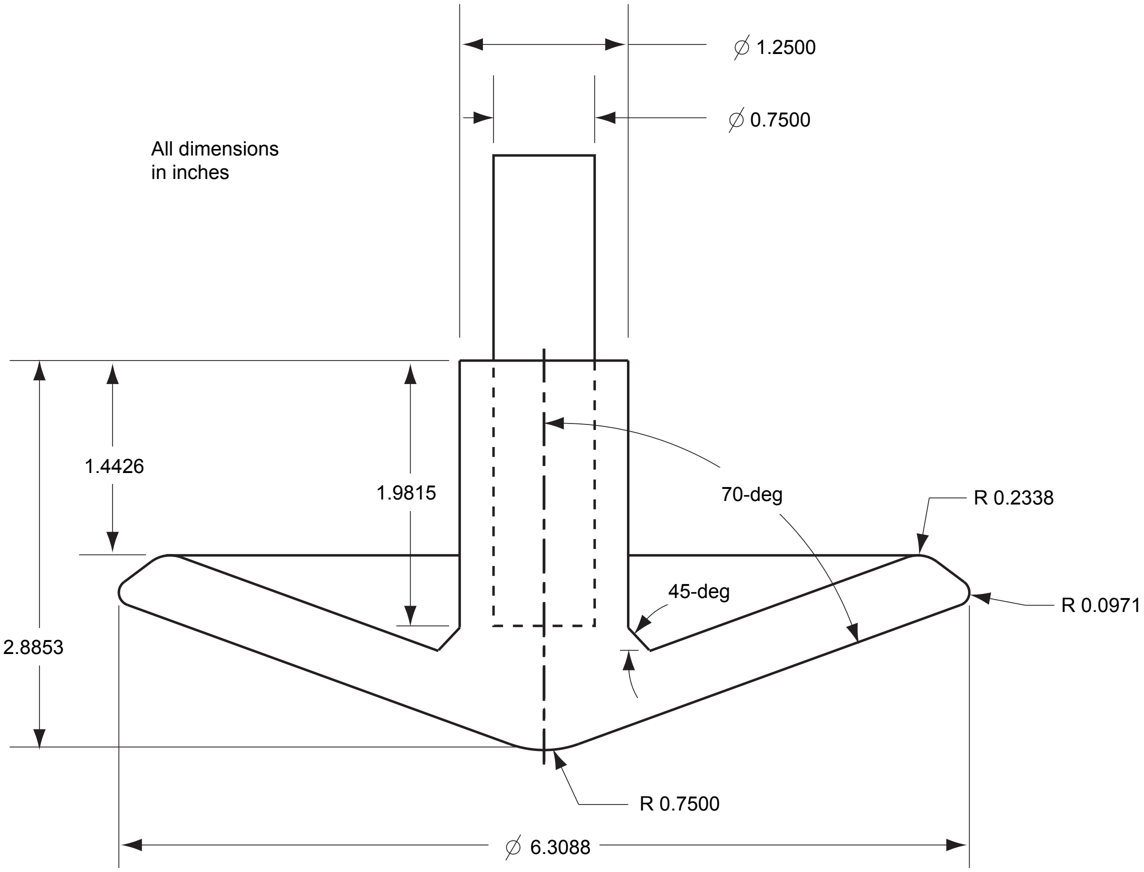

Figure 3.THOR 70-F wind tunnel model geometry.

Figure 4. LaRC 31-Inch Mach 10 Air Tunnel.

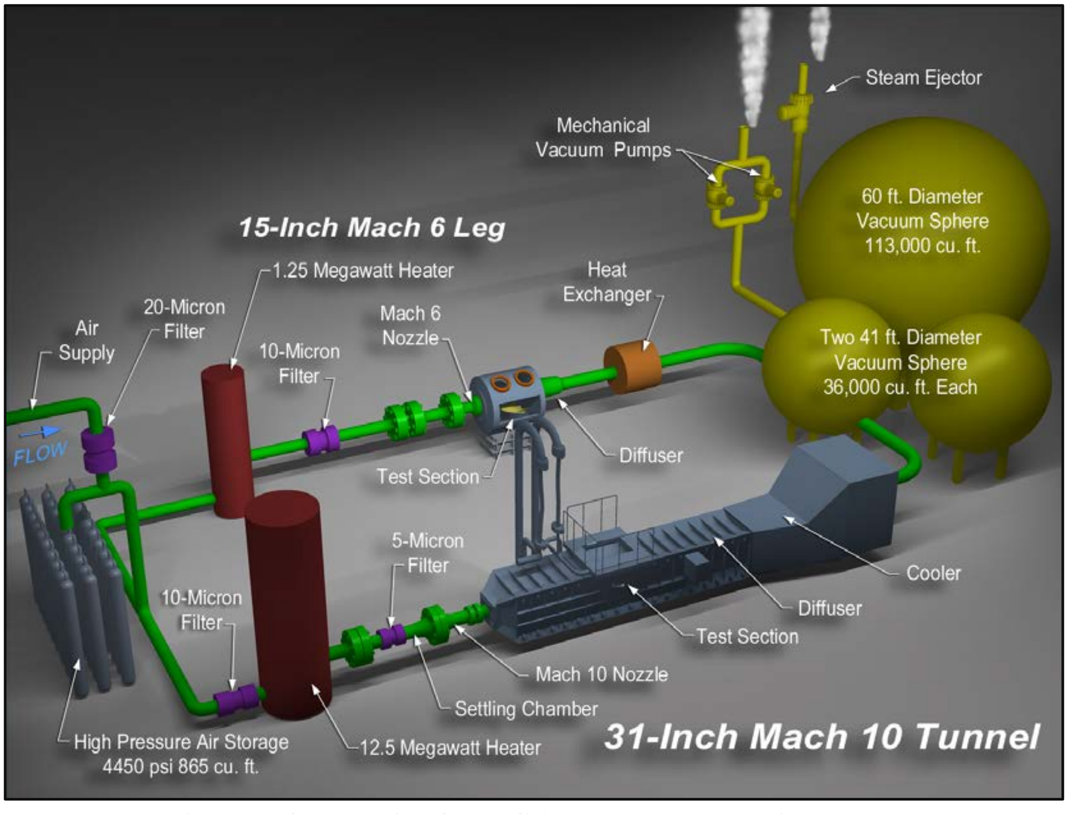

Figure 5. Schematic of LaRC 31-Inch Mach 10 Air Tunnel.

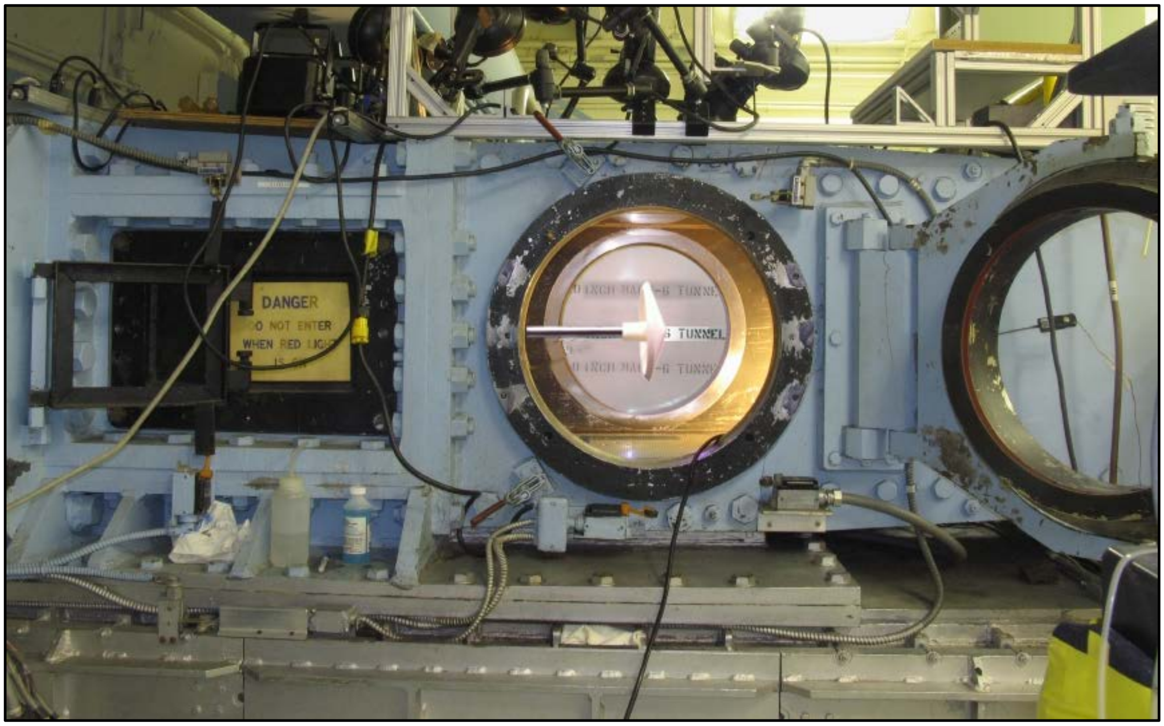

Figure 6. LaRC 20-Inch Mach 6 Air Tunnel.

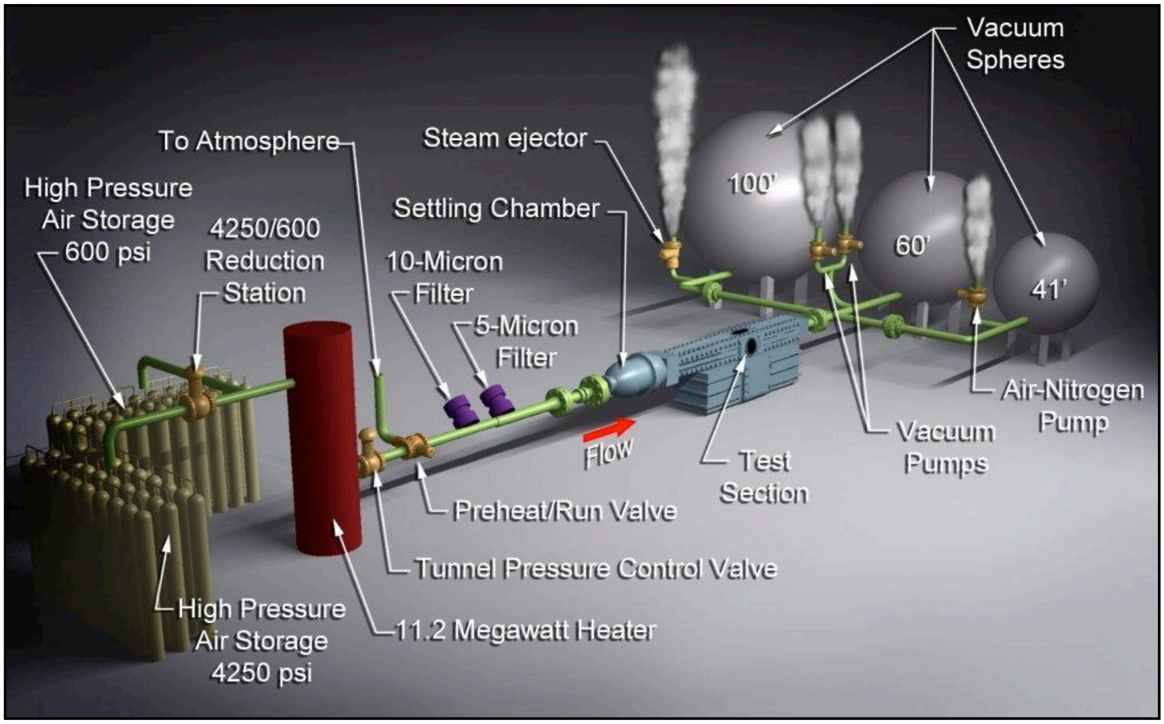

Figure 7. Schematic of LaRC 20-Inch Mach 6 Air Tunnel.

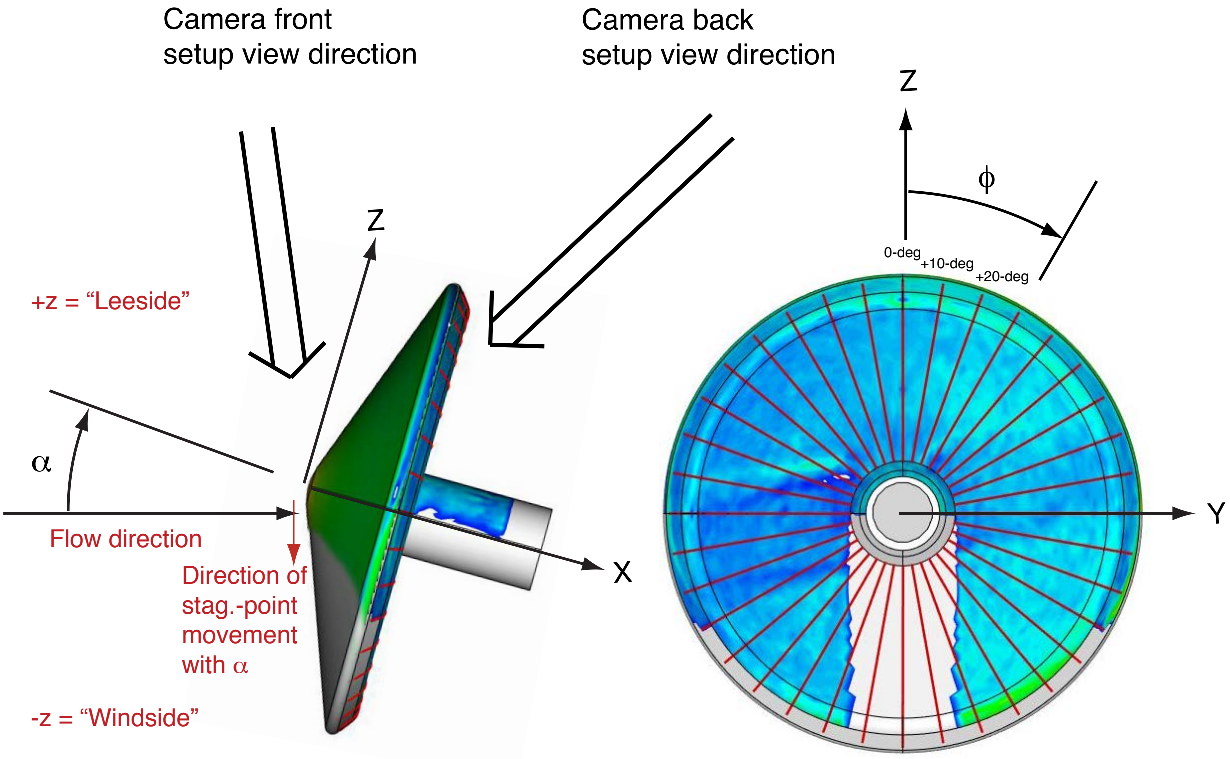

Side View

Rear View

Figure 8. Camera view directions and coordinate system nomenclature.

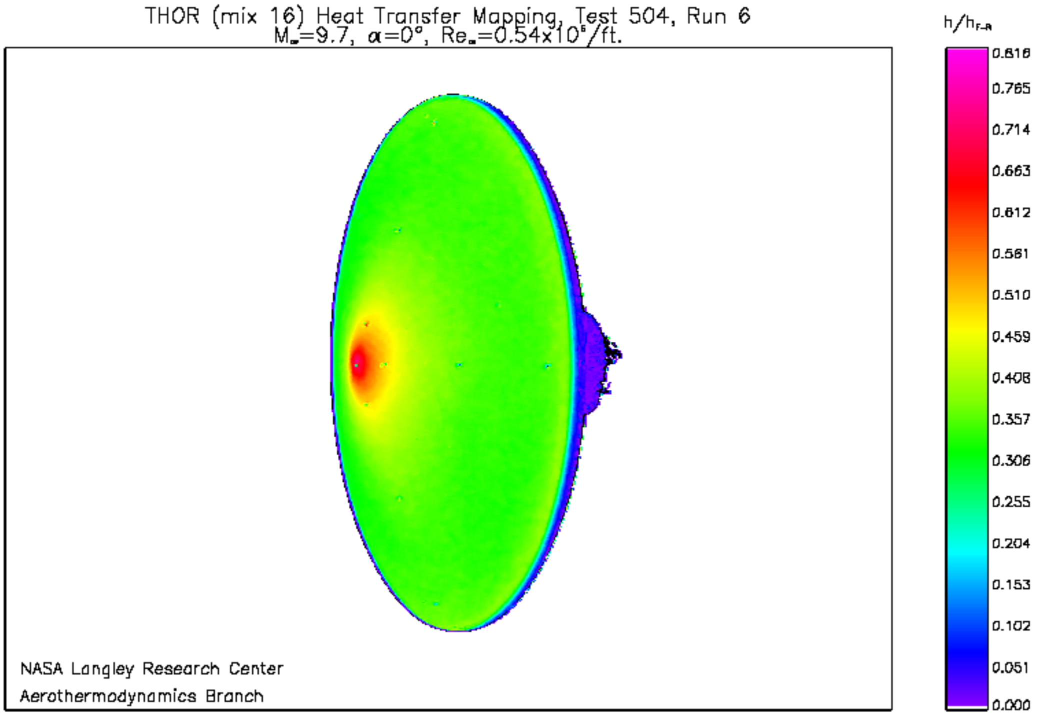

Figure 9. Sample two-dimensional image data from IHEAT.

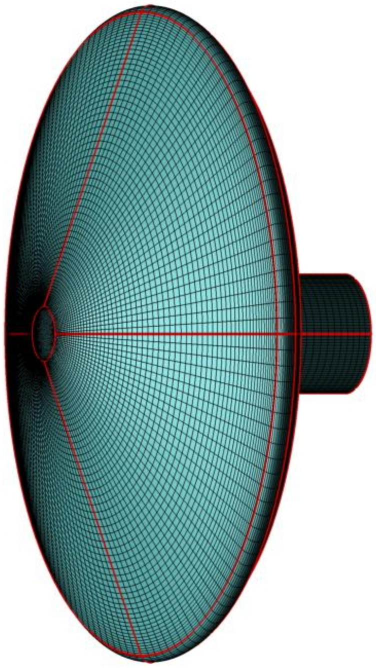

Figure 10. Sample three-dimensional vehicle surface geometry.

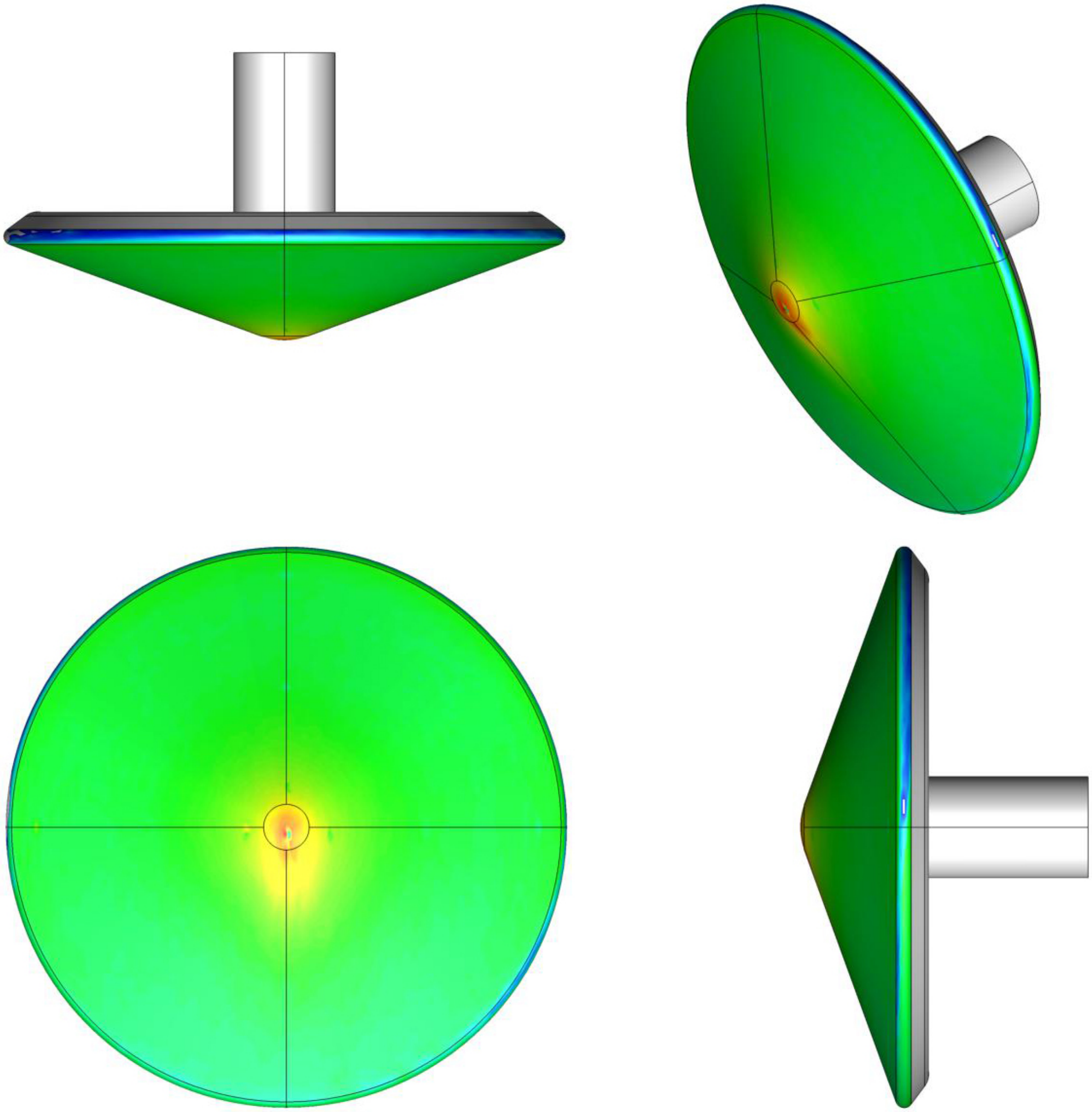

Figure 11. Sample mapping of image data onto vehicle surface geometry.

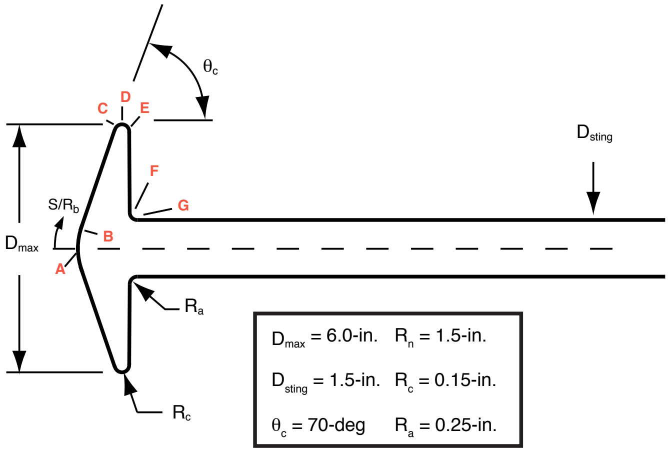

Figure 12. AGARD-18 model geometry.

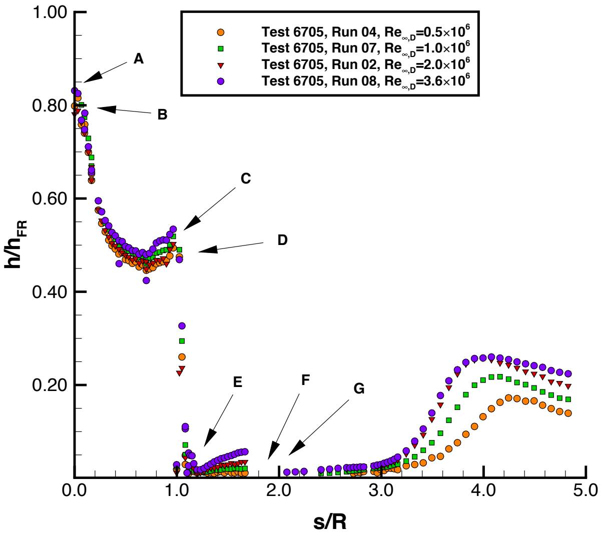

Figure 13. AGARD-18 heating distribution vs. unit Reynolds number on model and sting.

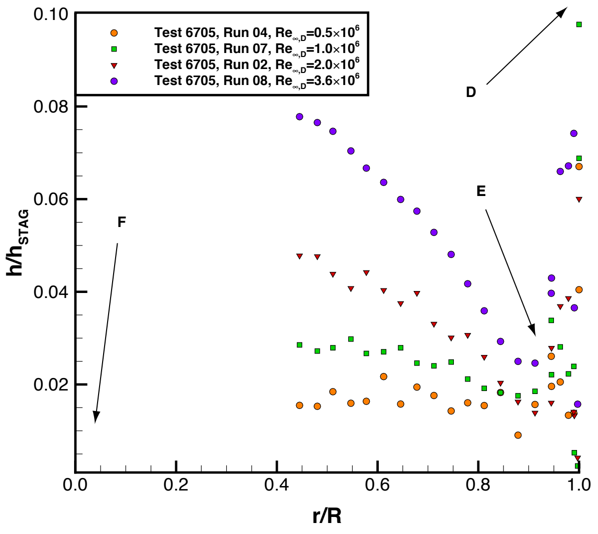

Figure 14. AGARD-18 heating distribution vs. unit Reynolds number, back-face close-up.

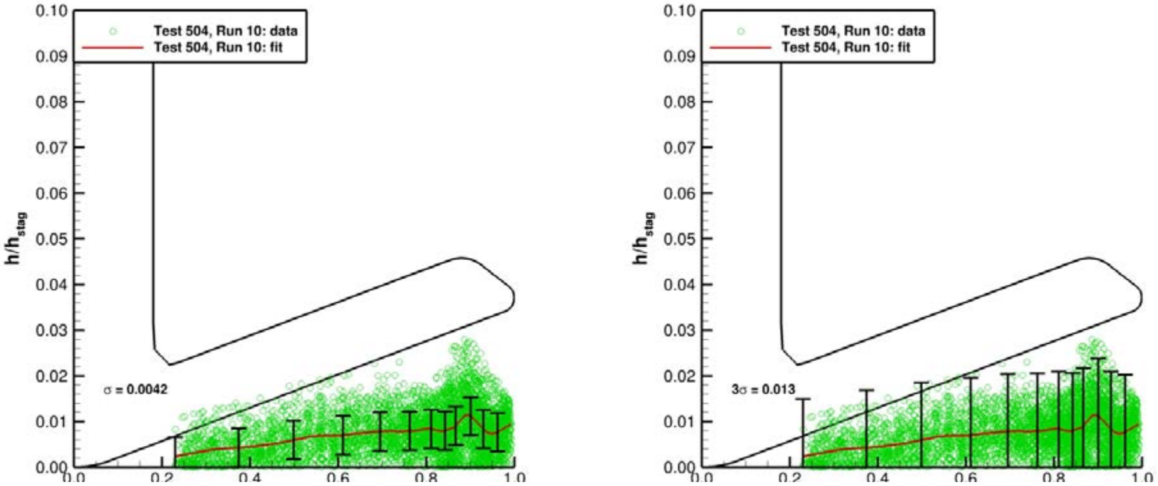

1×σ uncertainty 3×σ uncertainty

Figure 15. Back-face uncertainty estimates for $M_\infty = 10$, $Re_\infty = 0.5\times10^6$/ft condition.

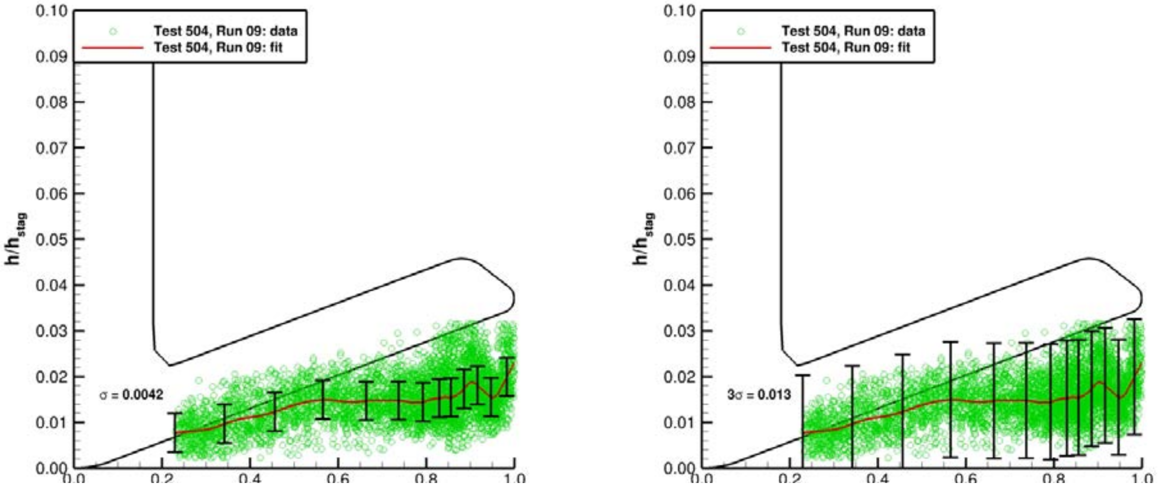

1×σ uncertainty 3×σ uncertainty

Figure 16. Back-face uncertainty estimates for $M_\infty = 10$, $Re_\infty = 1.0\times10^6$/ft condition.

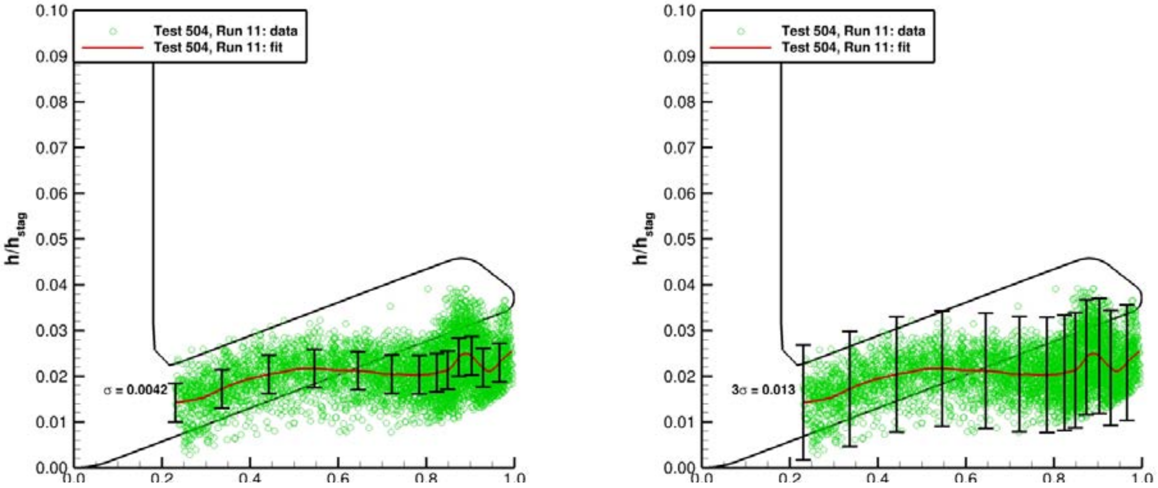

1×σ uncertainty 3×σ uncertainty

Figure 17. Back-face uncertainty estimates for $M_\infty = 10$, $Re_\infty = 2.0\times10^6$/ft condition.

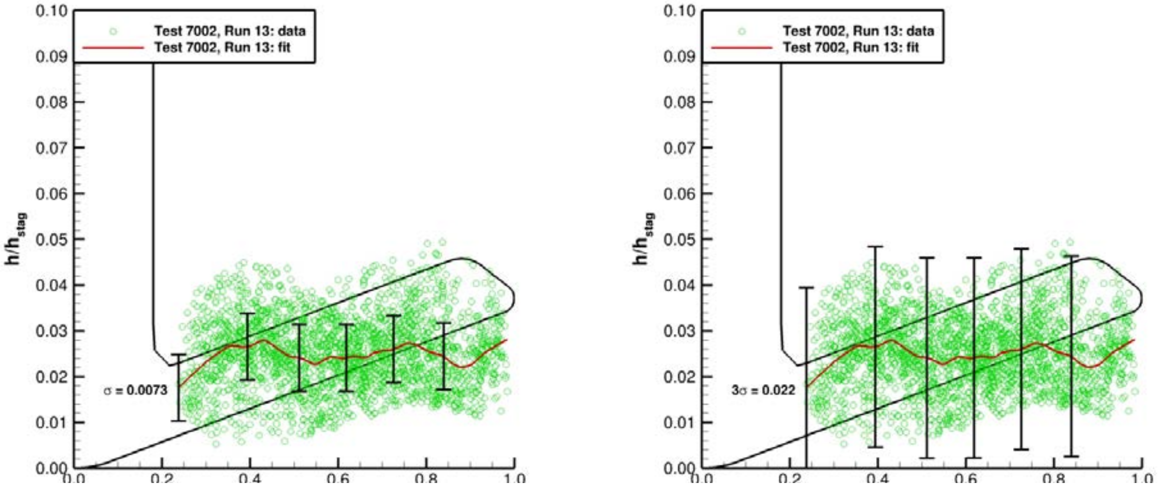

1×σ uncertainty 3×σ uncertainty

Figure 18. Back-face uncertainty estimates for $M_\infty = 6$, $Re_\infty = 1.1\times10^6$/ft condition.

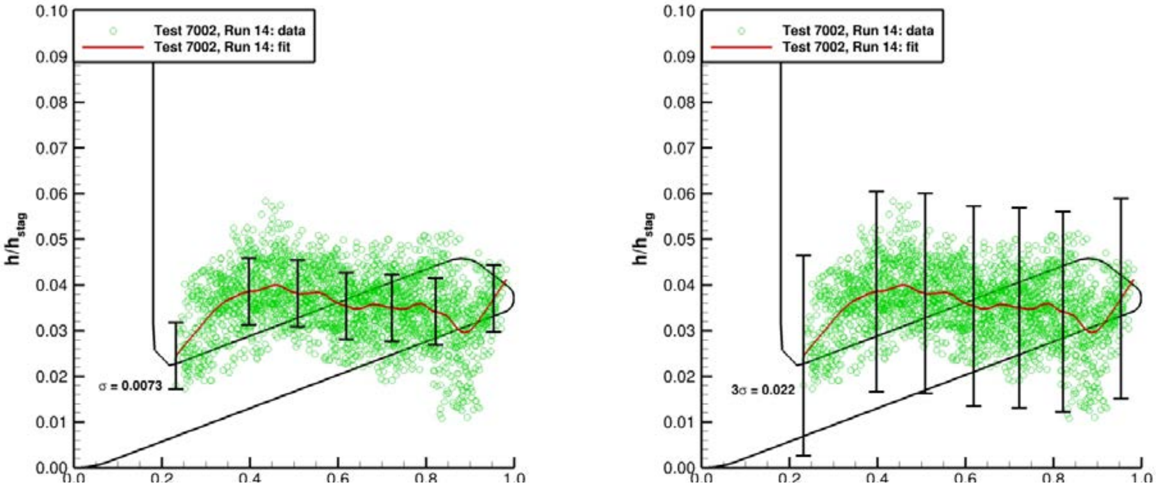

1×σ uncertainty 3×σ uncertainty

Figure 19. Back-face uncertainty estimates for $M_\infty = 6$, $Re_\infty = 2.1\times10^6$/ft condition.

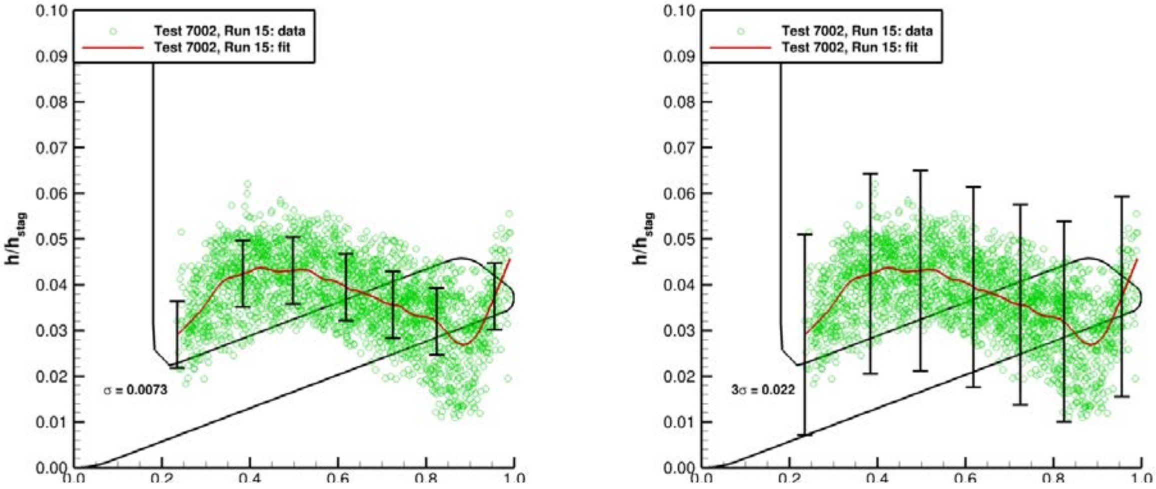

1×σ uncertainty 3×σ uncertainty

Figure 20. Back-face uncertainty estimates for $M_\infty = 6$, $Re_\infty = 3.1\times10^6$/ft condition.

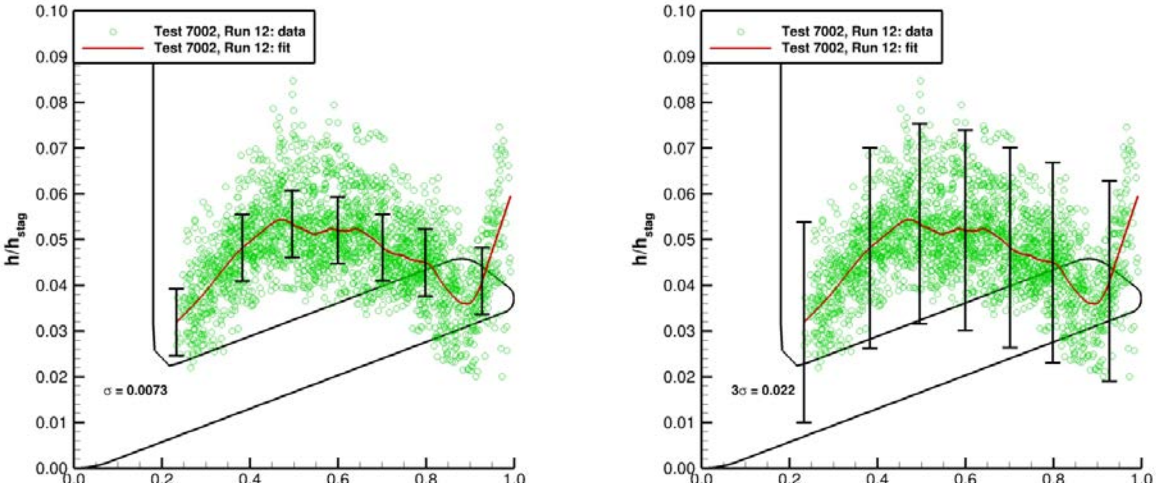

1×σ uncertainty 3×σ uncertainty

Figure 21. Back-face uncertainty estimates for $M_\infty = 6$, $Re_\infty = 3.9\times10^6$/ft condition.

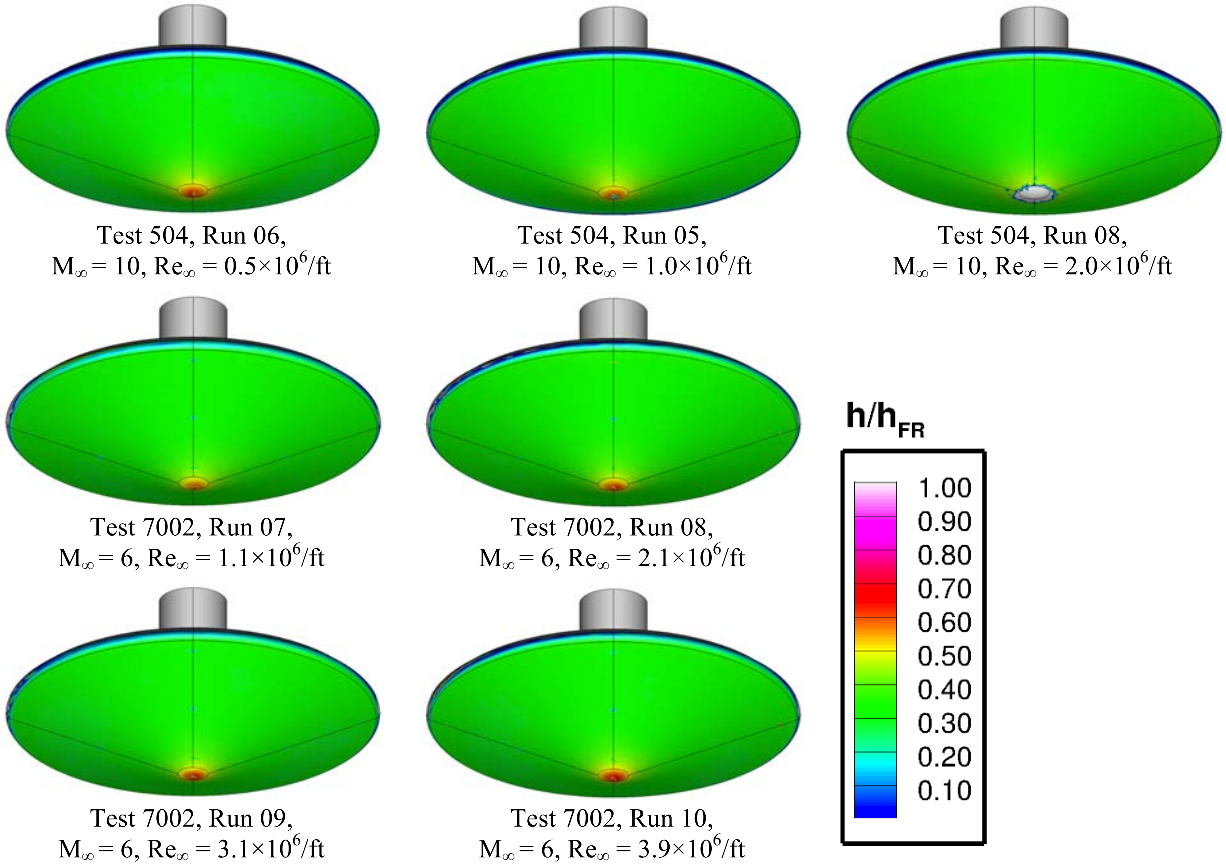

Test 504, Run 06,
$M_\infty = 10$, $Re_\infty = 0.5\times10^6$/ft

Test 504, Run 05,
$M_\infty = 10$, $Re_\infty = 1.0\times10^6$/ft

Test 504, Run 08,
$M_\infty = 10$, $Re_\infty = 2.0\times10^6$/ft

Test 7002, Run 07,
$M_\infty = 6$, $Re_\infty = 1.1\times10^6$/ft

Test 7002, Run 08,
$M_\infty = 6$, $Re_\infty = 2.1\times10^6$/ft

Test 7002, Run 09,
$M_\infty = 6$, $Re_\infty = 3.1\times10^6$/ft

Test 7002, Run 10,
$M_\infty = 6$, $Re_\infty = 3.9\times10^6$/ft

Figure 22. Aeroshell front-face heating images: Reynolds number effects, α = 0 deg.

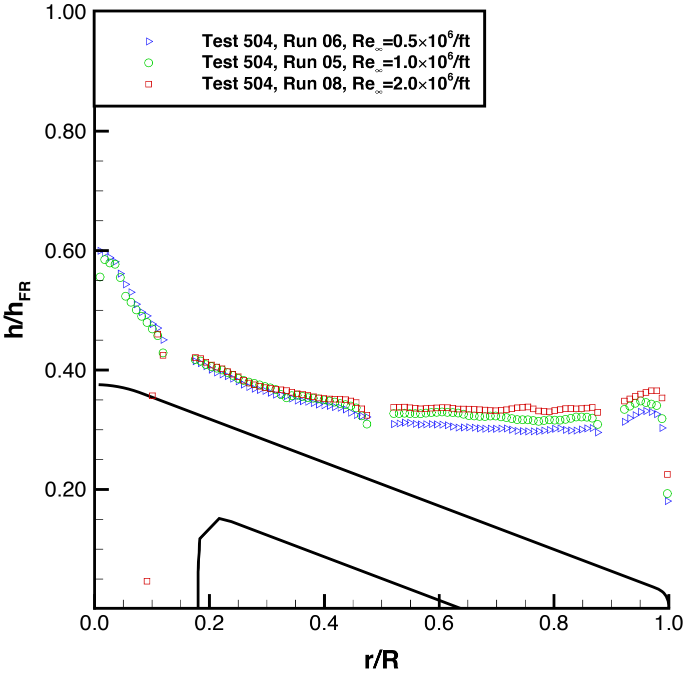

Figure 23. Front-face centerline heating, Reynolds number effects, $M_\infty = 10$, $\alpha = 0$ deg.

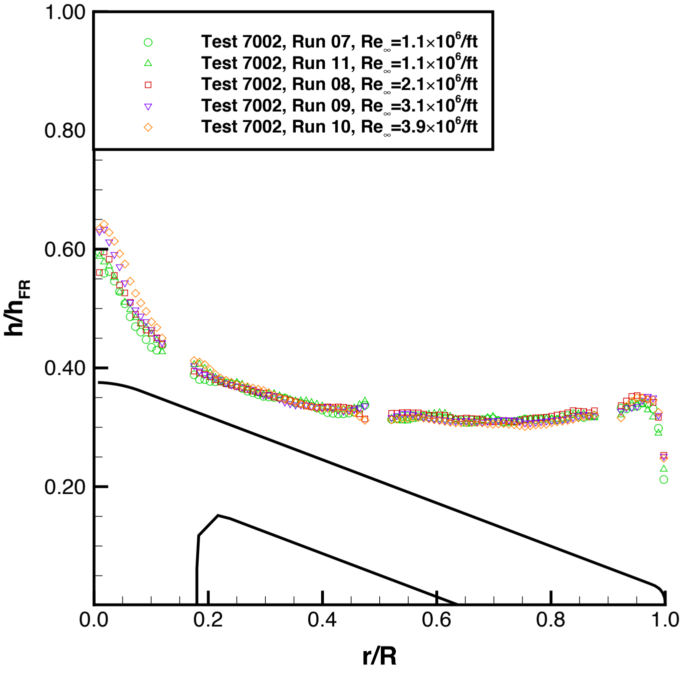

Figure 24. Front-face centerline heating: Reynolds number effects, $M_\infty = 6$, $\alpha = 0$ deg.

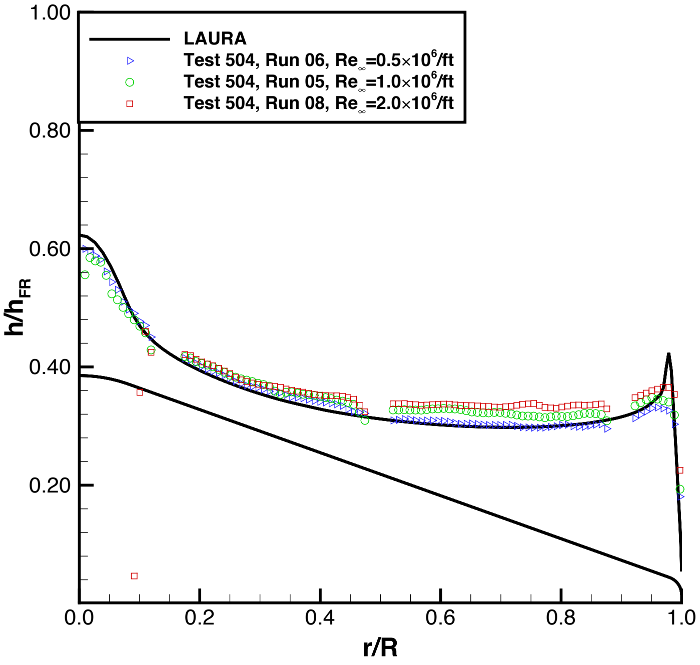

Figure 25. Front-face centerline heating: Reynolds number effects, $M_\infty = 10$, $\alpha = 0$ deg.

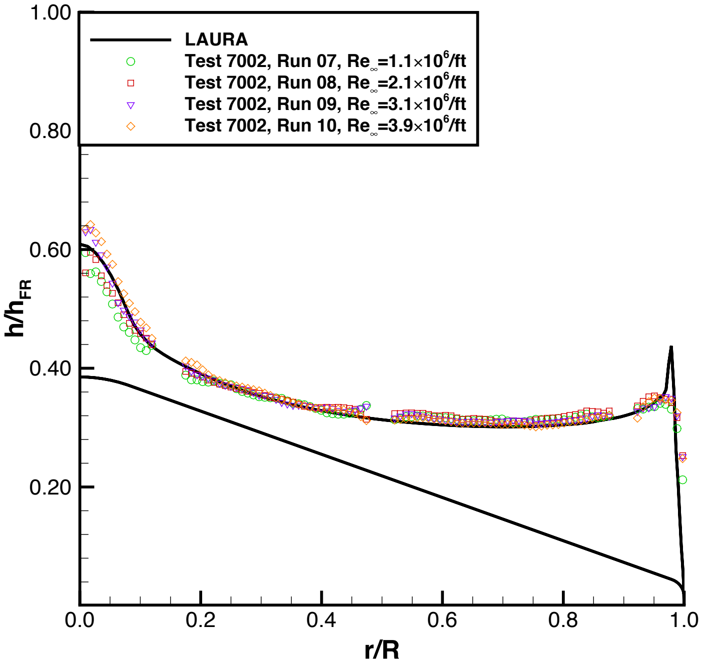

Figure 26. Front-face centerline heating: Reynolds number effects, $M_\infty = 6$, $\alpha = 0$ deg.

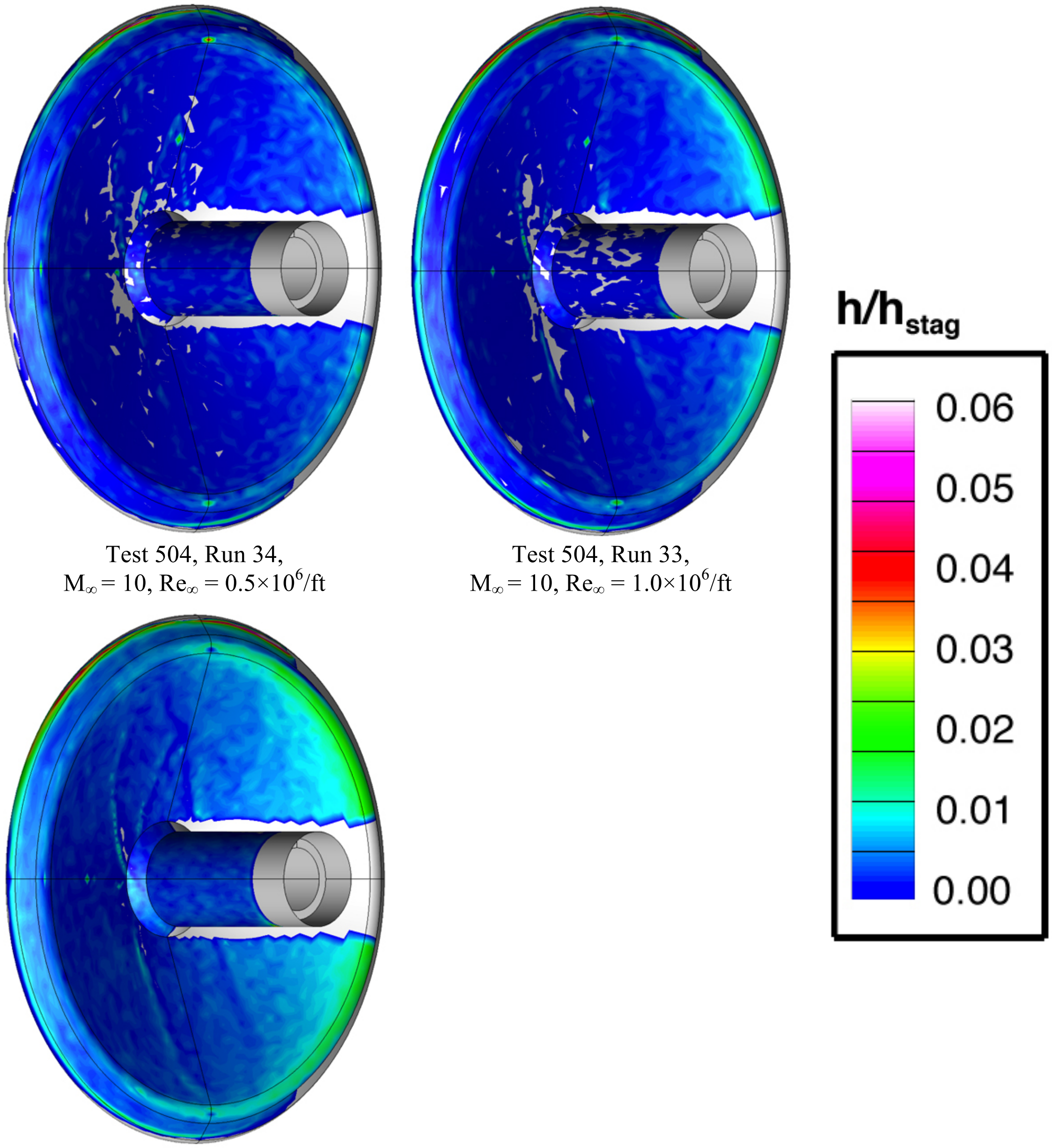

Test 504, Run 34,
$M_\infty = 10$, $Re_\infty = 0.5\times10^6$/ft

Test 504, Run 33,
$M_\infty = 10$, $Re_\infty = 1.0\times10^6$/ft

Test 504, Run 32,
$M_\infty = 10$, $Re_\infty = 2.0\times10^6$/ft

Figure 27. Back-face heating images: Reynolds number effects, $M_\infty = 10$, $\alpha = -10$ deg.

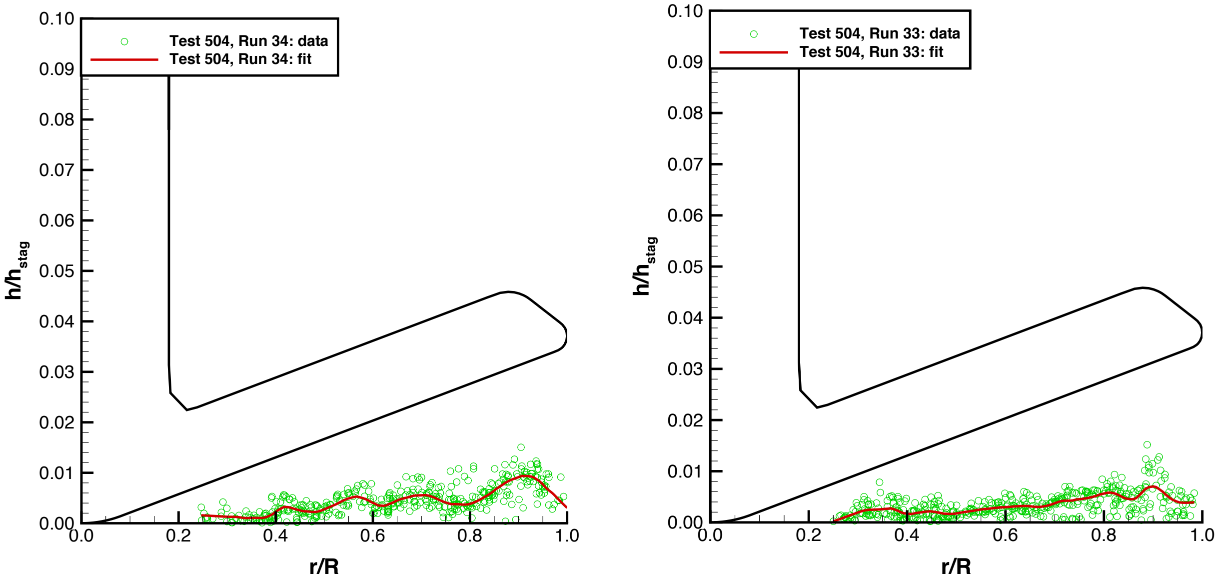

Test 504, Run 34,
$M_\infty = 10$, $Re_\infty = 0.5\times10^6$/ft

Test 504, Run 33,
$M_\infty = 10$, $Re_\infty = 1.0\times10^6$/ft

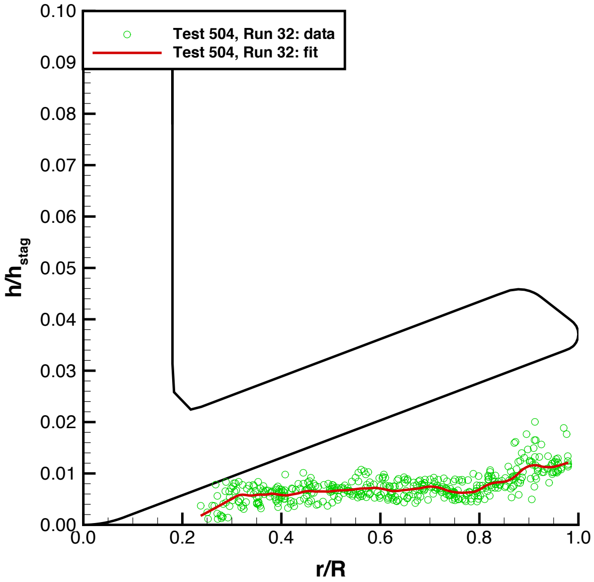

Test 504, Run 32,
$M_\infty = 10$, $Re_\infty = 2.0\times10^6$/ft

Data from $\phi = -20$ deg to +20 deg rays

Figure 28. Back-face heating data: Reynolds number effects, $M_\infty = 10$, $\alpha = -10$ deg.

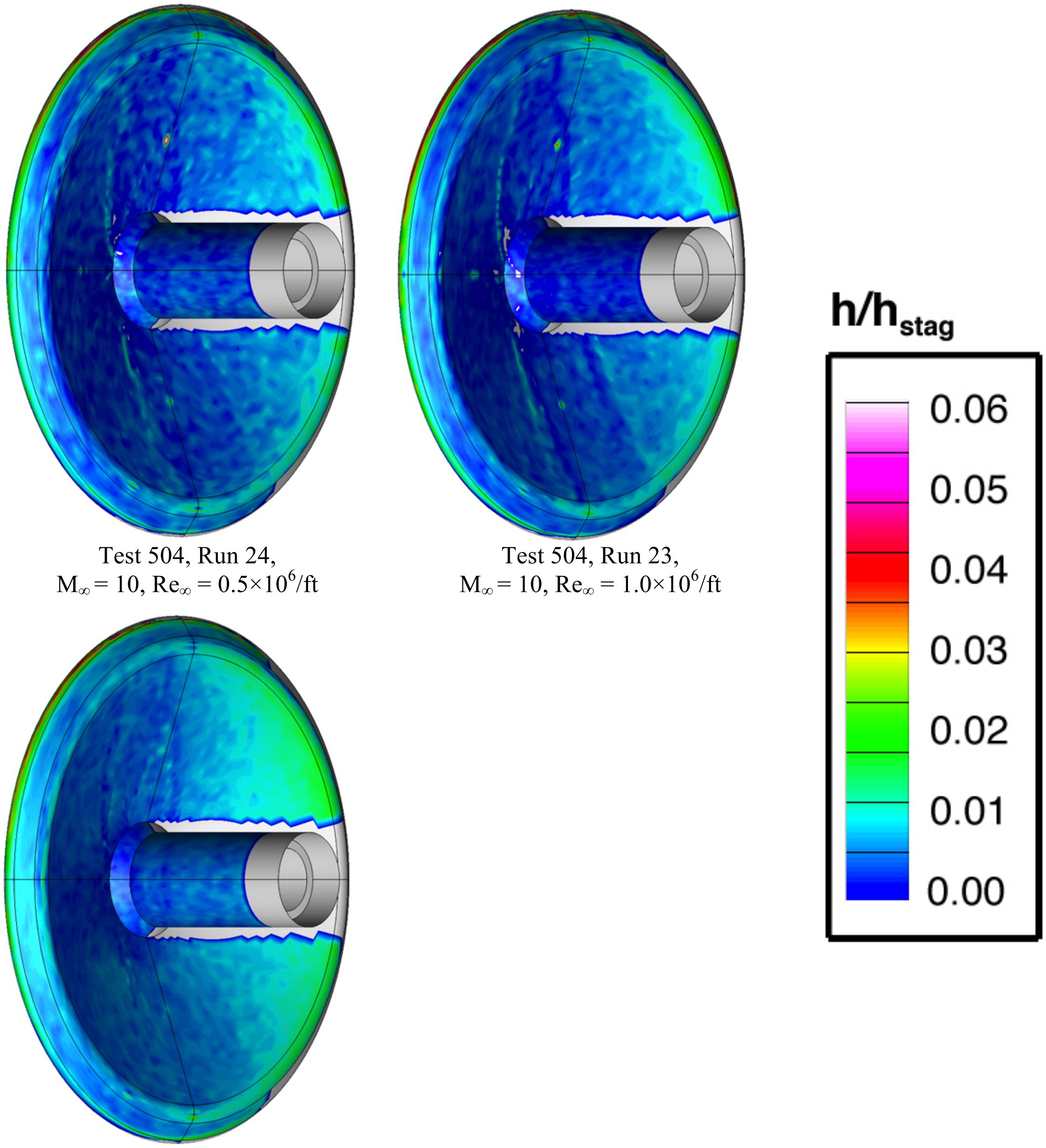

Test 504, Run 24,
$M_\infty = 10$, $Re_\infty = 0.5\times10^6$/ft

Test 504, Run 23,
$M_\infty = 10$, $Re_\infty = 1.0\times10^6$/ft

Test 504, Run 25,
$M_\infty = 10$, $Re_\infty = 2.0\times10^6$/ft

Figure 29. Back-face heating images: Reynolds number effects, $M_\infty = 10$, $\alpha = -5$ deg.

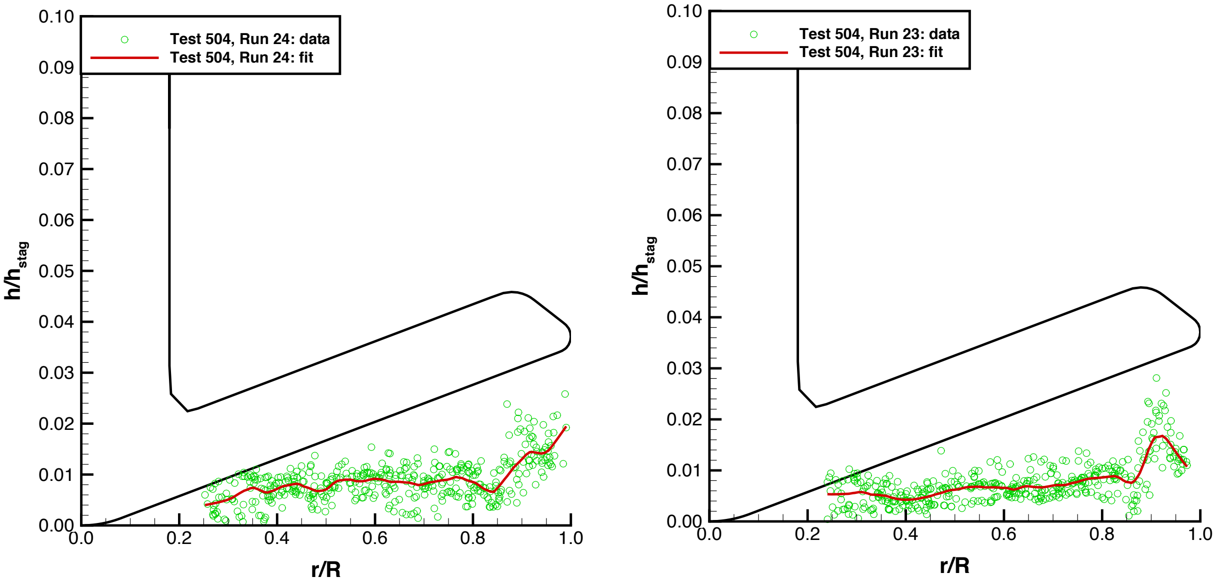

Test 504, Run 24,
$M_\infty = 10$, $Re_\infty = 0.5\times10^6$/ft

Test 504, Run 23,
$M_\infty = 10$, $Re_\infty = 1.0\times10^6$/ft

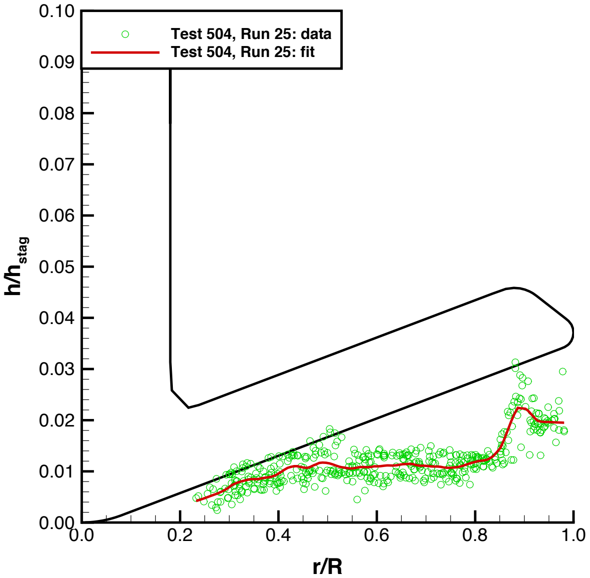

Test 504, Run 25,
$M_\infty = 10$, $Re_\infty = 2.0\times10^6$/ft

Data from $\phi = -20$ deg to +20 deg rays

Figure 30. Back-face heating data: Reynolds number effects, $M_\infty = 10$, $\alpha = -5$ deg.

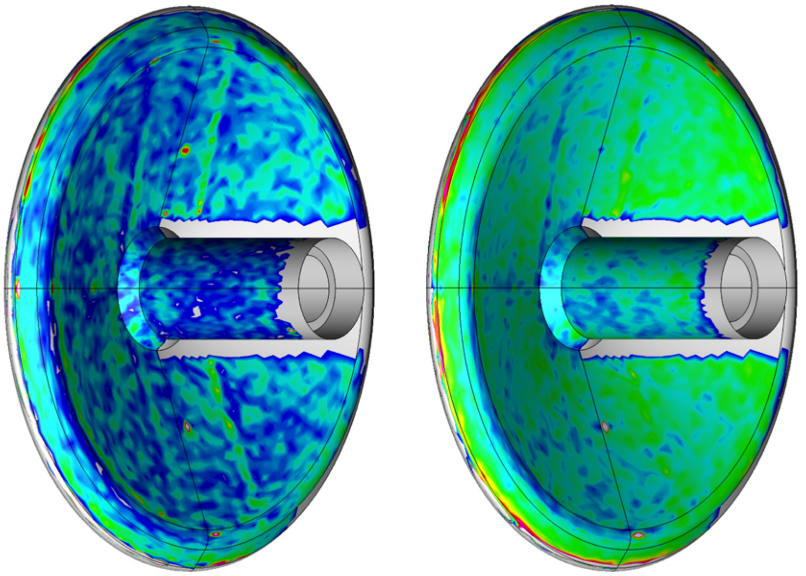

Test 7002, Run 16,
$M_\infty = 6$, $Re_\infty = 1.1\times10^6$/ft

Test 7002, Run 19,
$M_\infty = 6$, $Re_\infty = 2.1\times10^6$/ft

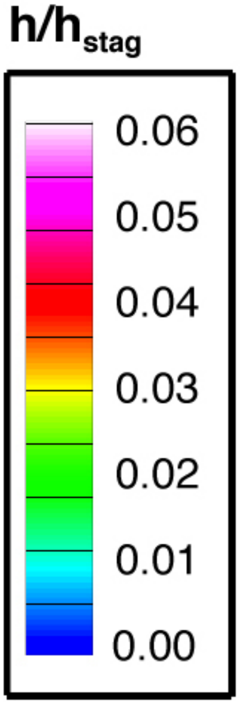

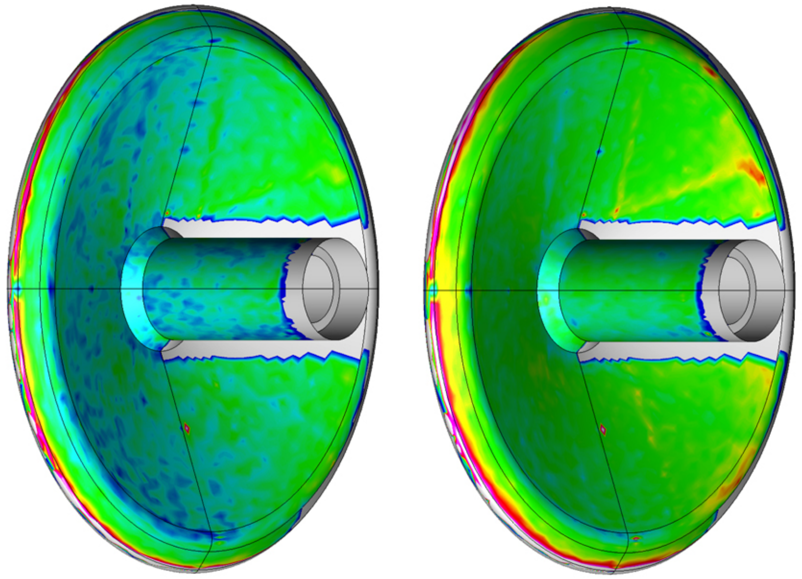

Test 7002, Run 18,
$M_\infty = 6$, $Re_\infty = 3.1\times10^6$/ft

Test 7002, Run 17,
$M_\infty = 6$, $Re_\infty = 3.9\times10^6$/ft

Figure 31. Back-face heating images: Reynolds number effects, $M_\infty = 6$, $\alpha = -5$ deg.

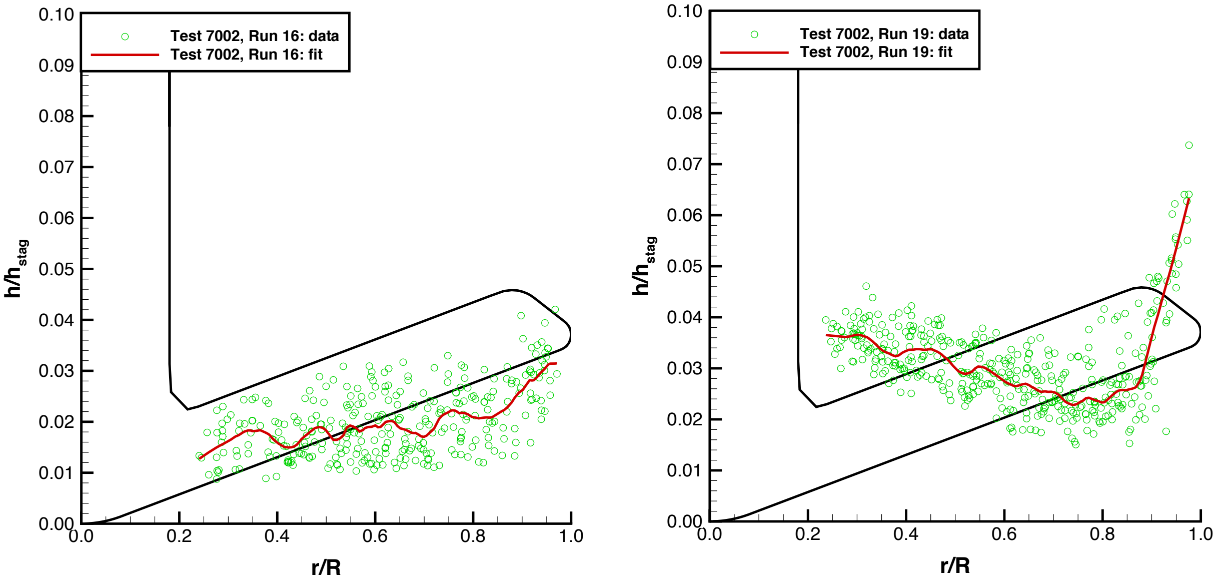

Test 7002, Run 16,
$M_\infty = 6$, $Re_\infty = 1.1\times10^6$/ft

Test 7002, Run 19,
$M_\infty = 6$, $Re_\infty = 2.1\times10^6$/ft

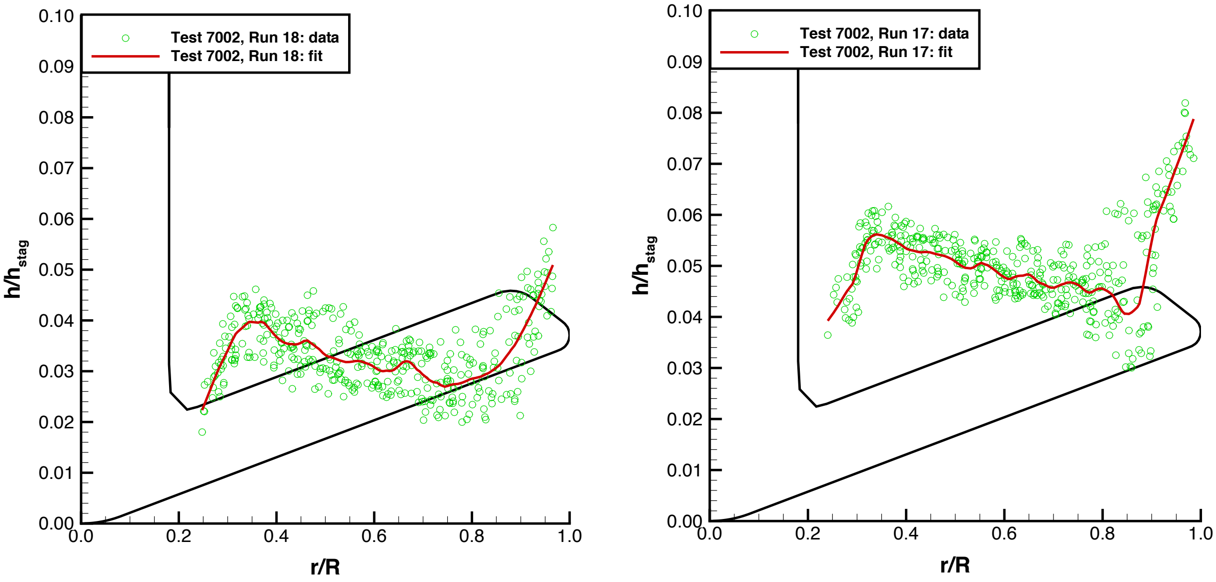

Test 7002, Run 18,
$M_\infty = 6$, $Re_\infty = 3.1\times10^6$/ft

Test 7002, Run 17,
$M_\infty = 6$, $Re_\infty = 3.9\times10^6$/ft

Data from $\phi = -20$ deg to +20 deg rays

Figure 32. Back-face heating data: Reynolds number effects, $M_\infty = 6$, $\alpha = -5$ deg.

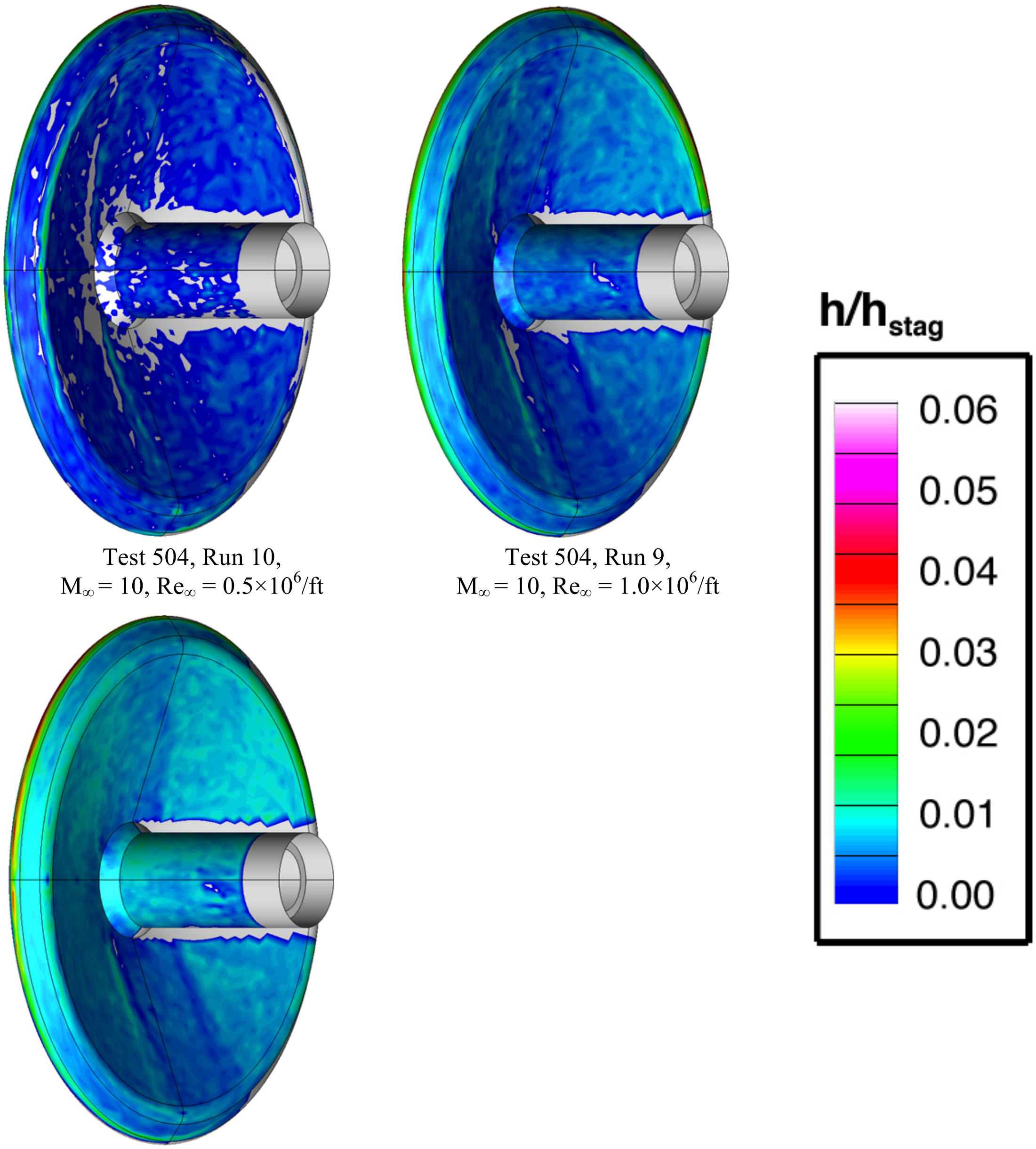

Test 504, Run 10,
$M_\infty = 10$, $Re_\infty = 0.5\times10^6$/ft

Test 504, Run 9,
$M_\infty = 10$, $Re_\infty = 1.0\times10^6$/ft

Test 504, Run 11,
$M_\infty = 10$, $Re_\infty = 2.0\times10^6$/ft

Figure 33. Back-face heating images: Reynolds number effects, $M_\infty = 10$, $\alpha = 0$ deg.

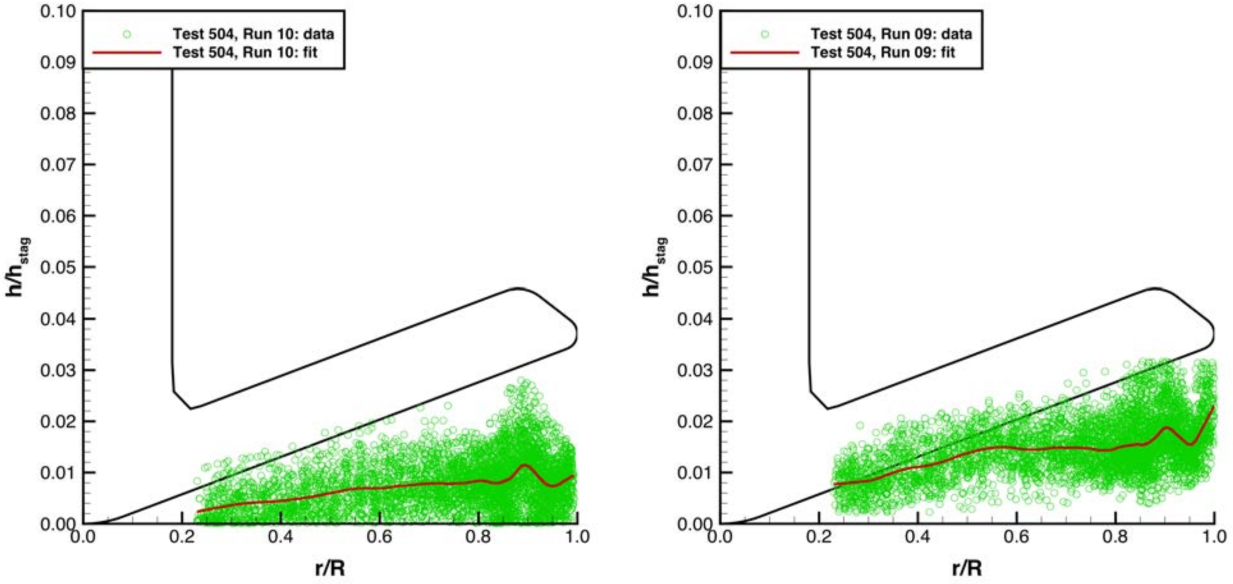

Test 504, Run 10,
$M_\infty = 10$, $Re_\infty = 0.5\times10^6$/ft

Test 504, Run 9,
$M_\infty = 10$, $Re_\infty = 1.0\times10^6$/ft

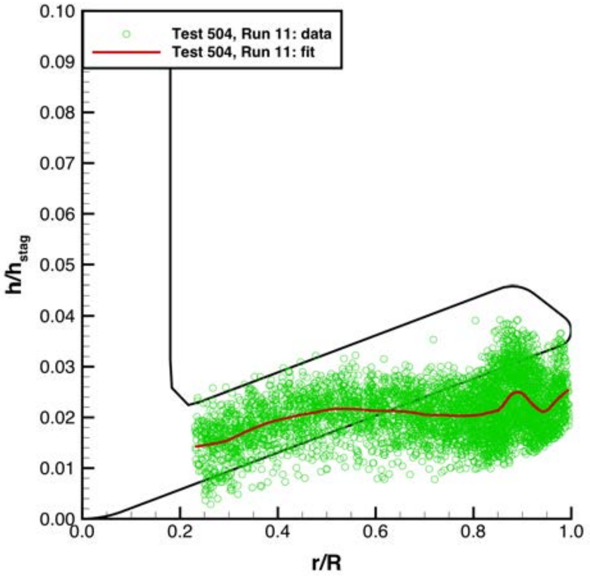

Test 504, Run 11,
$M_\infty = 10$, $Re_\infty = 2.0\times10^6$/ft

Data from all rays $\phi = 0$ deg to ±180 deg

Figure 34. Back-face heating data: Reynolds number effects, $M_\infty = 10$, $\alpha = 0$ deg.

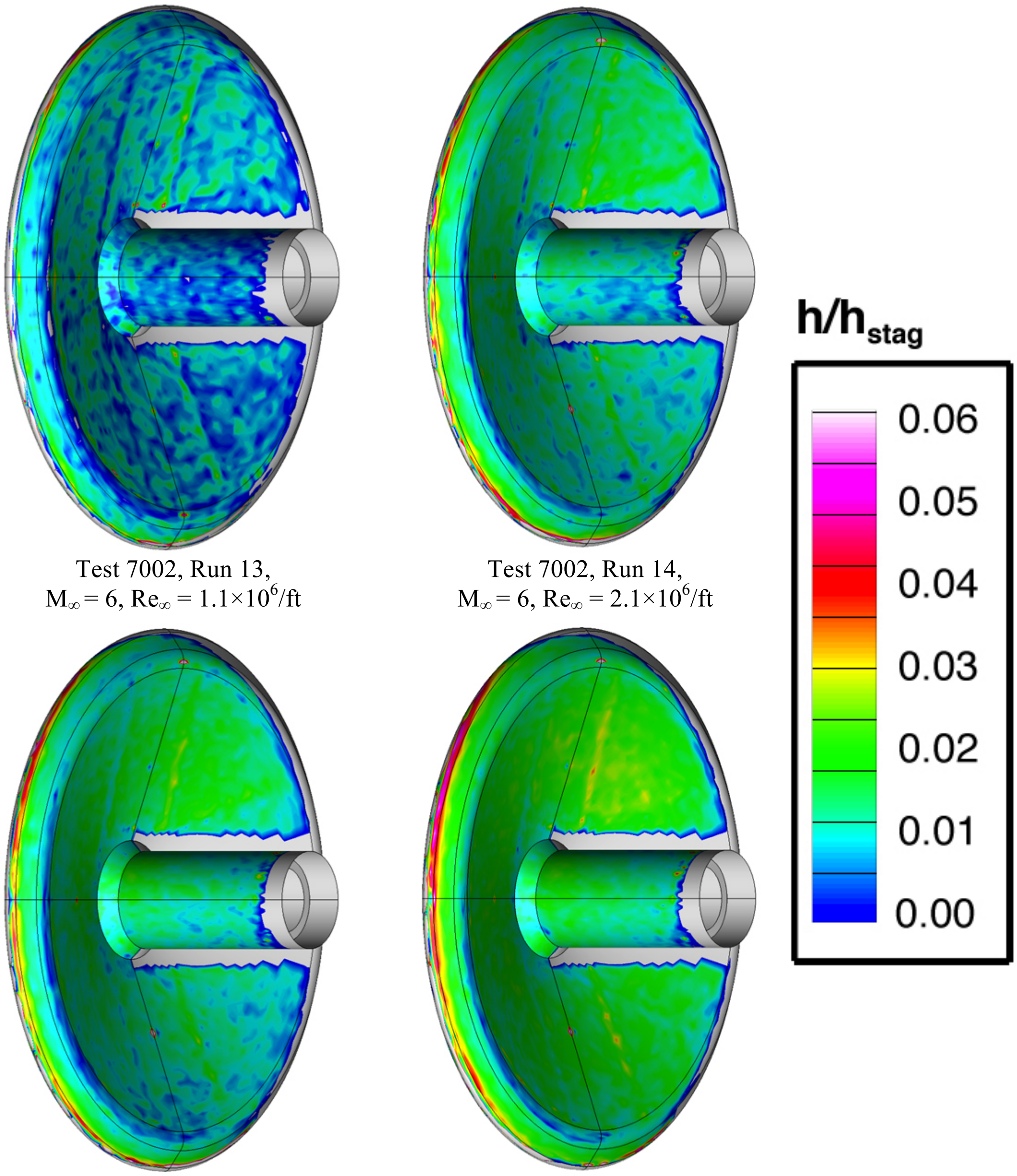

Test 7002, Run 13,
$M_\infty = 6$, $Re_\infty = 1.1\times10^6$/ft

Test 7002, Run 14,
$M_\infty = 6$, $Re_\infty = 2.1\times10^6$/ft

Test 7002, Run 15,
$M_\infty = 6$, $Re_\infty = 3.1\times10^6$/ft

Test 7002, Run 12,
$M_\infty = 6$, $Re_\infty = 3.9\times10^6$/ft

Figure 35. Back-face heating images: Reynolds number effects, $M_\infty = 6$, $\alpha = 0$ deg.

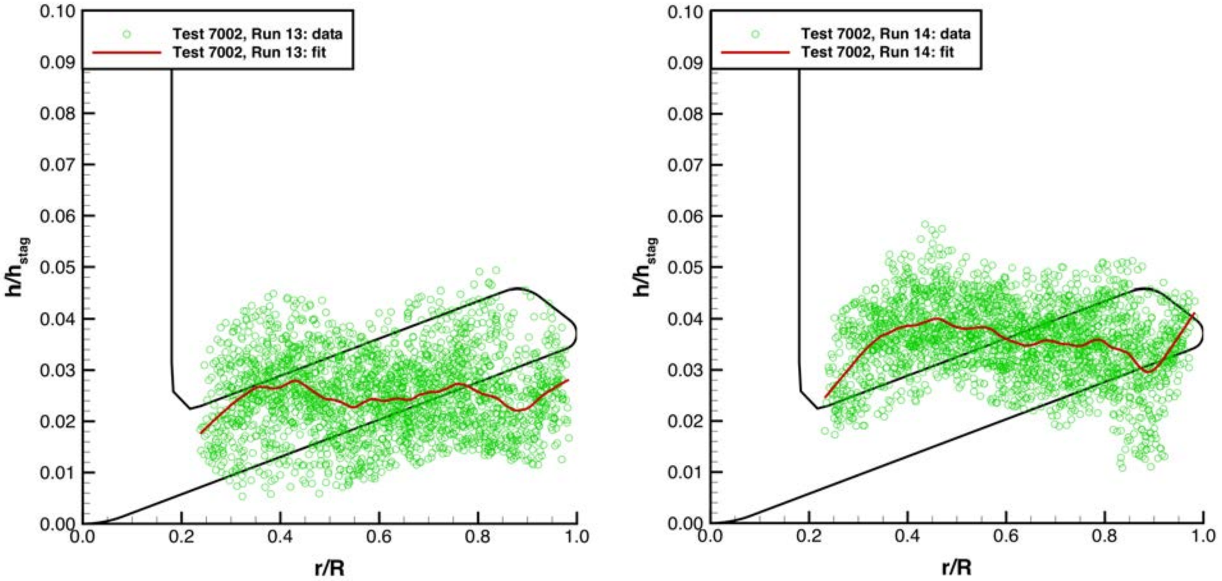

Test 7002, Run 13,
$M_\infty = 6$, $Re_\infty = 1.1\times10^6$/ft

Test 7002, Run 14,
$M_\infty = 6$, $Re_\infty = 2.1\times10^6$/ft

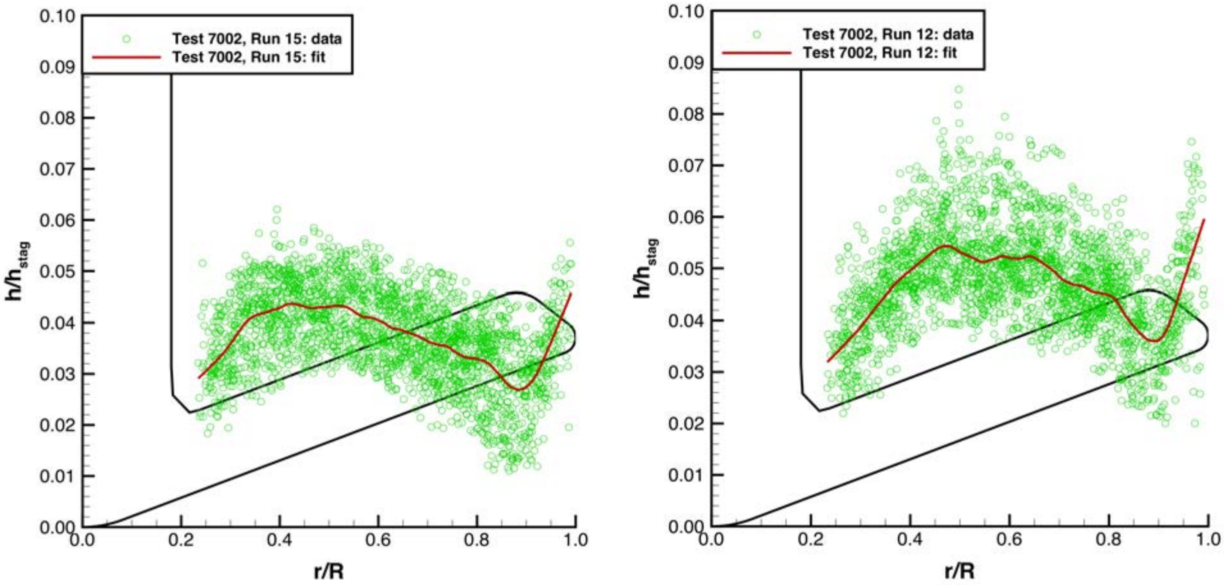

Test 7002, Run 15,
$M_\infty = 6$, $Re_\infty = 3.1\times10^6$/ft

Test 7002, Run 12,
$M_\infty = 6$, $Re_\infty = 3.9\times10^6$/ft

Data from all rays $\phi = 0$ deg to ±180 deg

Figure 36. Back-face heating data: Reynolds number effects, $M_\infty = 6$, $\alpha = 0$ deg.

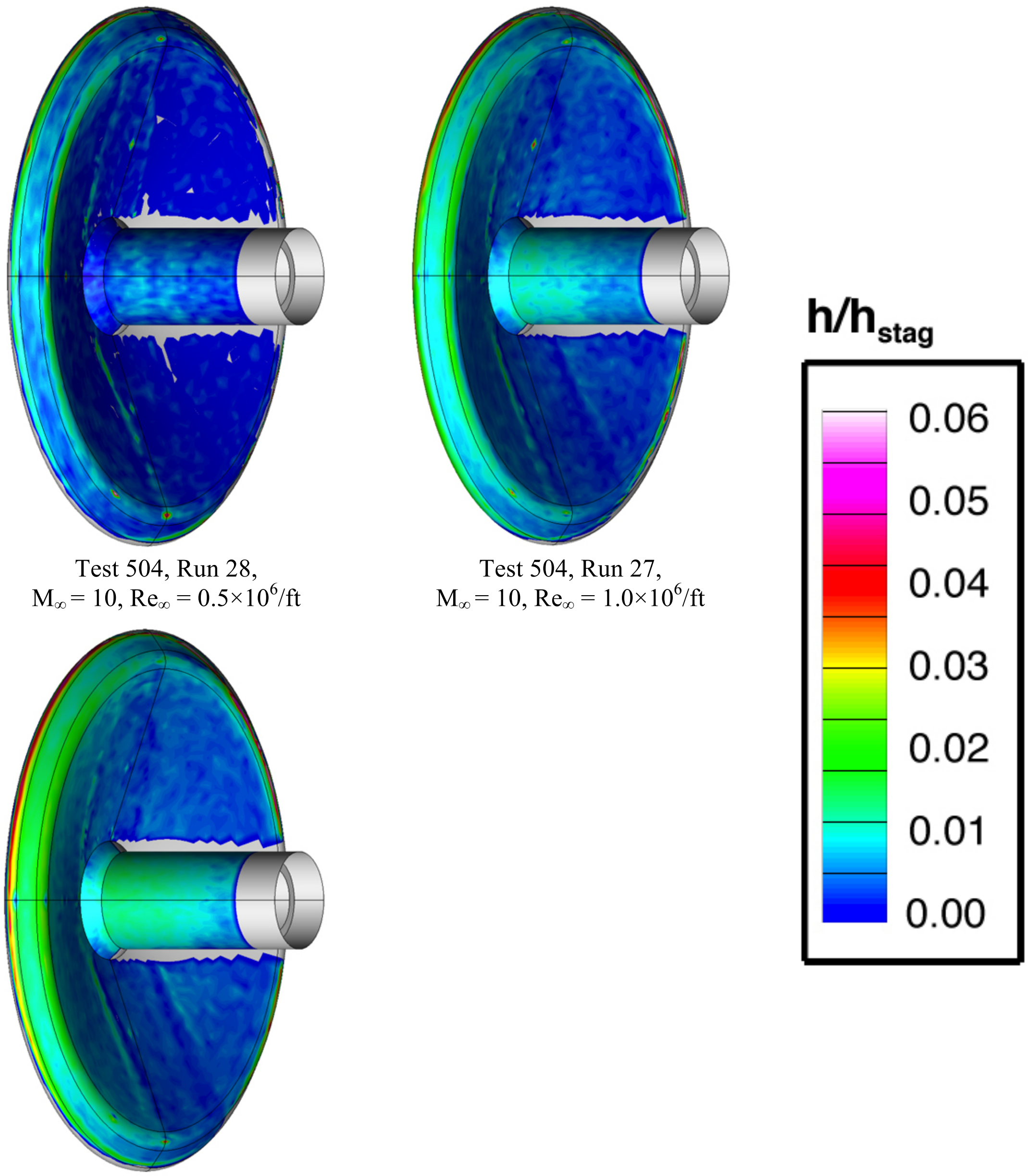

Test 504, Run 28,
$M_\infty = 10$, $Re_\infty = 0.5\times10^6$/ft

Test 504, Run 27,
$M_\infty = 10$, $Re_\infty = 1.0\times10^6$/ft

Test 504, Run 29,
$M_\infty = 10$, $Re_\infty = 2.0\times10^6$/ft

Figure 37. Back-face heating images: Reynolds number effects, $M_\infty = 10$, $\alpha = +5$ deg.

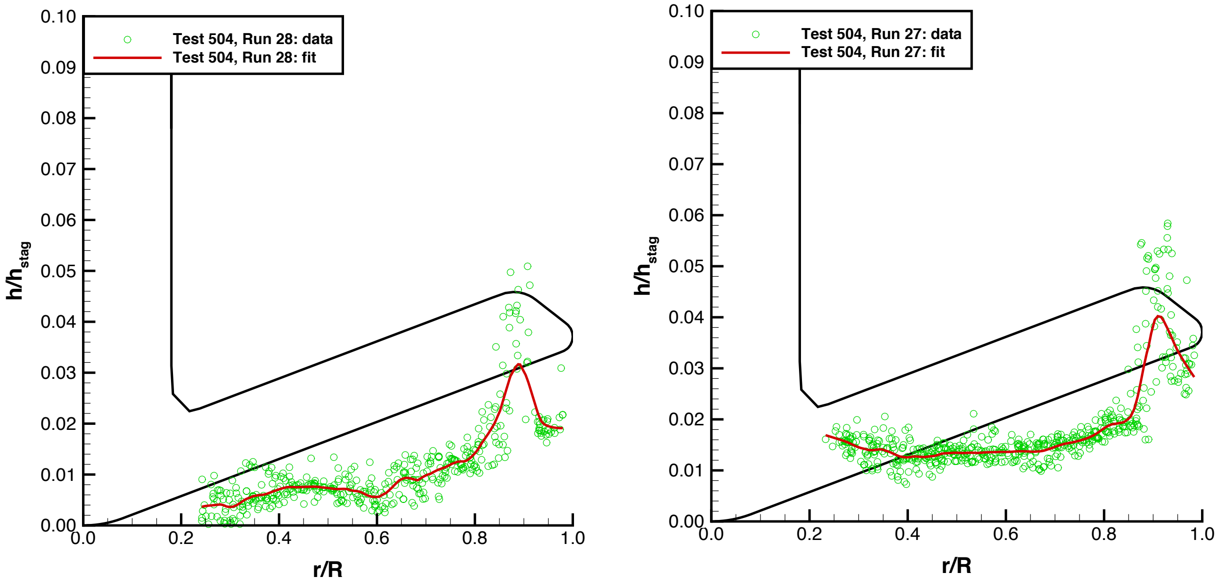

Test 504, Run 28,
$M_\infty = 10$, $Re_\infty = 0.5\times10^6$/ft

Test 504, Run 27,
$M_\infty = 10$, $Re_\infty = 1.0\times10^6$/ft

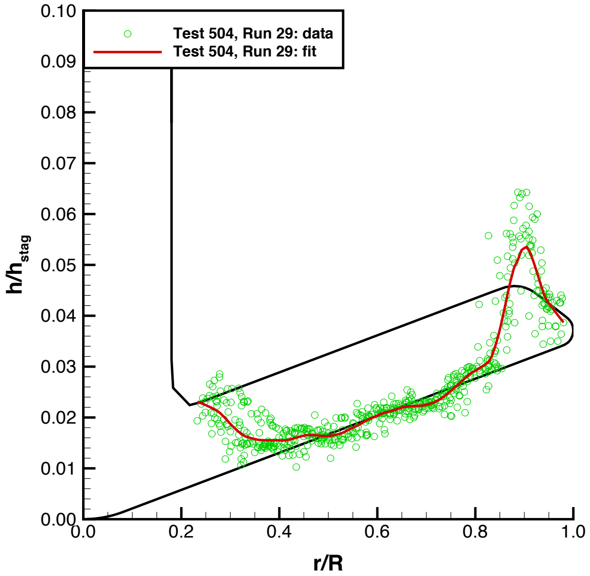

Test 504, Run 29,
$M_\infty = 10$, $Re_\infty = 2.0\times10^6$/ft

Data from $\phi = -20$ deg to +20 deg rays

Figure 38. Back-face heating data: Reynolds number effects, $M_\infty = 10$, $\alpha = +5$ deg.

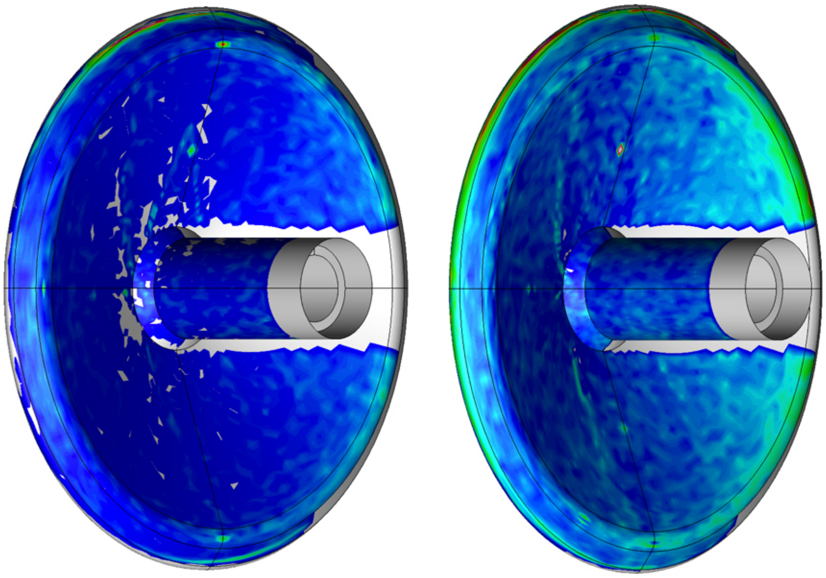

Test 504, Run 34,
$M_\infty = 10$, $\alpha = -10$ deg

Test 504, Run 24,
$M_\infty = 10$, $\alpha = -5$ deg

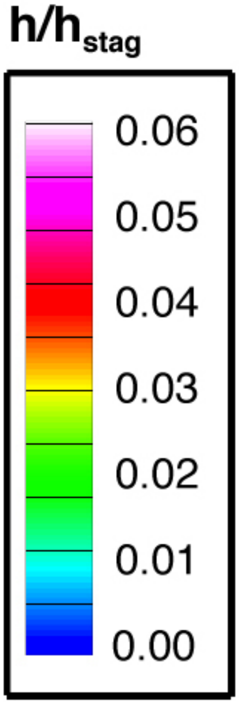

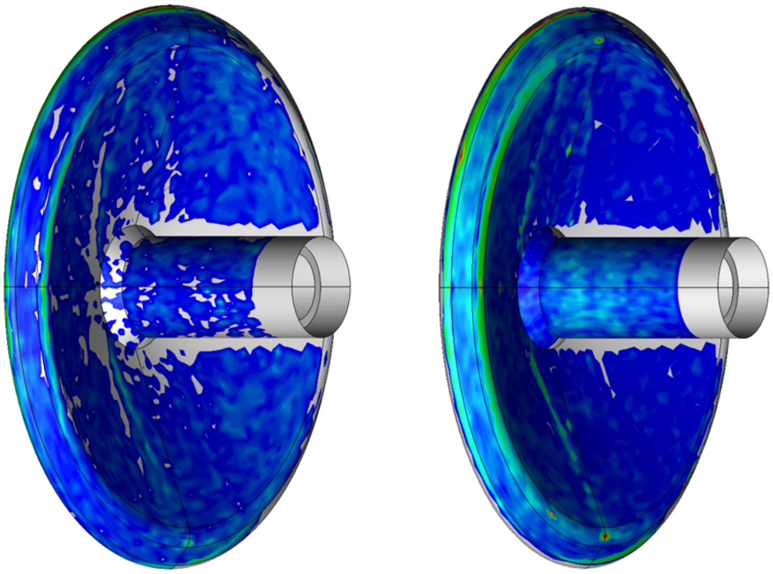

Test 504, Run 10,
$M_\infty = 10$, $\alpha = 0$ deg

Test 504, Run 28,
$M_\infty = 10$, $\alpha = +5$ deg

Figure 39. Back-face heating images: angle-of-attack effects, $M_\infty = 10$, $Re_\infty = 0.5\times10^6$/ft.

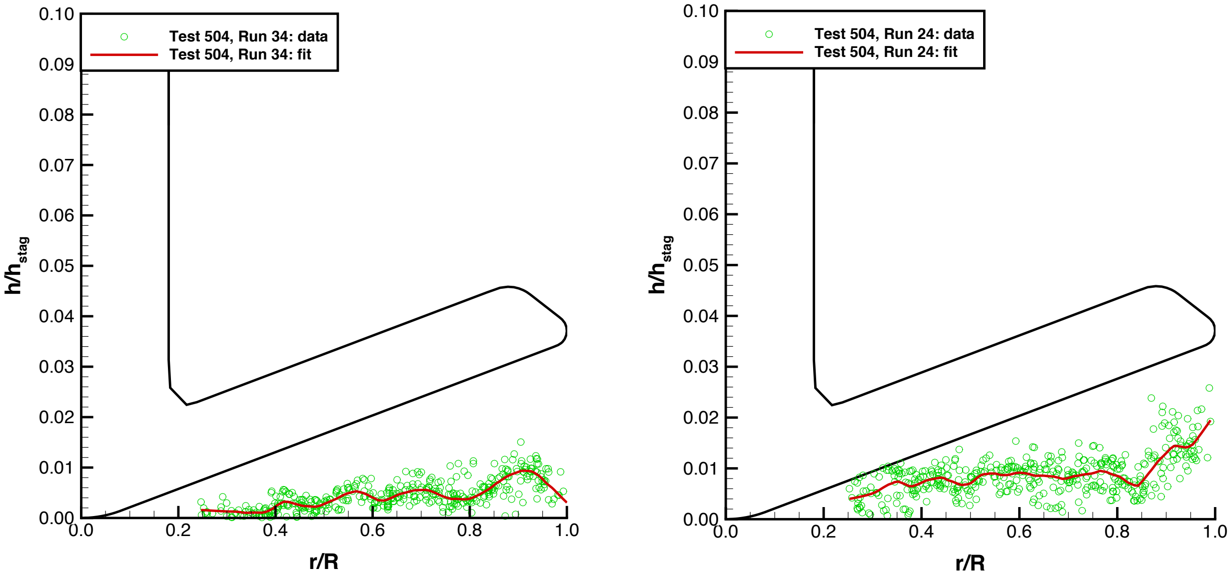

Test 504, Run 34,
$M_\infty = 10$, α = –10 deg

Test 504, Run 24,
$M_\infty = 10$, α = –5 deg

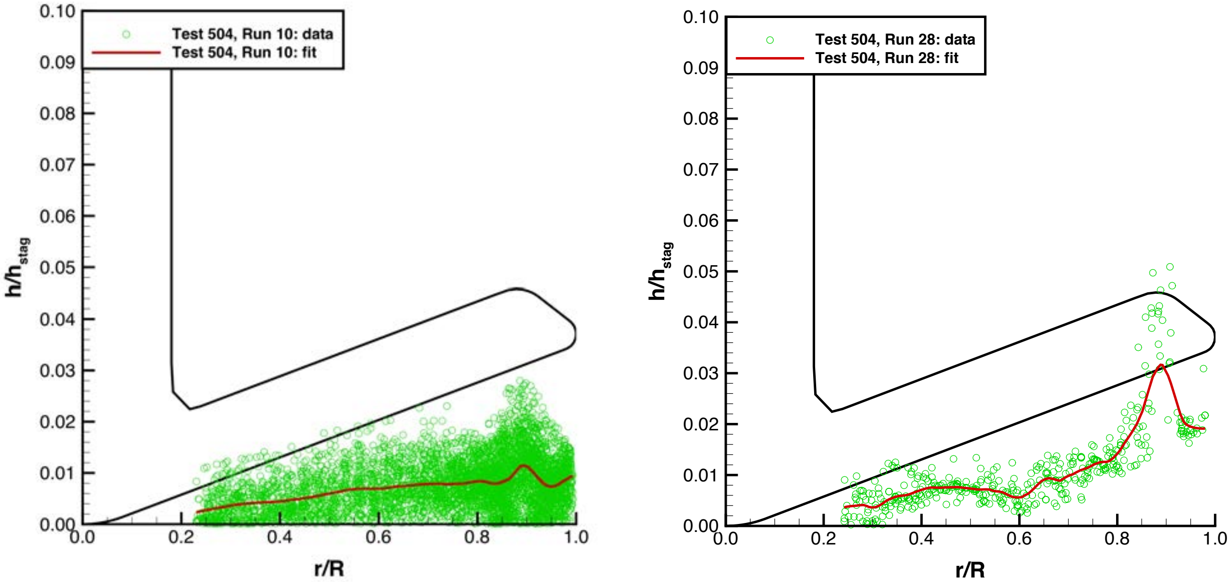

Test 504, Run 10,
$M_\infty = 10$, α = 0 deg

Test 504, Run 28,
$M_\infty = 10$, α = +5 deg

Data from ϕ = –20 deg to +20 deg rays

Figure 40. Back-face heating data: angle-of-attack effects, $M_\infty = 10$, $Re_\infty = 0.5\times10^6$/ft.

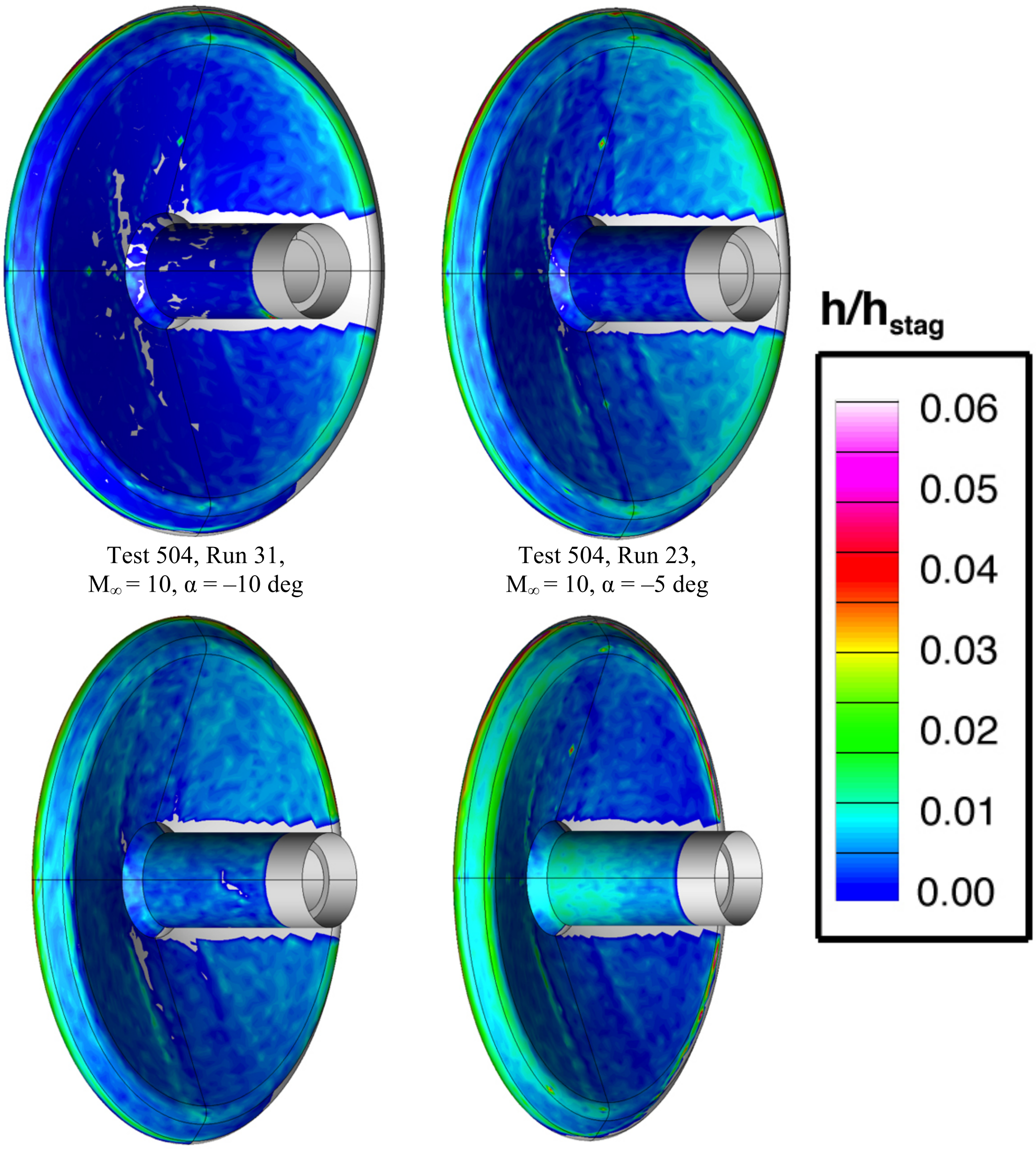

Test 504, Run 31,
$M_\infty = 10$, $\alpha = -10$ deg

Test 504, Run 23,
$M_\infty = 10$, $\alpha = -5$ deg

Test 504, Run 9,
$M_\infty = 10$, $\alpha = 0$ deg

Test 504, Run 27,
$M_\infty = 10$, $\alpha = +5$ deg

Figure 41. Back-face heating images: angle-of-attack effects, $M_\infty = 10$, $Re_\infty = 1.0\times10^6$/ft.

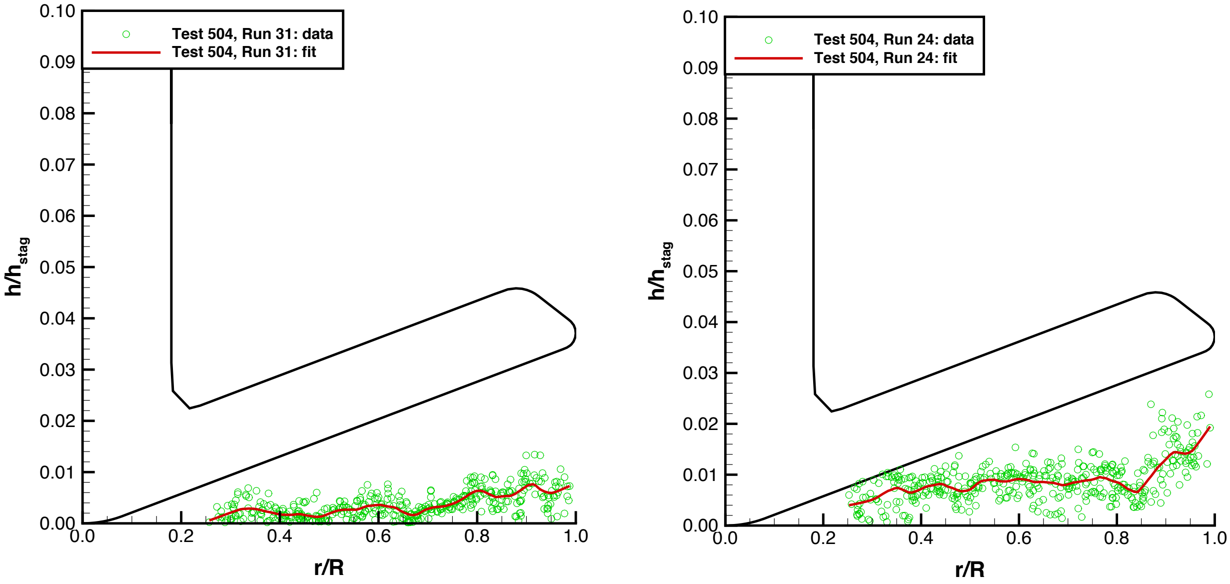

Test 504, Run 31,
M$_\infty$ = 10, α = –10 deg

Test 504, Run 23,
M$_\infty$ = 10, α = –5 deg

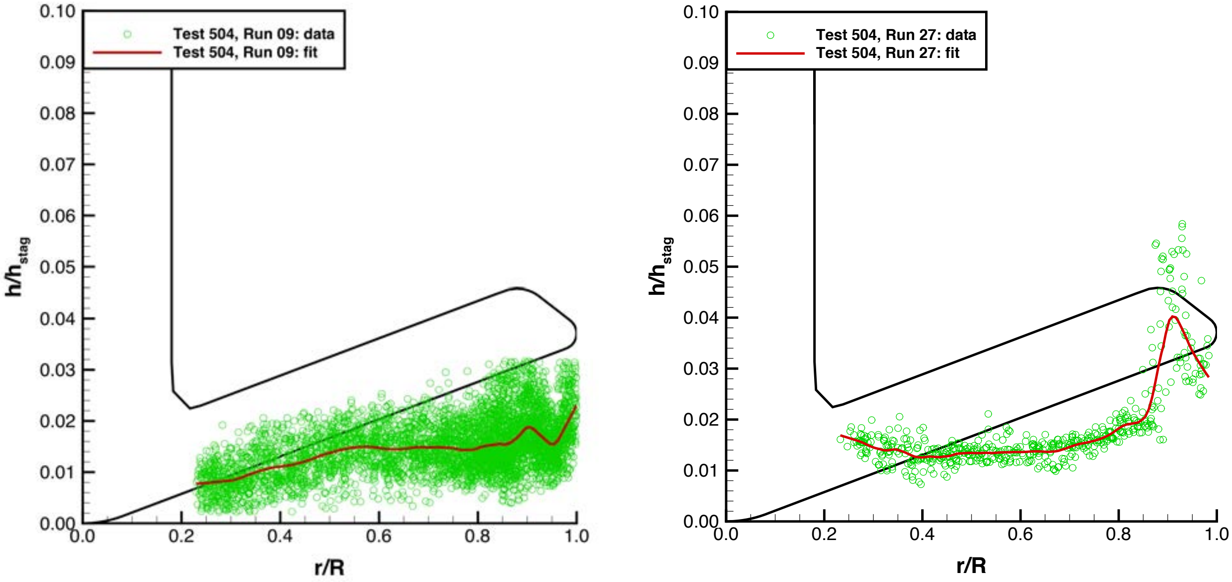

Test 504, Run 9,
M$_\infty$ = 10, α = 0 deg

Test 504, Run 27,
M$_\infty$ = 10, α = +5 deg

Data from ϕ = –20 deg to +20 deg rays

Figure 42. Back-face heating data: angle-of-attack effects, M$_\infty$ = 10, Re$_\infty$ = 1.0×10^6/ft.

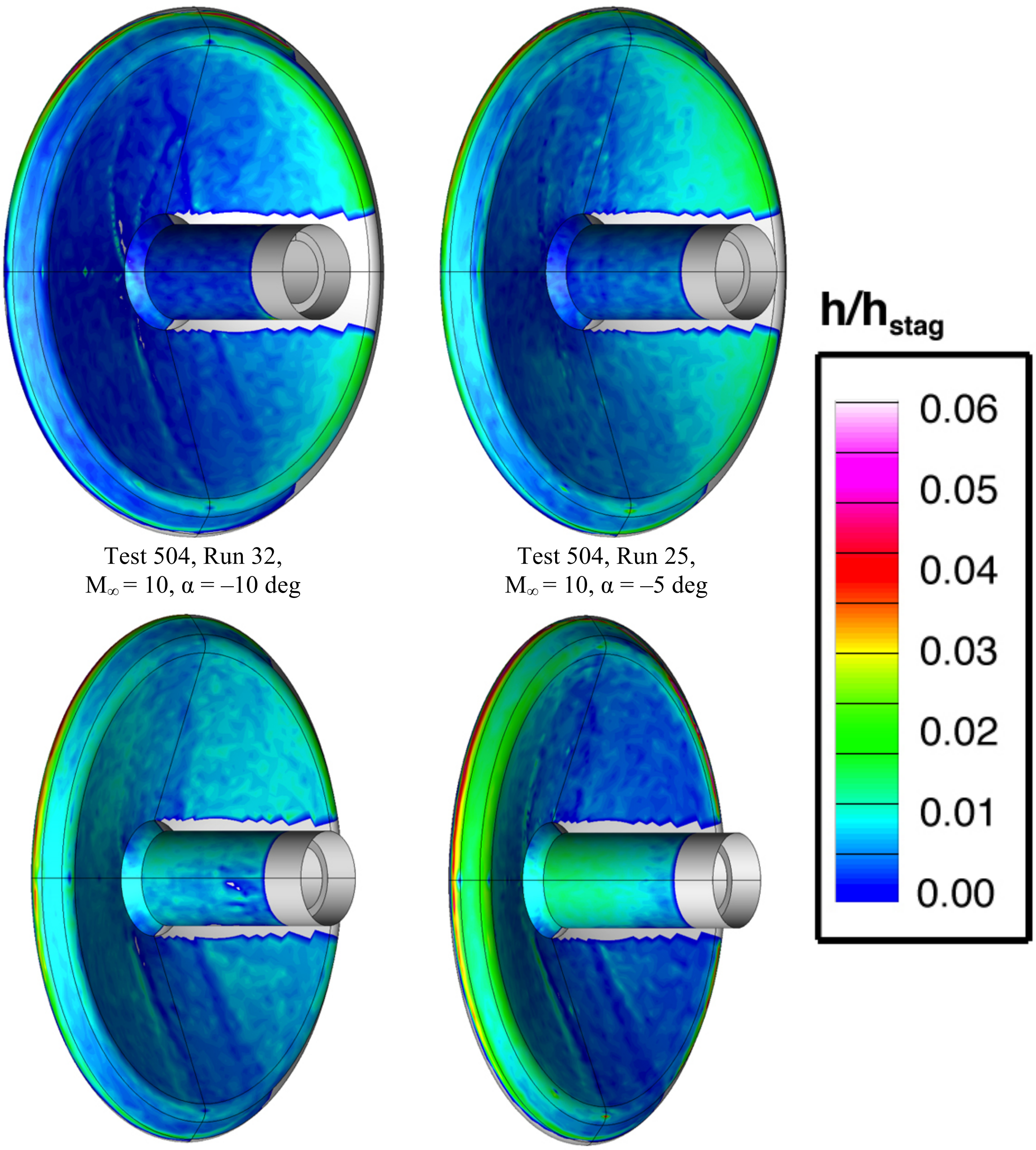

Test 504, Run 32,
$M_\infty = 10$, $\alpha = -10$ deg

Test 504, Run 25,
$M_\infty = 10$, $\alpha = -5$ deg

Test 504, Run 11,
$M_\infty = 10$, $\alpha = 0$ deg

Test 504, Run 29,
$M_\infty = 10$, $\alpha = +5$ deg

Figure 43. Back-face heating images: angle-of-attack effects, $M_\infty = 10$, $Re_\infty = 2.0\times10^6$/ft.

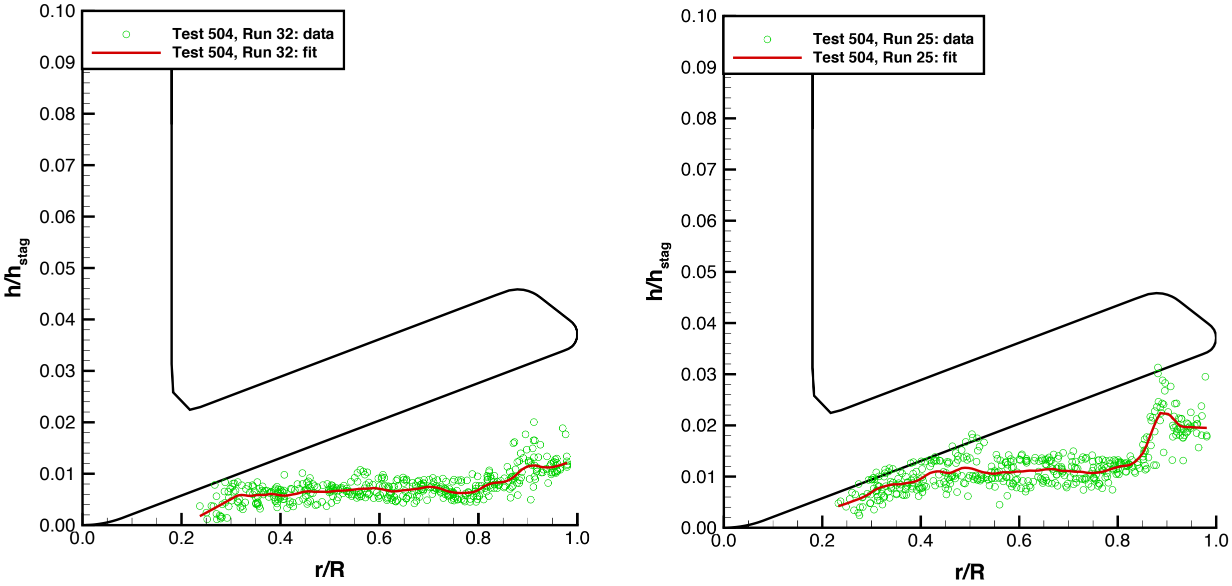

Test 504, Run 32,
$M_\infty = 10$, $\alpha = -10$ deg

Test 504, Run 25,
$M_\infty = 10$, $\alpha = -5$ deg

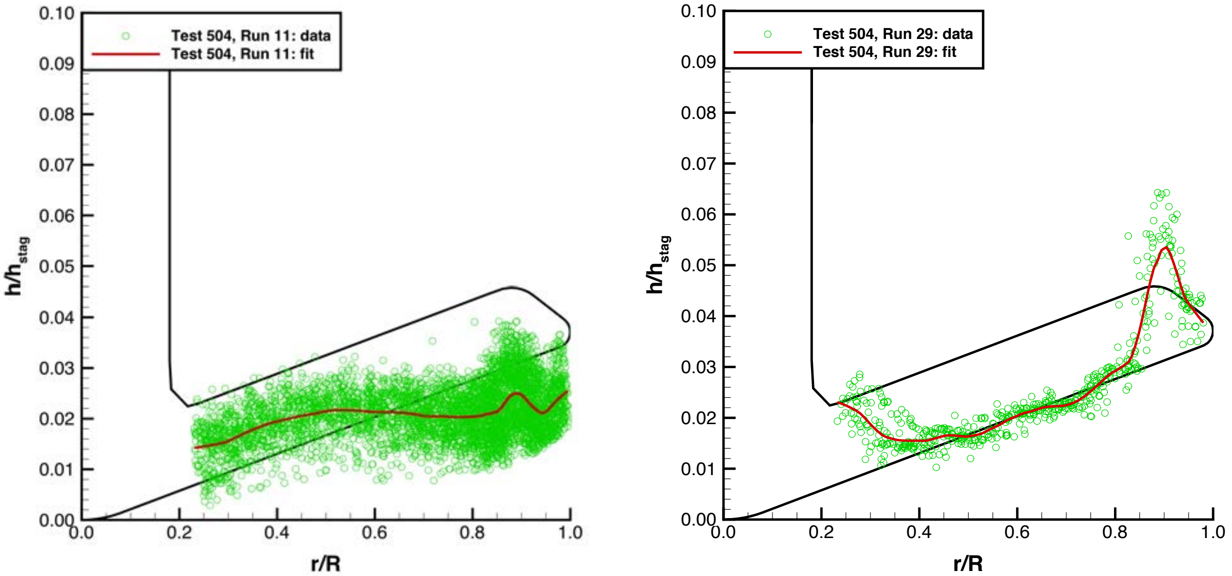

Test 504, Run 11,
$M_\infty = 10$, $\alpha = 0$ deg

Test 504, Run 29,
$M_\infty = 10$, $\alpha = +5$ deg

Data from $\phi = -20$ deg to +20 deg rays

Figure 44. Back-face heating data: angle-of-attack effects, $M_\infty = 10$, $Re_\infty = 2.0\times10^6$/ft.

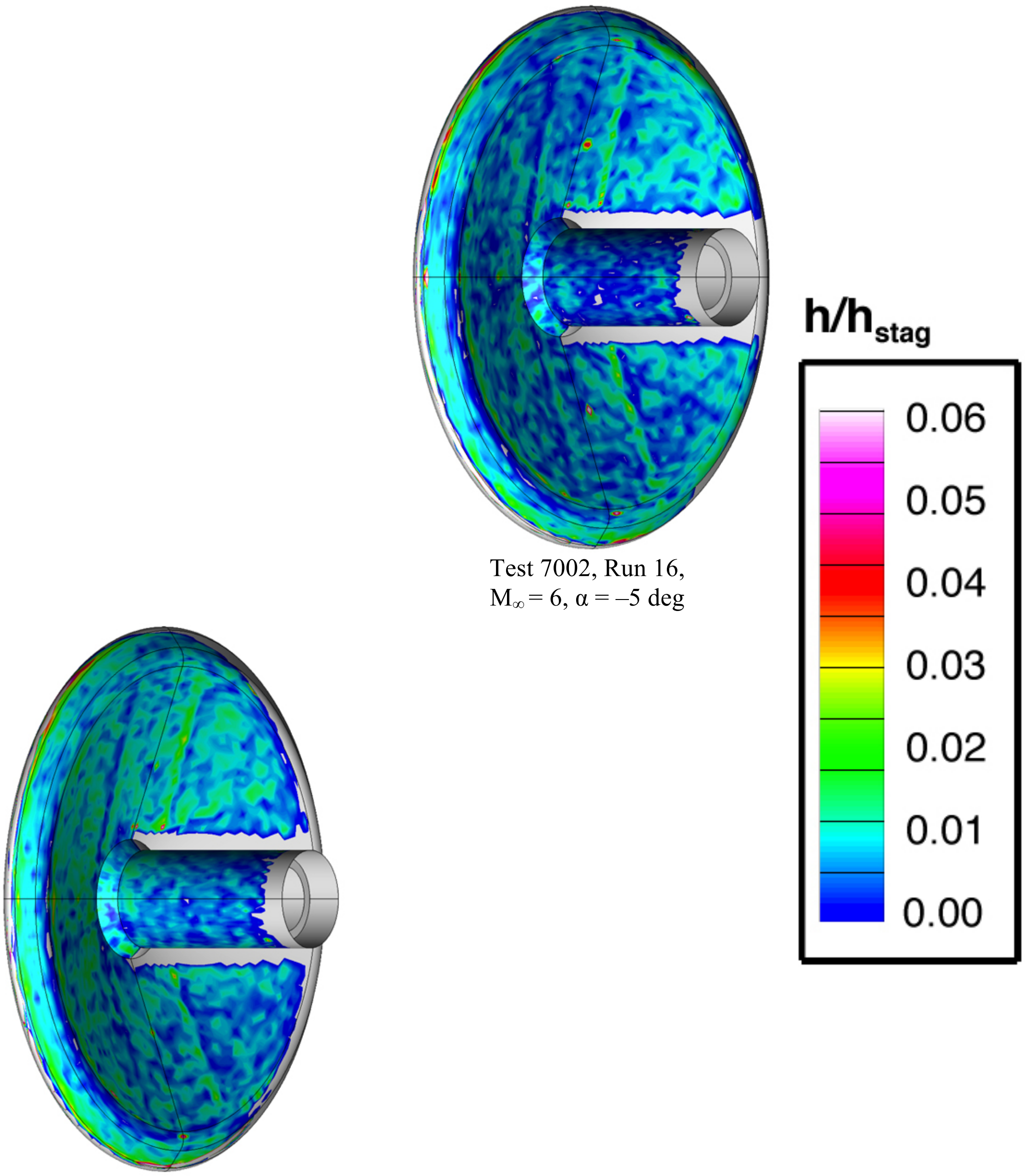

Test 7002, Run 16,
$M_\infty = 6$, $\alpha = -5$ deg

Test 7002, Run 13,
$M_\infty = 6$, $\alpha = 0$ deg

Figure 45. Back-face heating images: angle-of-attack effects, $M_\infty = 6$, $Re_\infty = 1.1\times10^6$/ft.

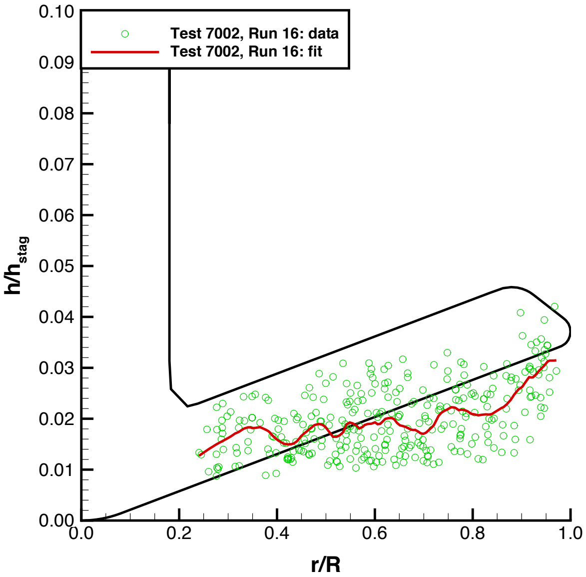

Test 7002, Run 16,
$M_\infty = 6$, $\alpha = -5$ deg

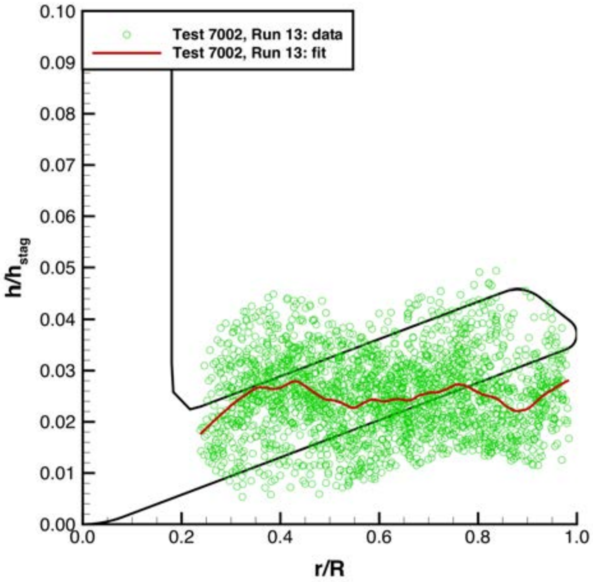

Test 7002, Run 13,
$M_\infty = 6$, $\alpha = 0$ deg

Data from $\phi = -20$ deg to +20 deg rays

Figure 46. Back-face heating data: angle-of-attack effects, $M_\infty = 6$, $Re_\infty = 1.1\times10^6$/ft.

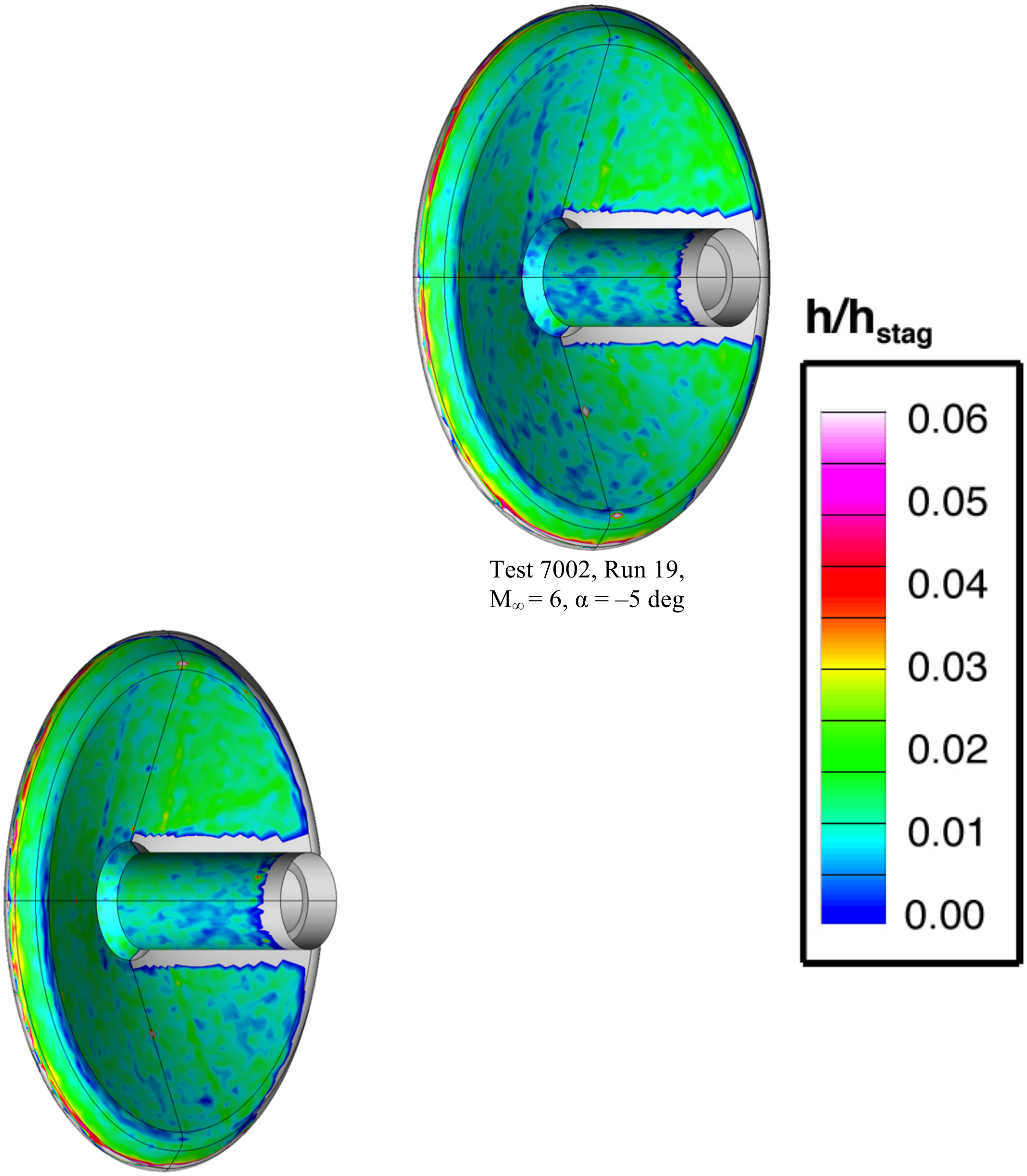

Test 7002, Run 19,
$M_\infty = 6$, $\alpha = -5$ deg

Test 7002, Run 14,
$M_\infty = 6$, $\alpha = 0$ deg

Figure 47. Back-face heating images: angle-of-attack effects, $M_\infty = 6$, $Re_\infty = 2.1 \times 10^6$/ft.

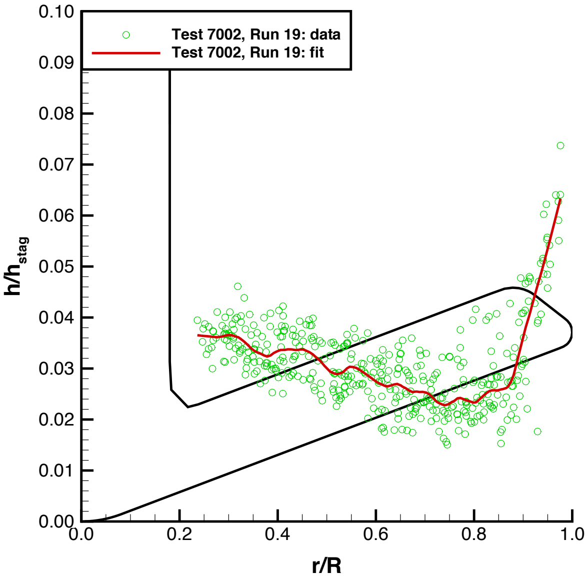

Test 7002, Run 19,
$M_\infty = 6$, $\alpha = -5$ deg

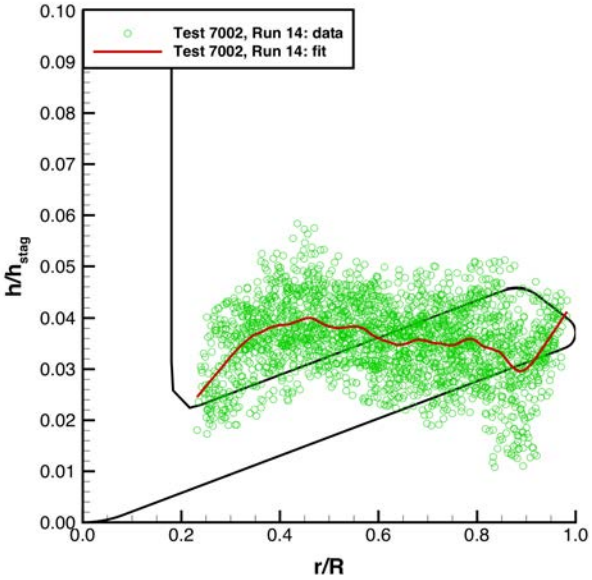

Test 7002, Run 14,
$M_\infty = 6$, $\alpha = 0$ deg

Data from $\phi = -20$ deg to +20 deg rays

Figure 48. Back-face heating data: angle-of-attack effects, $M_\infty = 6$, $Re_\infty = 2.1 \times 10^6$/ft.

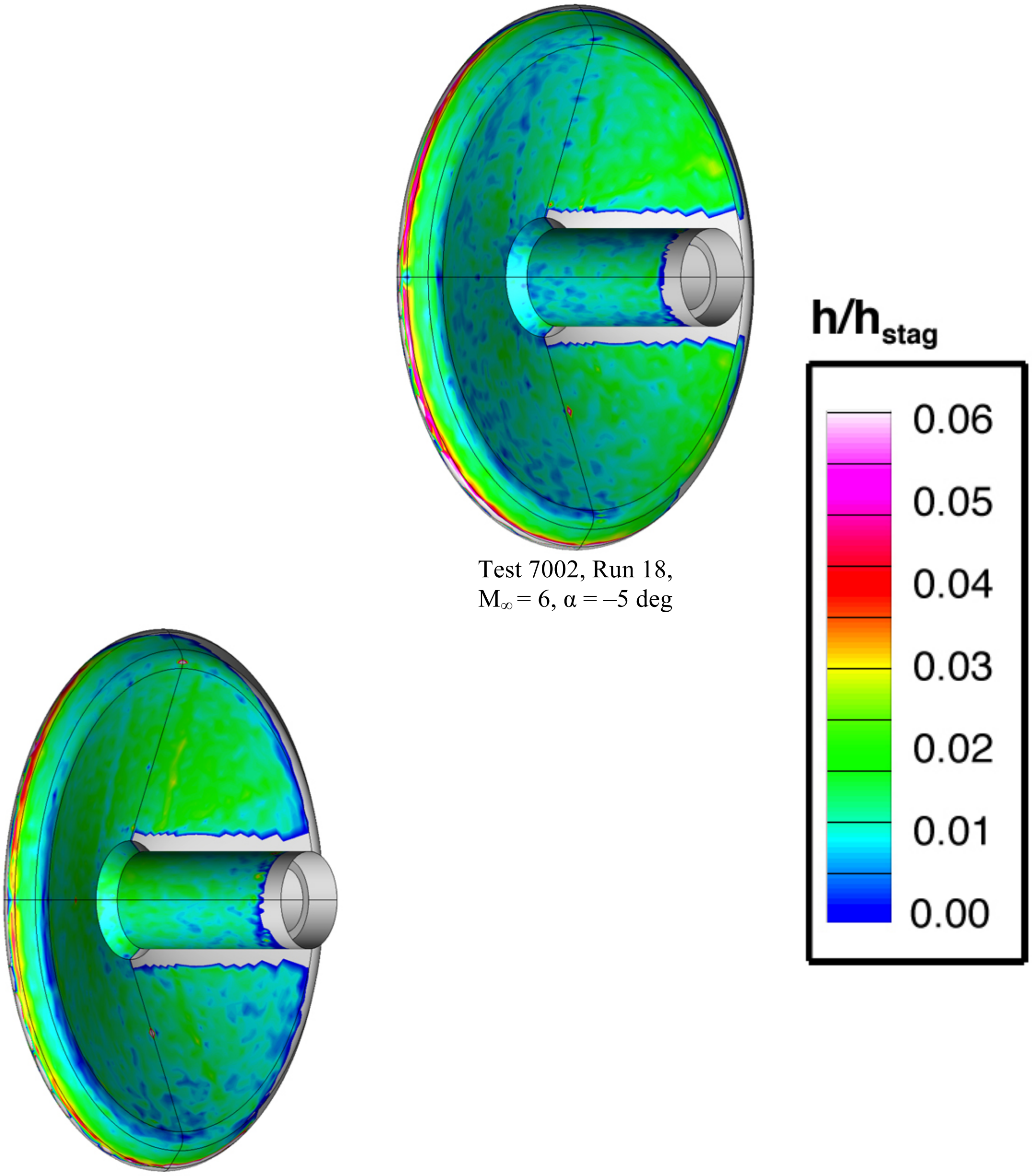

Test 7002, Run 18,
$M_\infty = 6$, $\alpha = -5$ deg

Test 7002, Run 15,
$M_\infty = 6$, $\alpha = 0$ deg

Figure 49. Back-face heating images: angle-of-attack effects, $M_\infty = 6$, $Re_\infty = 3.1\times10^6$/ft.

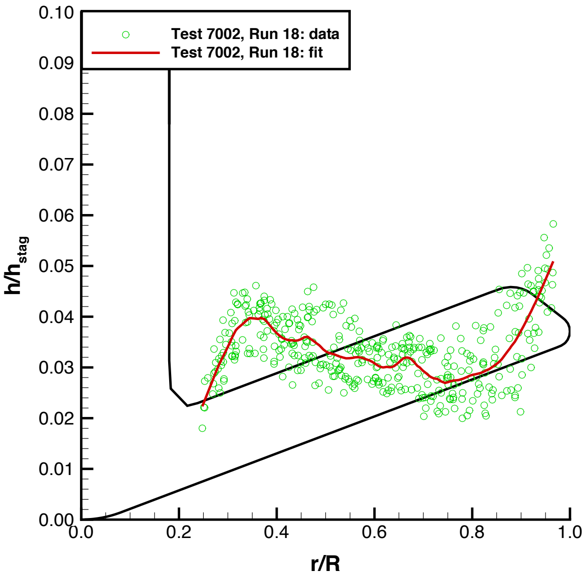

Test 7002, Run 18,
$M_\infty = 6$, $\alpha = -5$ deg

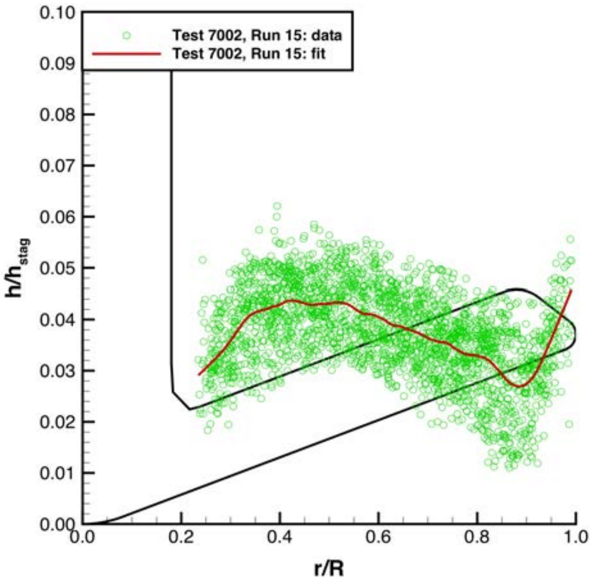

Test 7002, Run 15,
$M_\infty = 6$, $\alpha = 0$ deg

Data from ϕ = –20 deg to +20 deg rays

Figure 50. Back-face heating data: angle-of-attack effects, $M_\infty = 6$, $Re_\infty = 3.1 \times 10^6$/ft.

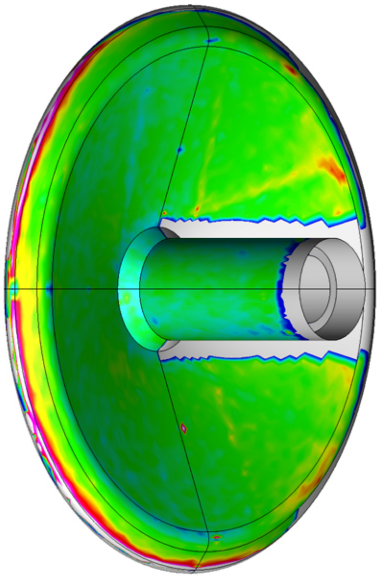

Test 7002, Run 17,
$M_\infty = 6$, $\alpha = -5$ deg

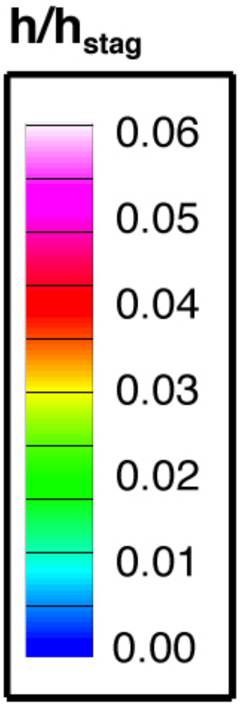

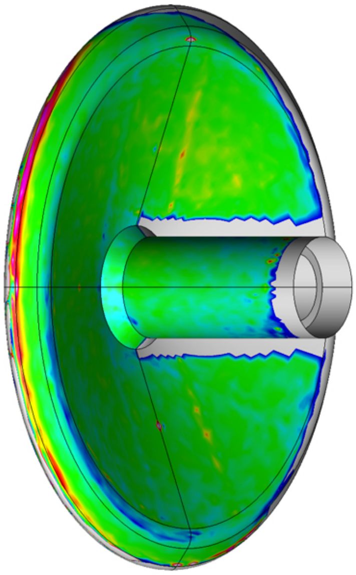

Test 7002, Run 12,
$M_\infty = 6$, $\alpha = 0$ deg

Figure 51. Back-face heating images: angle-of-attack effects, $M_\infty = 6$, $Re_\infty = 3.9 \times 10^6$/ft.

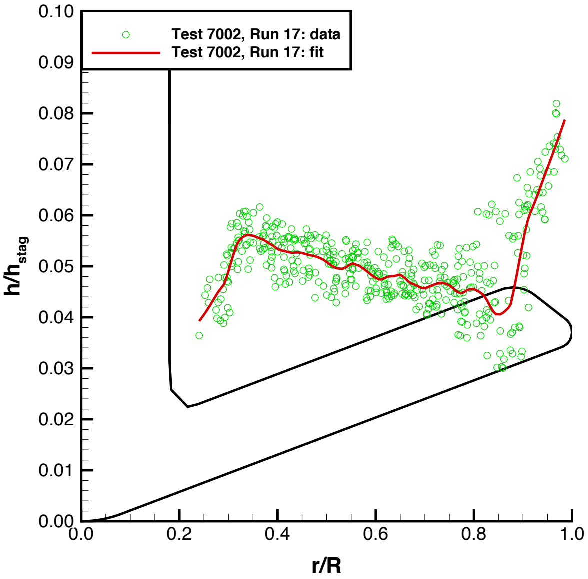

Test 7002, Run 17,
$M_\infty = 6$, $\alpha = -5$ deg

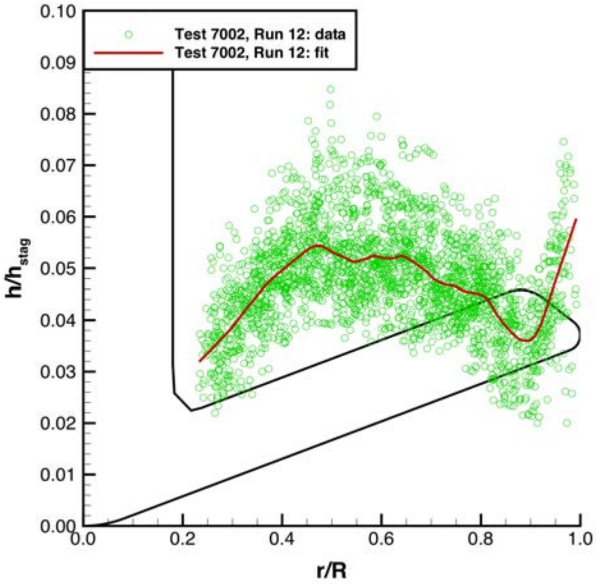

Test 7002, Run 12,
$M_\infty = 6$, $\alpha = 0$ deg

Data from $\phi = -20$ deg to +20 deg rays

Figure 52. Back-face heating data: angle-of-attack effects, $M_\infty = 6$, $Re_\infty = 3.9 \times 10^6$/ft.

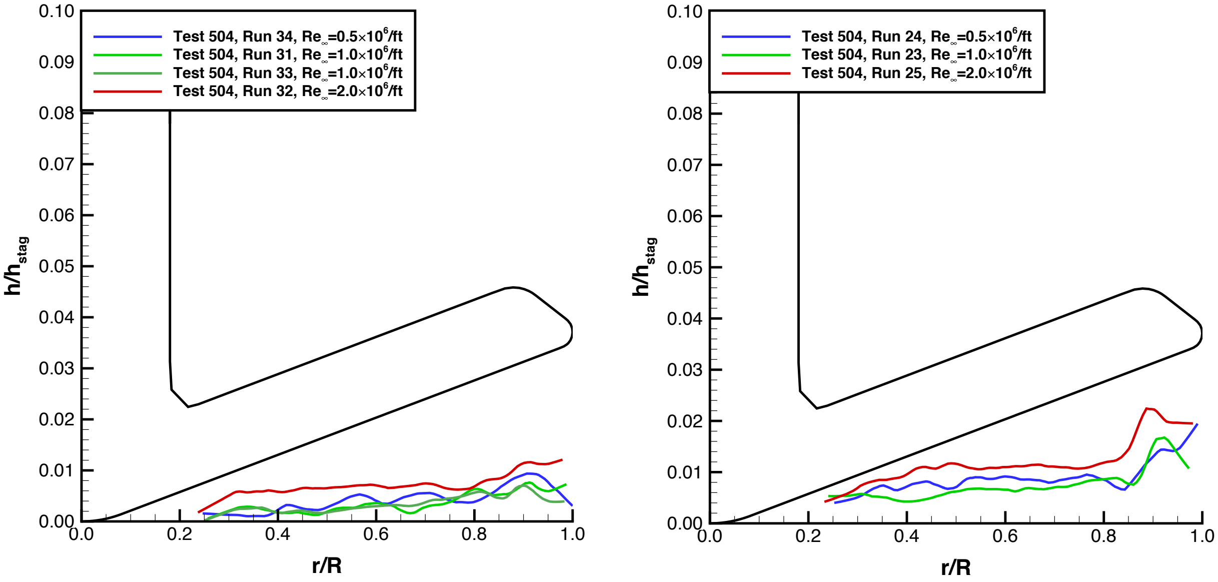

$M_\infty = 10$, $\alpha = -10$ deg

$M_\infty = 10$, $\alpha = -5$ deg

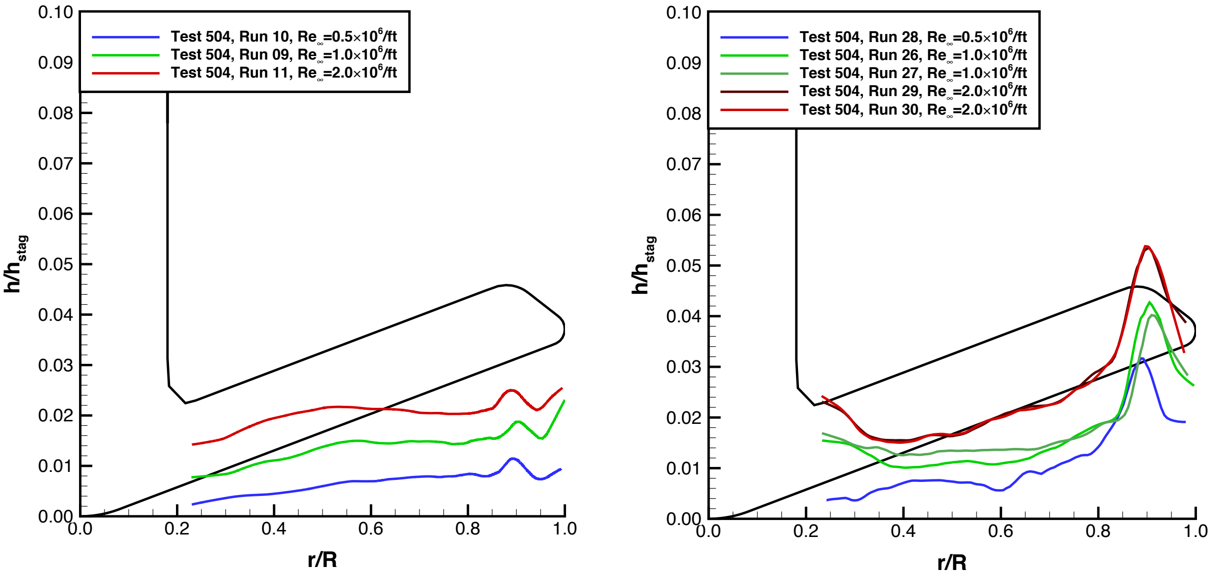

$M_\infty = 10$, $\alpha = 0$ deg

$M_\infty = 10$, $\alpha = +5$ deg

Data from $\phi = -20$ deg to +20 deg rays

Figure 53. Back-face fitted heating data: Reynolds number effects at $M_\infty = 10$.

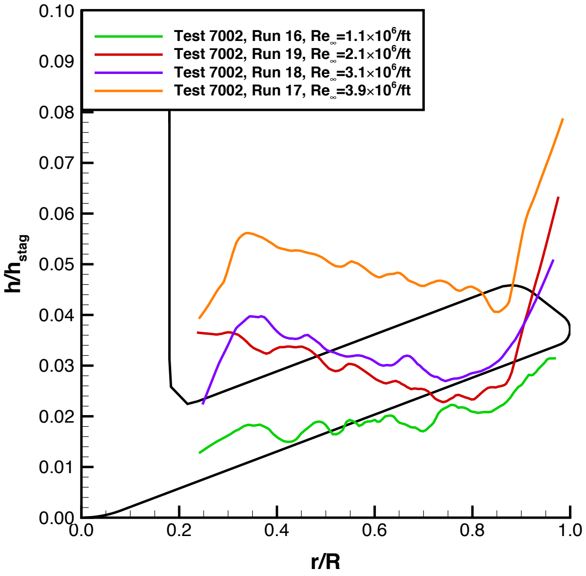

$M_\infty = 6$, $\alpha = -5$ deg

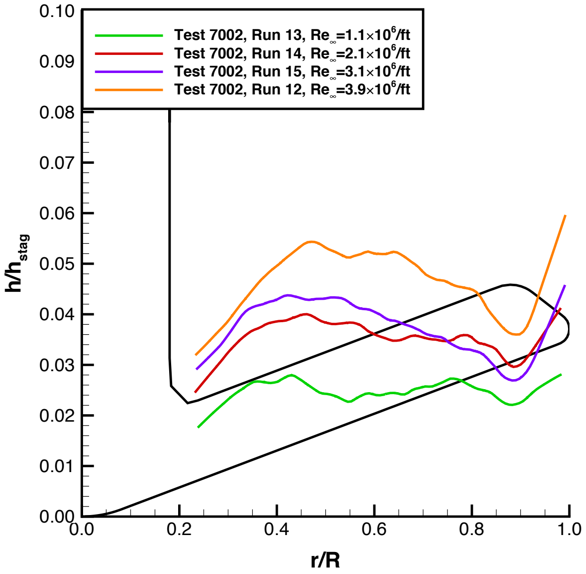

$M_\infty = 6$, $\alpha = 0$ deg

Data from $\phi = -20$ deg to +20 deg rays

Figure 54. Back-face fitted heating data: Reynolds number effects at $M_\infty = 6$.

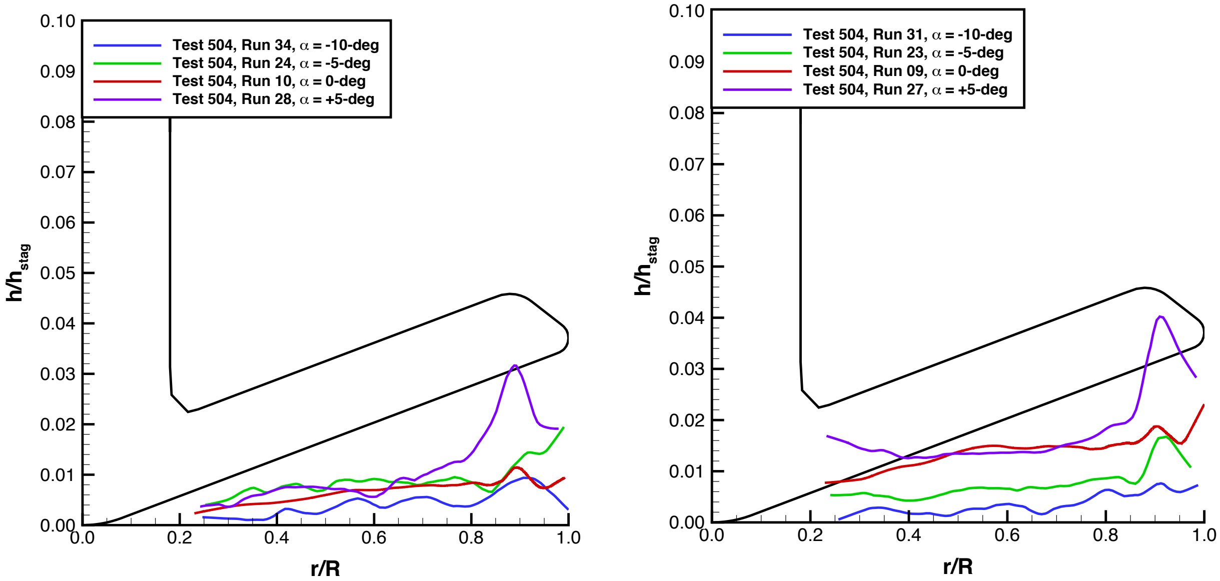

$M_\infty = 10$, $Re_\infty = 0.5\times10^6$/ft

$M_\infty = 10$, $Re_\infty = 1.0\times10^6$/ft

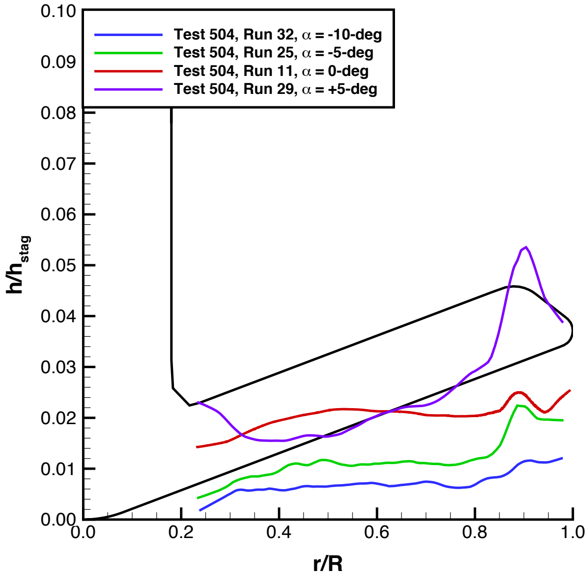

$M_\infty = 10$, $Re_\infty = 2.0\times10^6$/ft

Data from $\phi = -20$ deg to +20 deg rays

Figure 55. Back-face fitted heating data: angle-of-attack effects at $M_\infty = 10$.

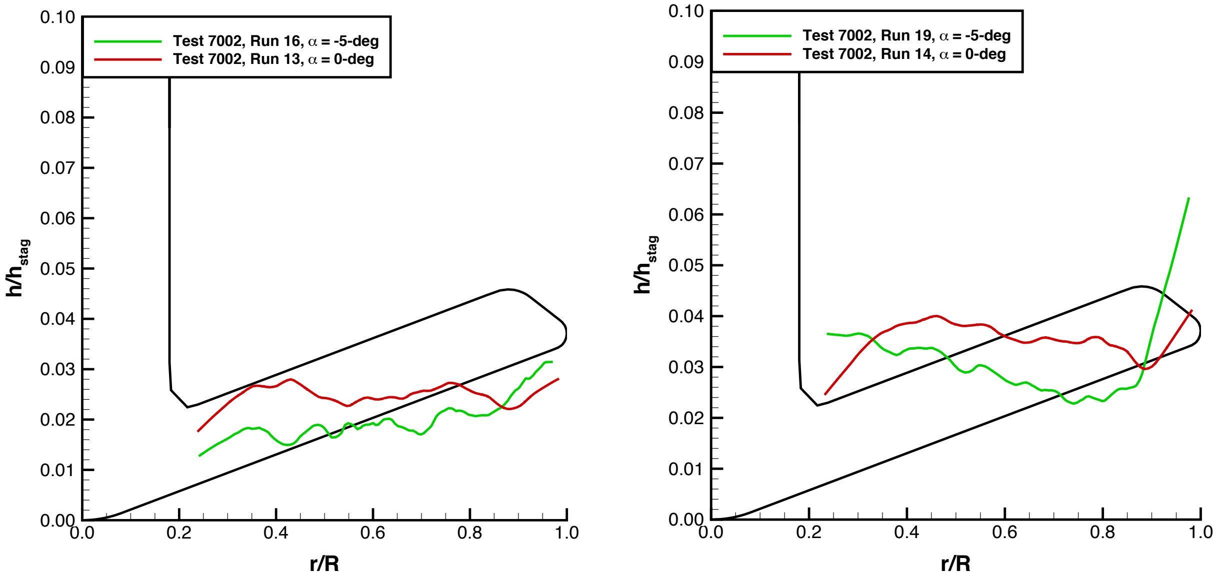

$M_\infty = 6$, $Re_\infty = 1.1\times10^6$/ft $M_\infty = 6$, $Re_\infty = 2.1\times10^6$/ft

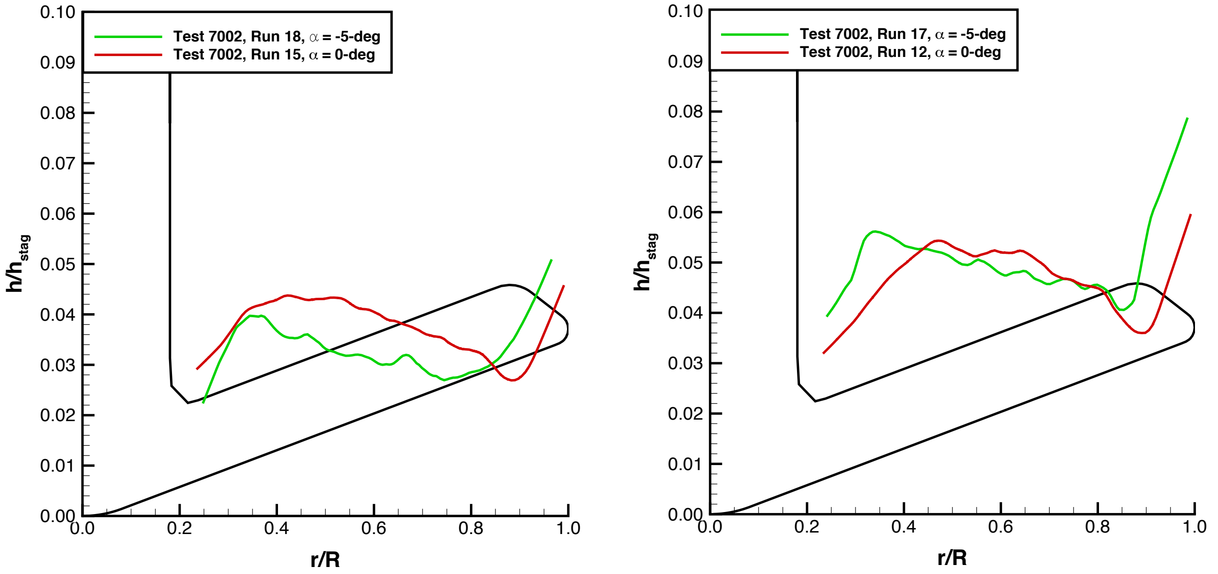

$M_\infty = 6$, $Re_\infty = 3.1\times10^6$/ft $M_\infty = 6$, $Re_\infty = 3.9\times10^6$/ft

Data from ϕ = –20 deg to +20 deg rays

Figure 56. Back-face fitted heating data: angle-of-attack effects at $M_\infty = 6$.

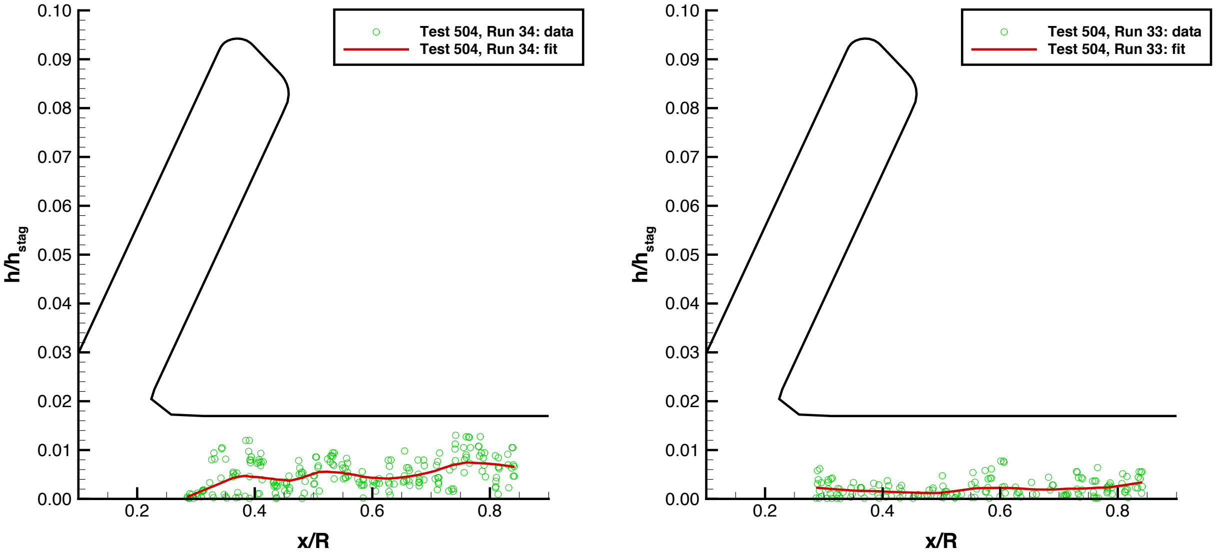

Test 504, Run 34,
$M_\infty = 10$, $Re_\infty = 0.5\times10^6$/ft

Test 504, Run 33,
$M_\infty = 10$, $Re_\infty = 1.0\times10^6$/ft

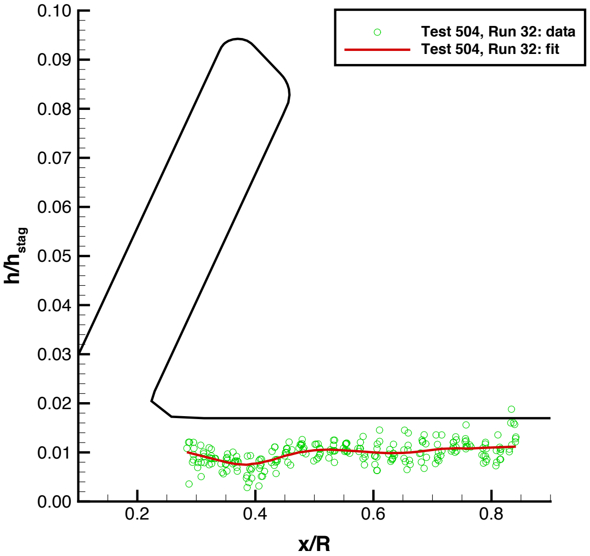

Test 504, Run 32,
$M_\infty = 10$, $Re_\infty = 2.0\times10^6$/ft

Data from leeward side centerline

Figure 57. Payload heating data, Reynolds number effects: $M_\infty = 10$, $\alpha = -10$ deg.

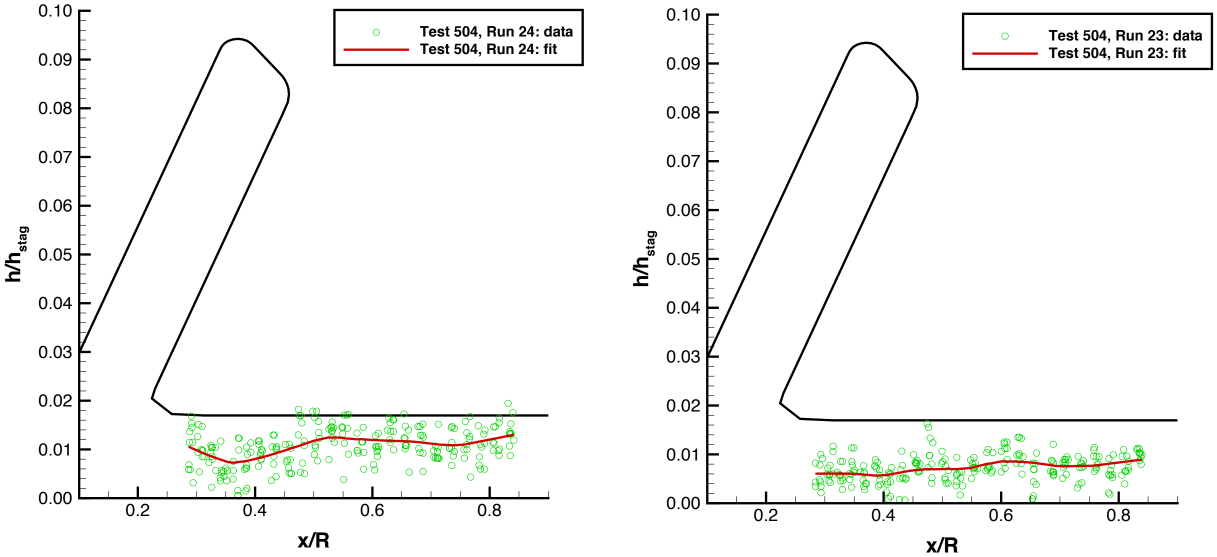

Test 504, Run 24,
$M_\infty = 10$, $Re_\infty = 0.5\times10^6$/ft

Test 504, Run 23,
$M_\infty = 10$, $Re_\infty = 1.0\times10^6$/ft

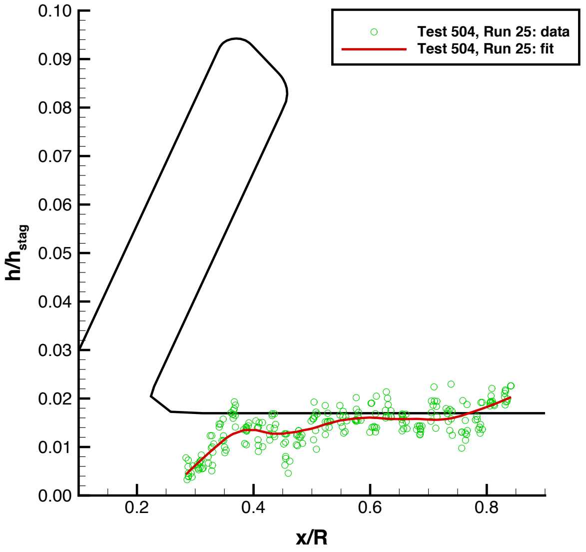

Test 504, Run 25,
$M_\infty = 10$, $Re_\infty = 2.0\times10^6$/ft

Data from leeward side centerline

Figure 58. Payload heating data, Reynolds number effects: $M_\infty = 10$, $\alpha = -5$ deg.

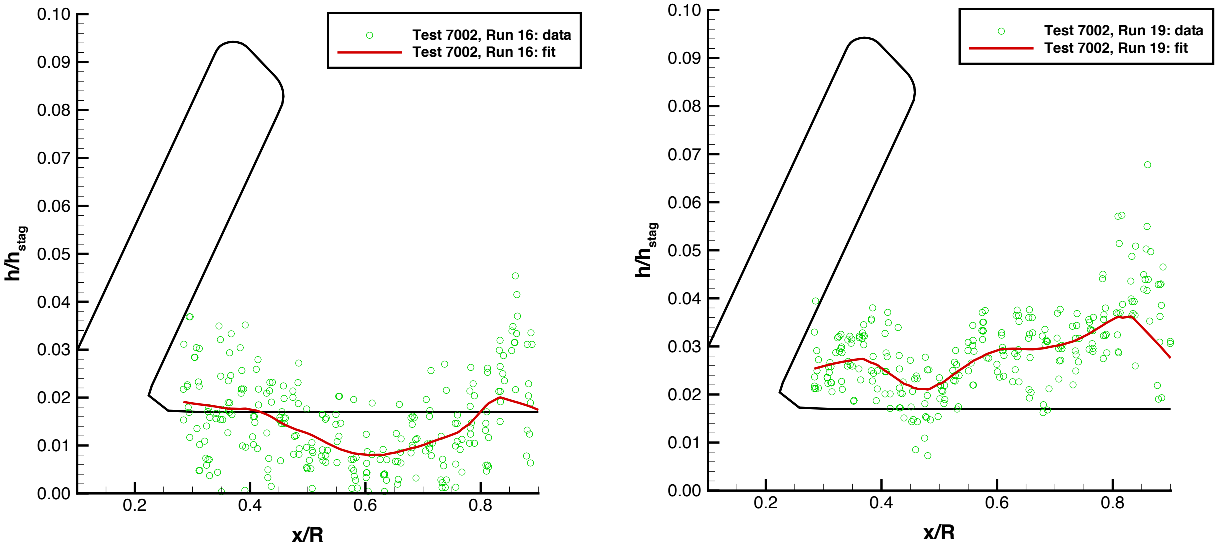

Test 7002, Run 16,
$M_\infty = 6$, $Re_\infty = 1.1\times10^6$/ft

Test 7002, Run 19,
$M_\infty = 6$, $Re_\infty = 2.1\times10^6$/ft

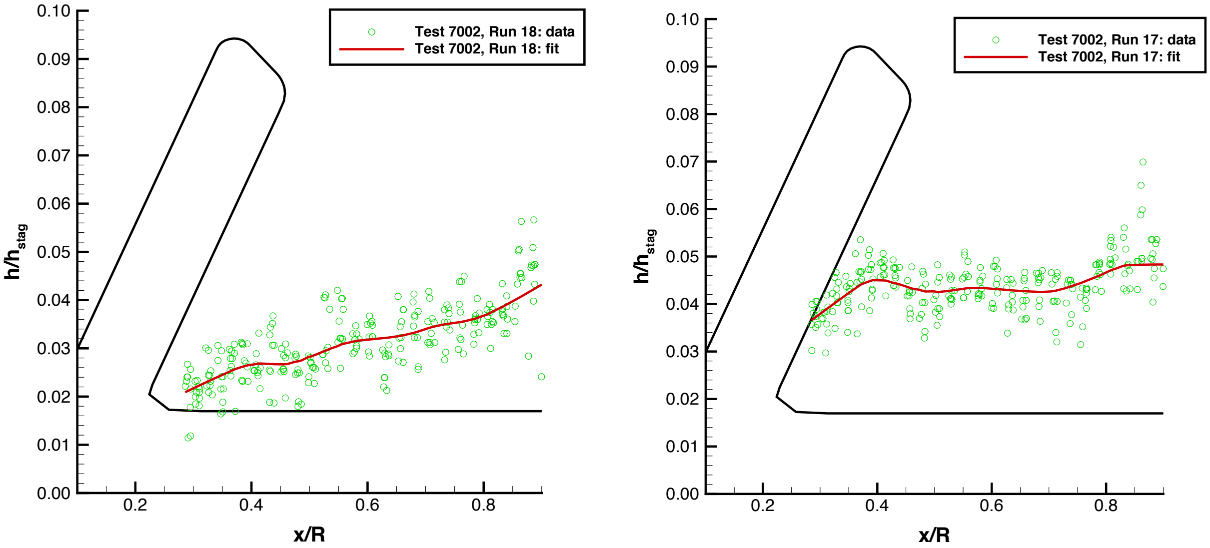

Test 7002, Run 18,
$M_\infty = 6$, $Re_\infty = 3.1\times10^6$/ft

Test 7002, Run 17,
$M_\infty = 6$, $Re_\infty = 3.9\times10^6$/ft

Data from leeward side centerline

Figure 59. Payload heating data, Reynolds number effects: $M_\infty = 6$, $\alpha = -5$ deg.

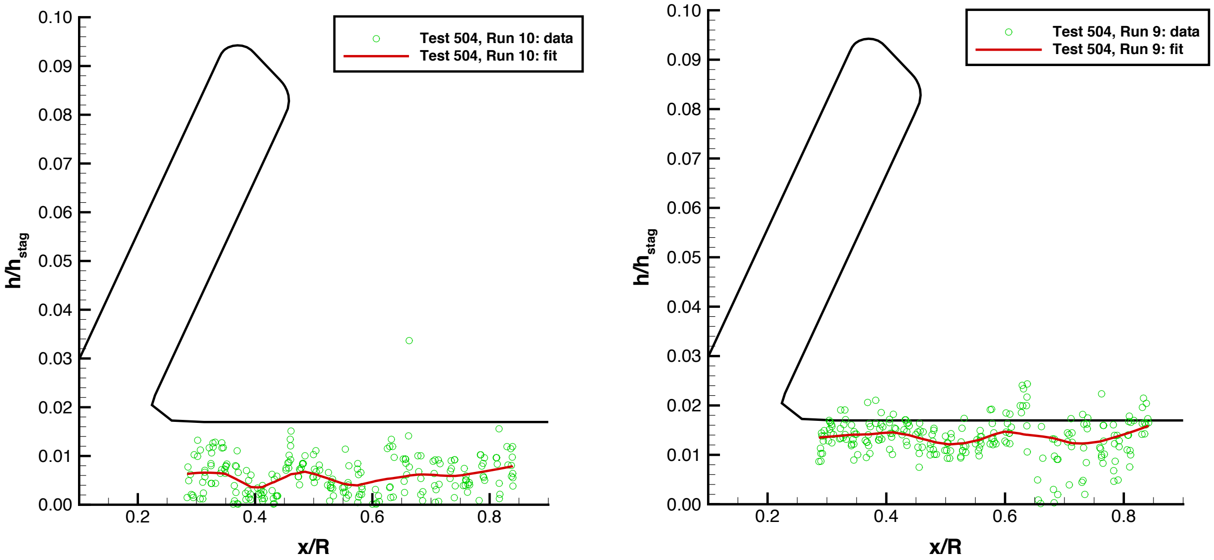

Test 504, Run 10,
$M_\infty = 10$, $Re_\infty = 0.5\times10^6$/ft

Test 504, Run 9,
$M_\infty = 10$, $Re_\infty = 1.0\times10^6$/ft

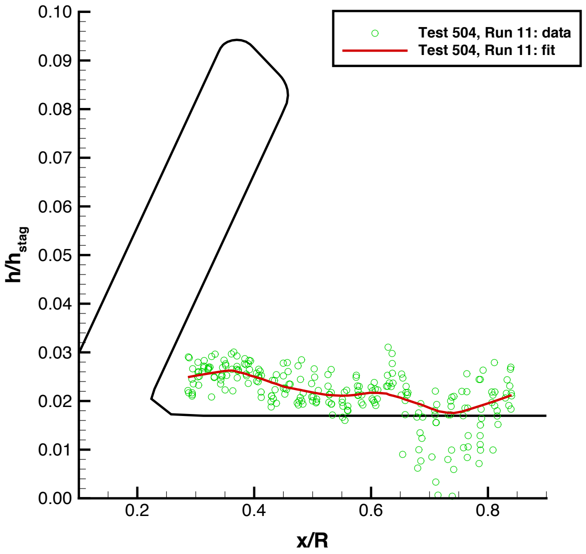

Test 504, Run 11,
$M_\infty = 10$, $Re_\infty = 2.0\times10^6$/ft

Data from leeward side centerline

Figure 60. Payload heating data, Reynolds number effects: $M_\infty = 10$, α = 0 deg.

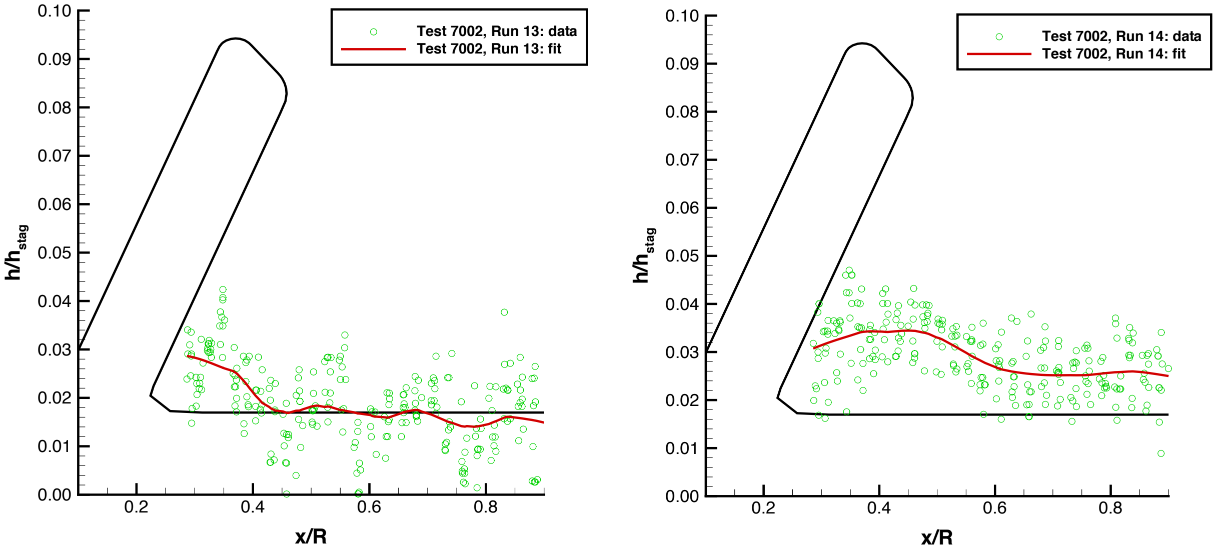

Test 7002, Run 13,
$M_\infty = 6$, $Re_\infty = 1.1\times10^6$/ft

Test 7002, Run 14,
$M_\infty = 6$, $Re_\infty = 2.1\times10^6$/ft

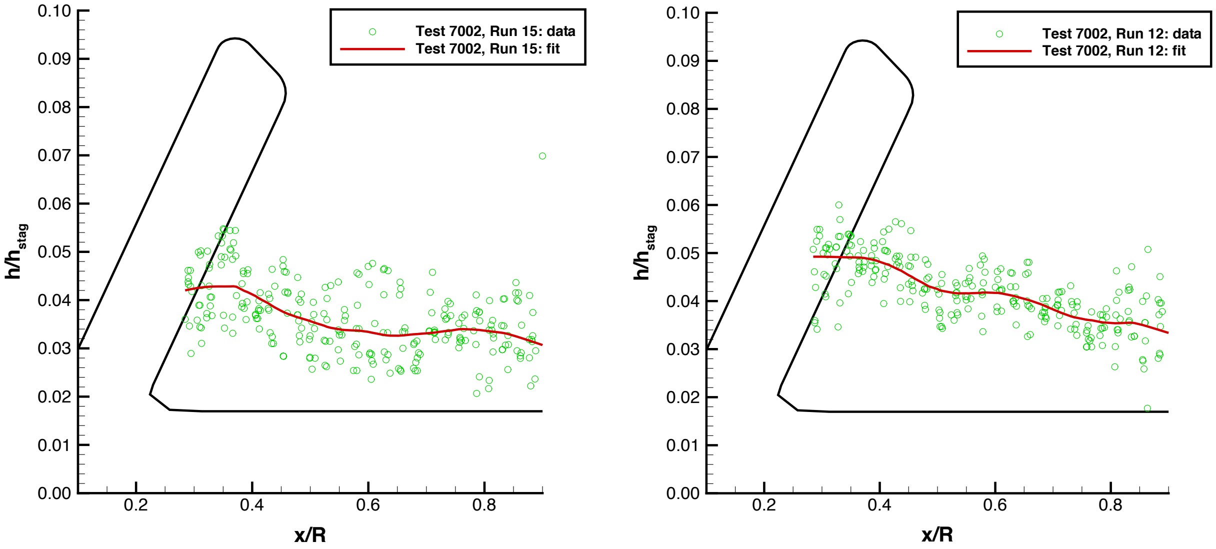

Test 7002, Run 15,
$M_\infty = 6$, $Re_\infty = 3.1\times10^6$/ft

Test 7002, Run 12,
$M_\infty = 6$, $Re_\infty = 3.9\times10^6$/ft

Data from leeward side centerline

Figure 61. Payload heating data, Reynolds number effects: $M_\infty = 6$, α = 0 deg.

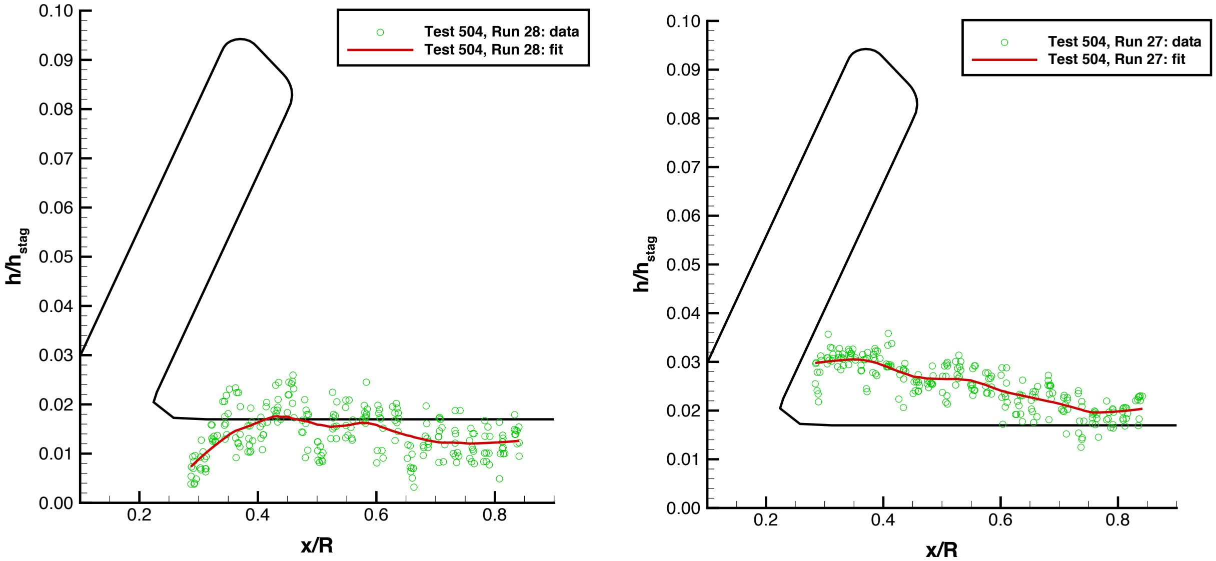

Test 504, Run 28,
$M_\infty = 10$, $Re_\infty = 0.5\times10^6$/ft

Test 504, Run 27,
$M_\infty = 10$, $Re_\infty = 1.0\times10^6$/ft

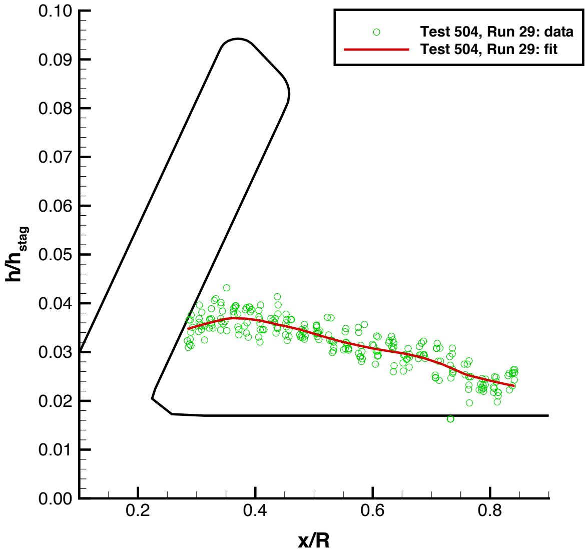

Test 504, Run 29,
$M_\infty = 10$, $Re_\infty = 2.0\times10^6$/ft

Data from leeward side centerline

Figure 62. Payload heating data, Reynolds number effects: $M_\infty = 10$, $\alpha = +5$ deg.

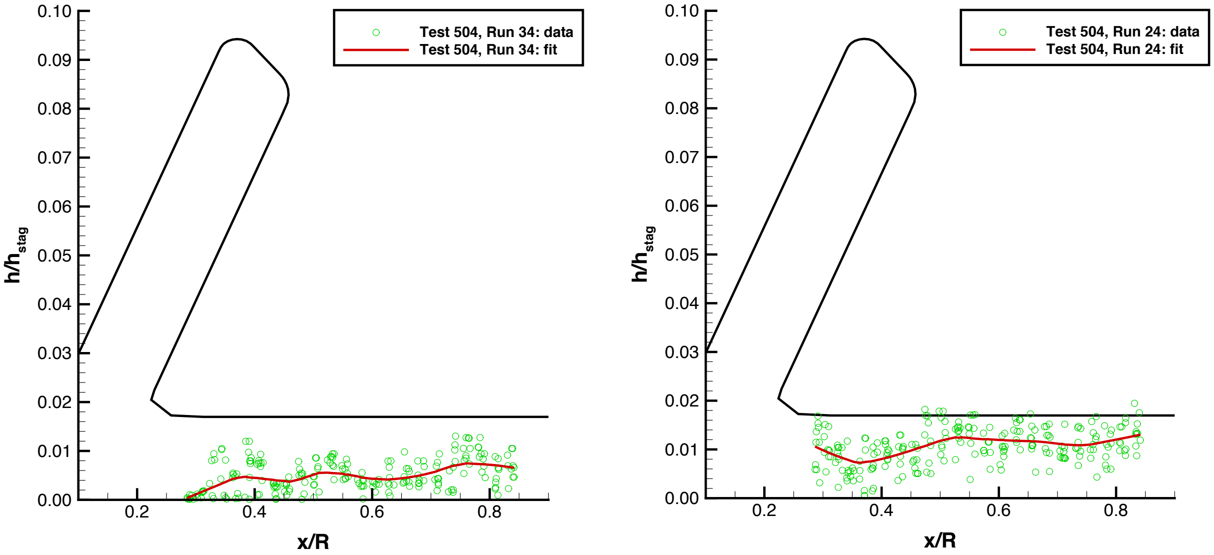

Test 504, Run 34,
$M_\infty = 10$, $\alpha = -10$ deg

Test 504, Run 24,
$M_\infty = 10$, $\alpha = -5$ deg

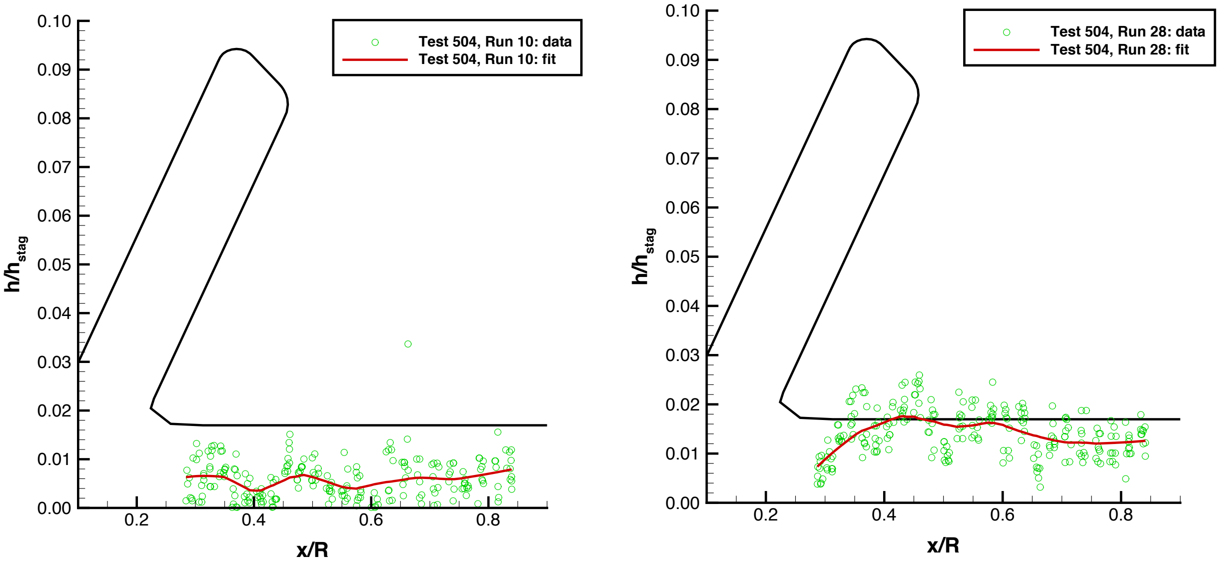

Test 504, Run 10,
$M_\infty = 10$, $\alpha = 0$ deg

Test 504, Run 28,
$M_\infty = 10$, $\alpha = +5$ deg

Data from leeward side centerline

Figure 63. Payload heating data, angle-of-attack effects: $M_\infty = 10$, $Re_\infty = 0.5\times10^6$/ft.

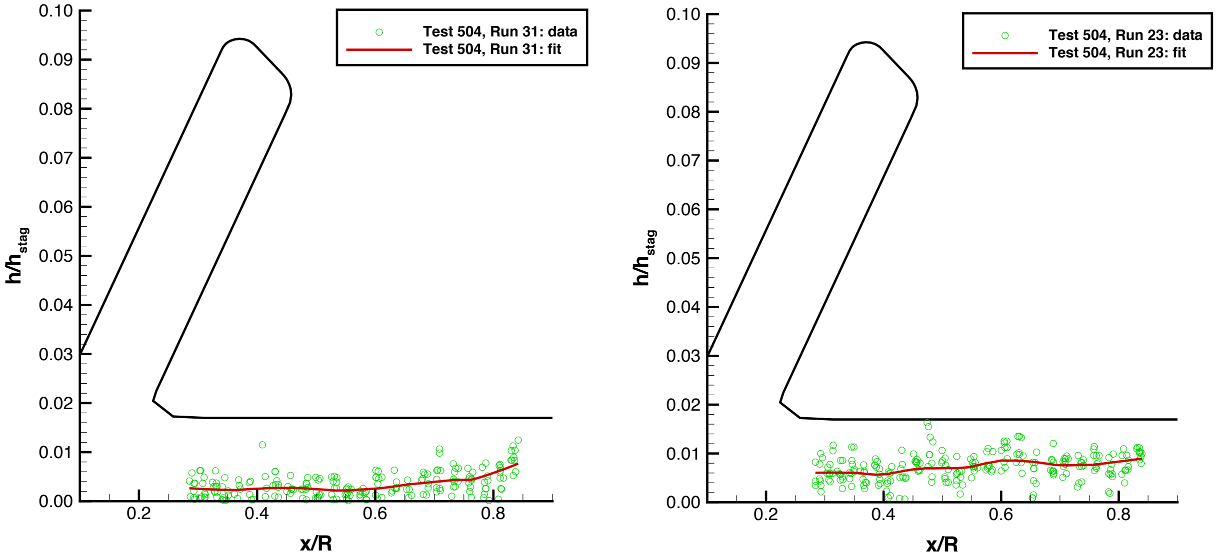

Test 504, Run 31,
$M_\infty = 10$, $\alpha = -10$ deg

Test 504, Run 23,
$M_\infty = 10$, $\alpha = -5$ deg

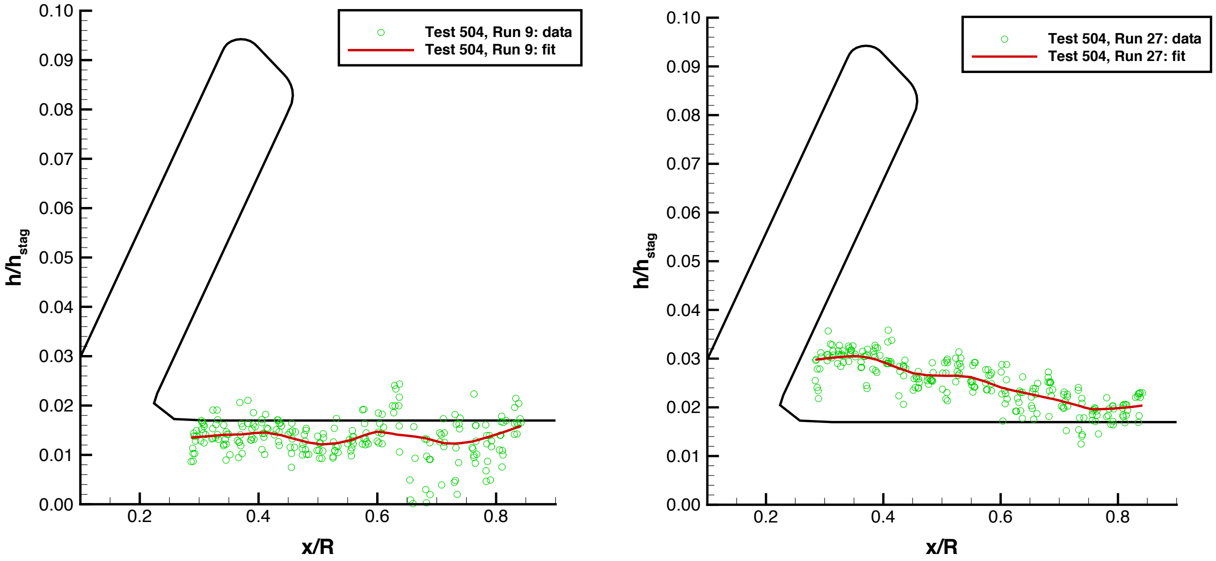

Test 504, Run 9,
$M_\infty = 10$, $\alpha = 0$ deg

Test 504, Run 27,
$M_\infty = 10$, $\alpha = +5$ deg

Data from leeward side centerline

Figure 64. Payload heating data, angle-of-attack effects: $M_\infty = 10$, $Re_\infty = 1.0 \times 10^6$/ft.

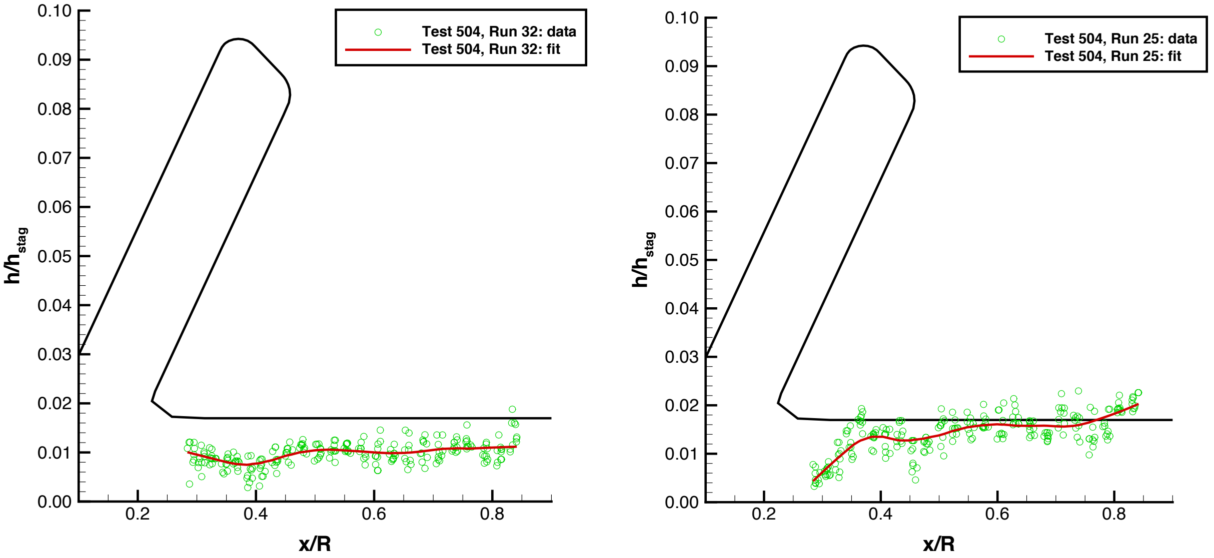

Test 504, Run 32,
$M_\infty = 10$, $\alpha = -10$ deg

Test 504, Run 25,
$M_\infty = 10$, $\alpha = -5$ deg

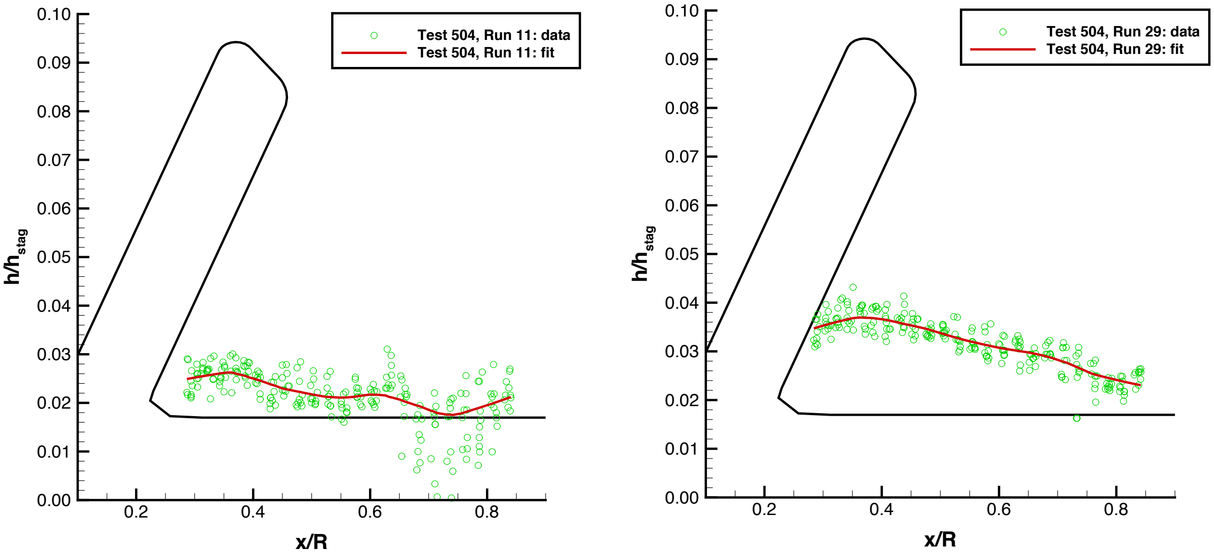

Test 504, Run 11,
$M_\infty = 10$, $\alpha = 0$ deg

Test 504, Run 29,
$M_\infty = 10$, $\alpha = +5$ deg

Data from leeward side centerline

Figure 65. Payload heating data, angle-of-attack effects: $M_\infty = 10$, $Re_\infty = 2.0 \times 10^6$/ft.

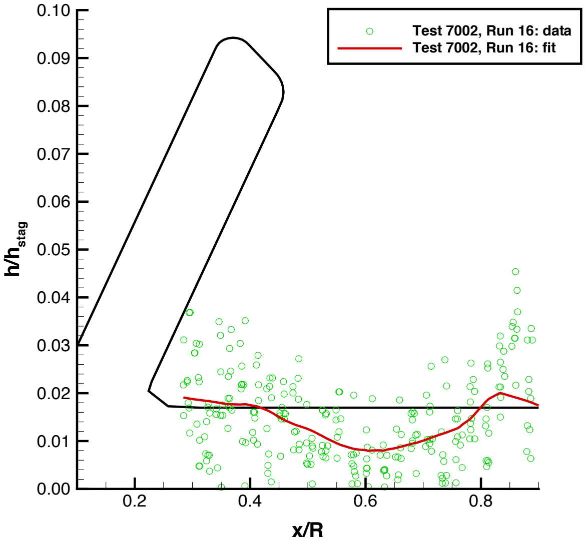

Test 7002, Run 16,
M$_\infty$ = 6, α = –5 deg

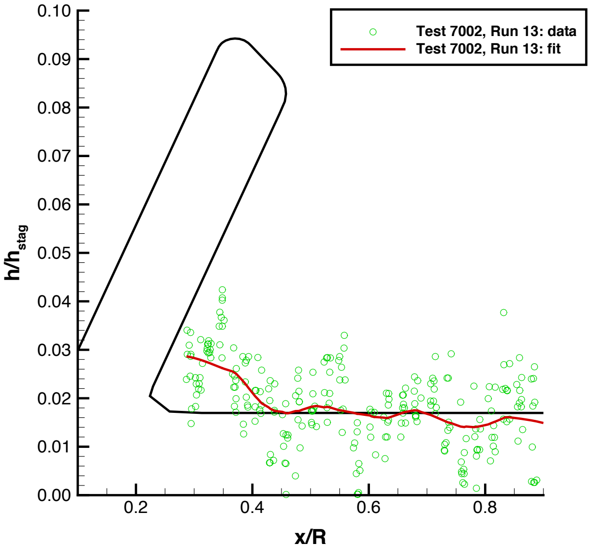

Test 7002, Run 13,
M$_\infty$ = 6, α = 0 deg

Data from leeward side centerline

Figure 66. Payload heating data, angle-of-attack effects: M$_\infty$ = 6, Re$_\infty$ = 1.1×10^6/ft.

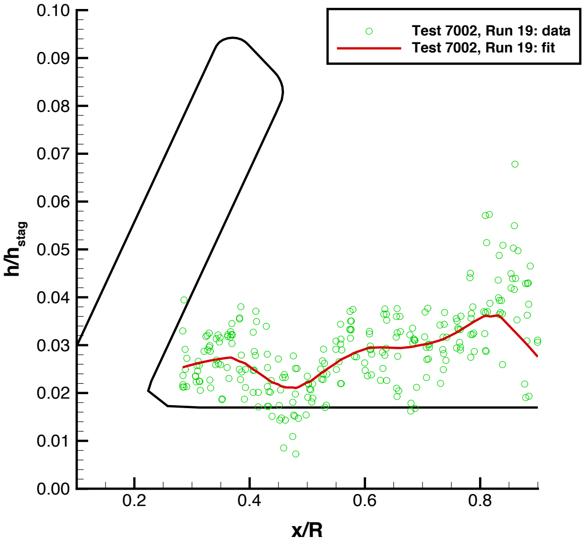

Test 7002, Run 19,
M$_\infty$ = 6, α = –5 deg

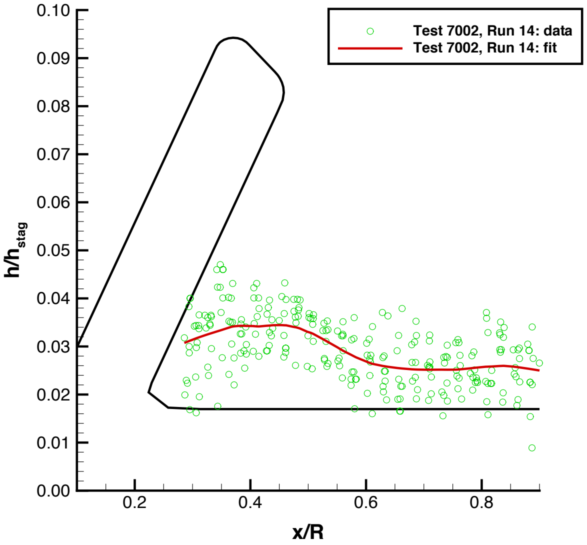

Test 7002, Run 14,
M$_\infty$ = 6, α = 0 deg

Data from leeward side centerline

Figure 67. Payload heating data, angle-of-attack effects: M$_\infty$ = 6, Re$_\infty$ = 2.1×10^6/ft.

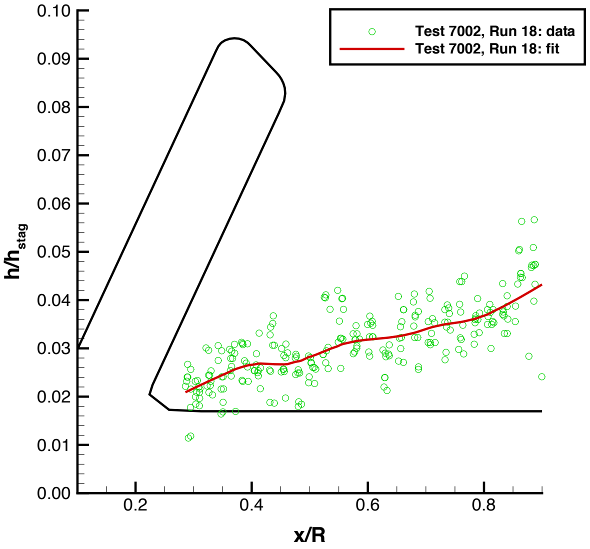

Test 7002, Run 18,
$M_\infty = 6$, $\alpha = -5$ deg

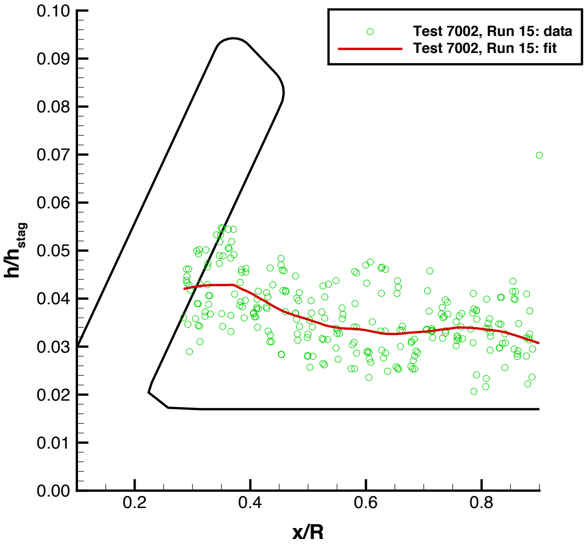

Test 7002, Run 15,
$M_\infty = 6$, $\alpha = 0$ deg

Data from leeward side centerline

Figure 68. Payload heating data, angle-of-attack effects: $M_\infty = 6$, $Re_\infty = 3.1\times10^6$/ft.

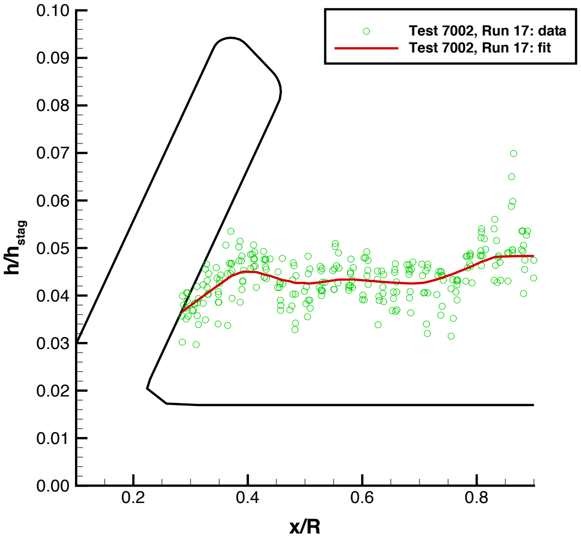

Test 7002, Run 17,
$M_\infty = 6$, $\alpha = -5$ deg

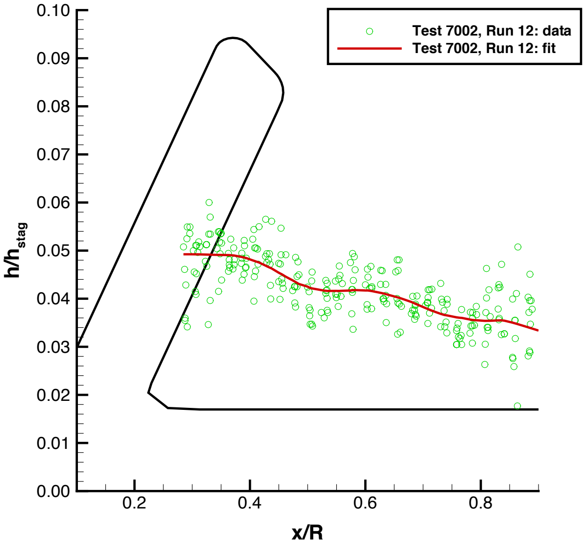

Test 7002, Run 12,
$M_\infty = 6$, $\alpha = 0$ deg

Data from leeward side centerline

Figure 69. Payload heating data, angle-of-attack effects: $M_\infty = 6$, $Re_\infty = 3.9\times10^6$/ft.

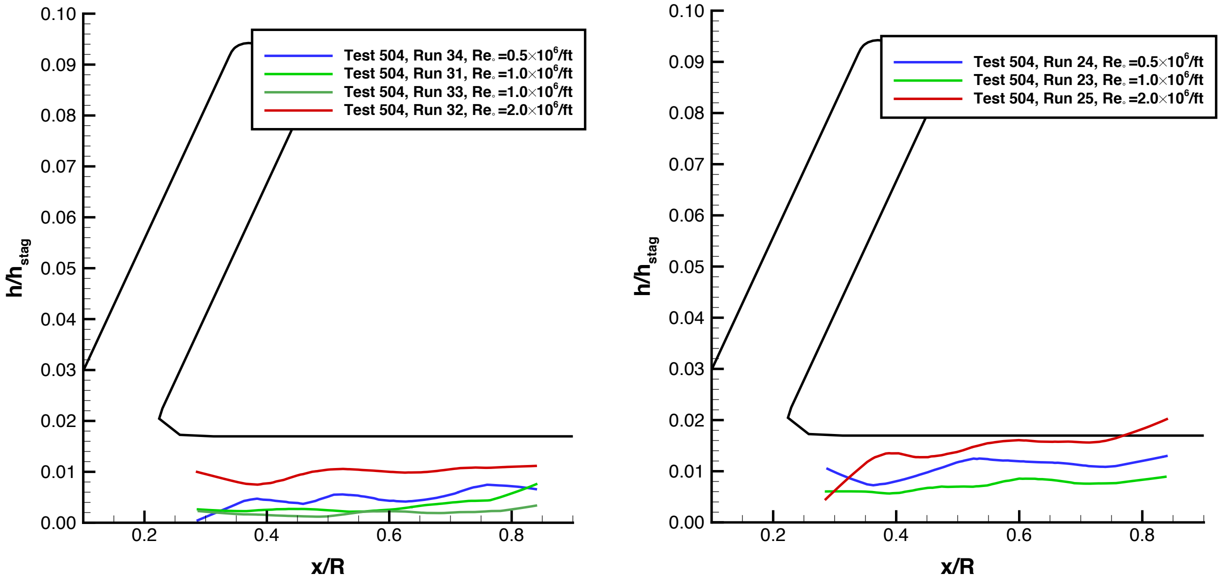

$M_\infty = 10$, $\alpha = -10$ deg

$M_\infty = 10$, $\alpha = -5$ deg

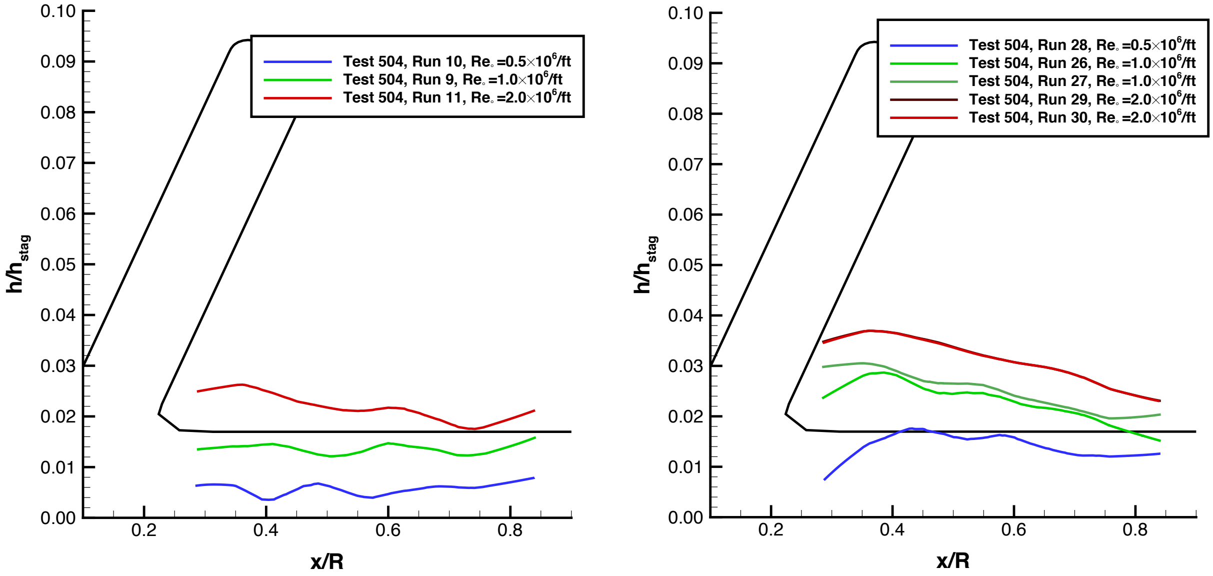

$M_\infty = 10$, $\alpha = 0$ deg

$M_\infty = 10$, $\alpha = +5$ deg

Data from leeward side centerline

Figure 70. Payload fitted heating data: Reynolds number effects at $M_\infty = 10$.

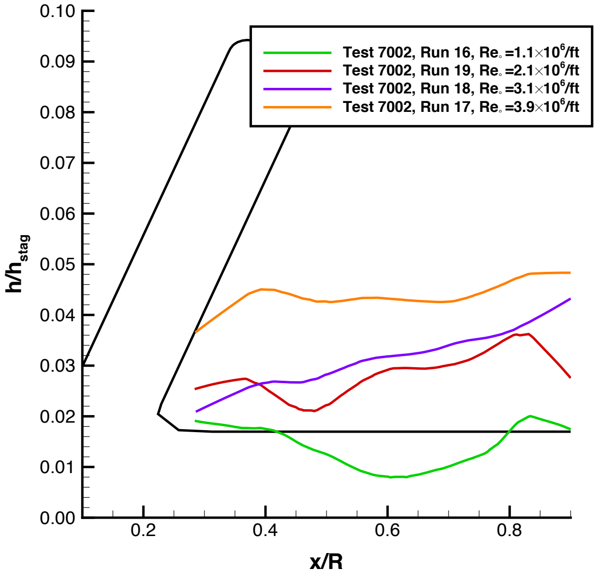

$M_\infty = 6$, $\alpha = -5$ deg

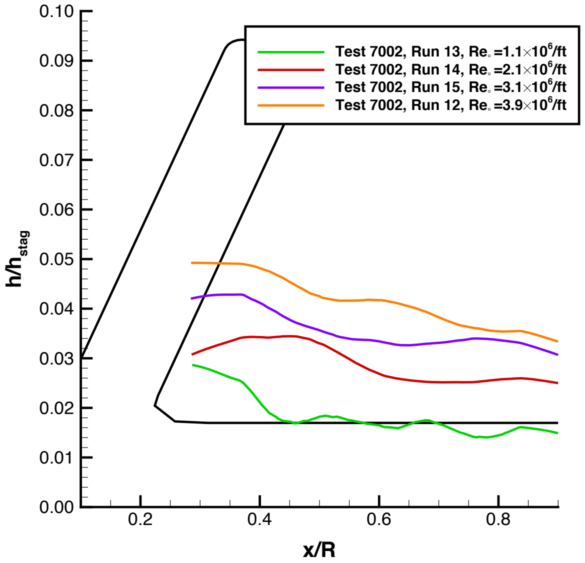

$M_\infty = 6$, $\alpha = 0$ deg

Data from leeward side centerline

Figure 71. Payload fitted heating data: Reynolds number effects at $M_\infty = 6$.

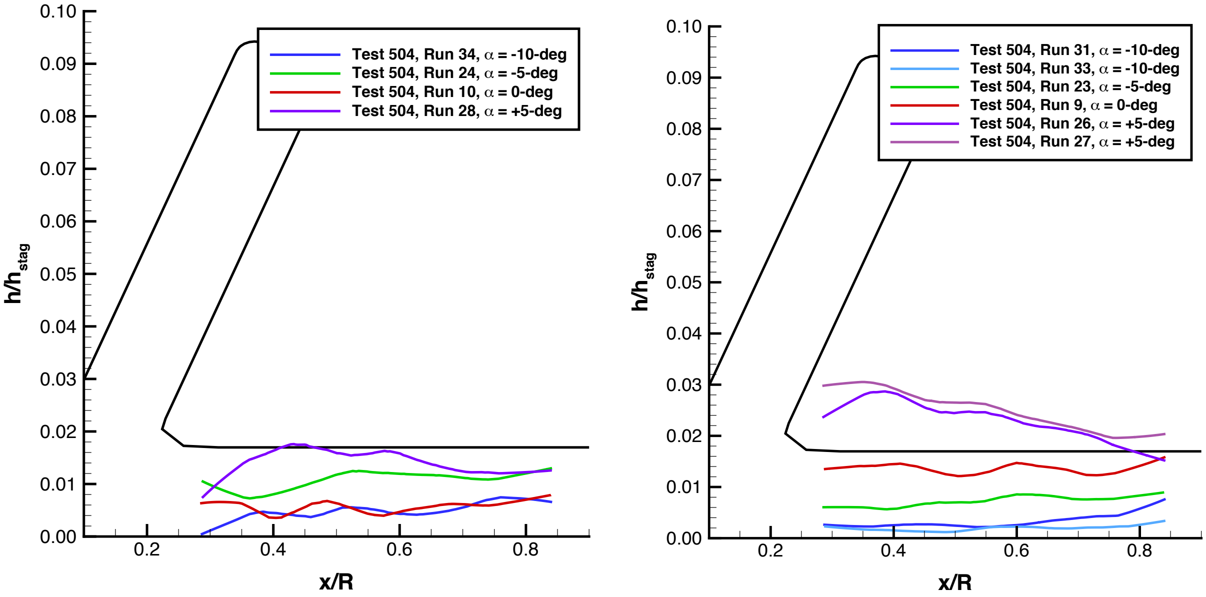

$M_\infty = 10$, $Re_\infty = 0.5\times10^6$/ft

$M_\infty = 10$, $Re_\infty = 1.0\times10^6$/ft

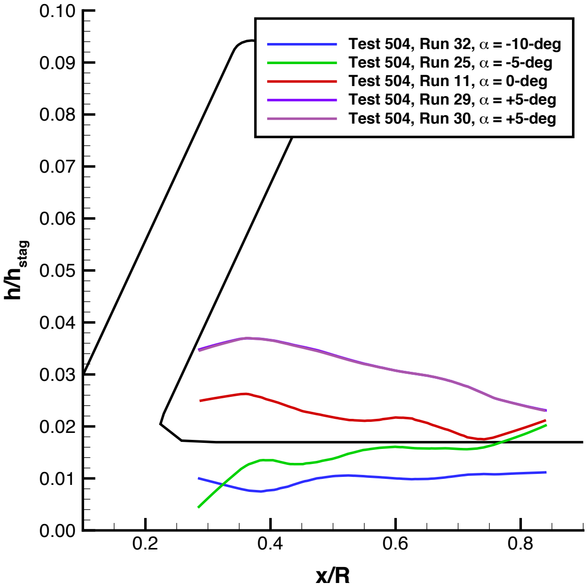

$M_\infty = 10$, $Re_\infty = 2.0\times10^6$/ft

Data from leeward side centerline

Figure 72. Payload fitted heating data: angle-of-attack effects at $M_\infty = 10$.

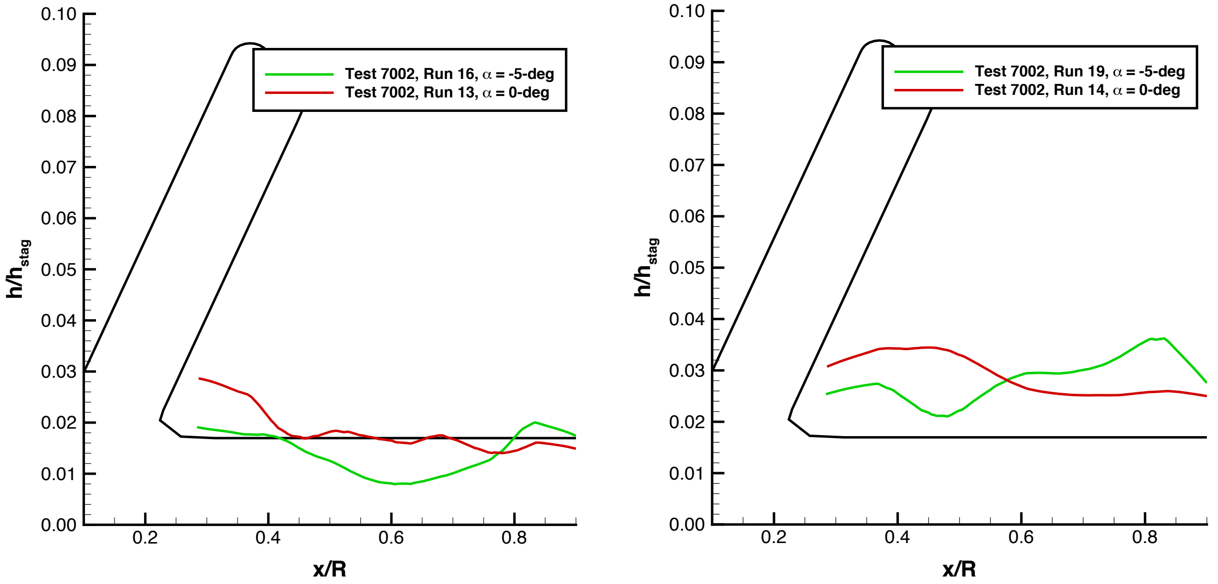

M$_\infty$ = 6, Re$_\infty$ = 1.1×10^6/ft

M$_\infty$ = 6, Re$_\infty$ = 2.1×10^6/ft

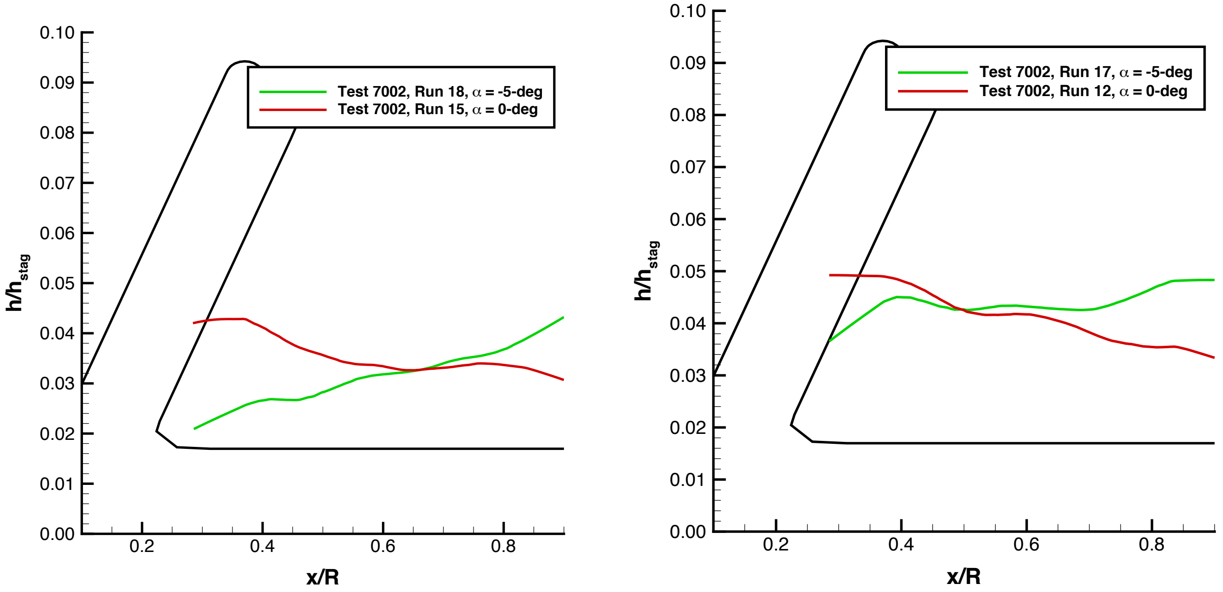

M$_\infty$ = 6, Re$_\infty$ = 3.1×10^6/ft

M$_\infty$ = 6, Re$_\infty$ = 3.9×10^6/ft

Data from leeward side centerline

Figure 73. Payload fitted heating data: angle-of-attack effects at M$_\infty$ = 6.

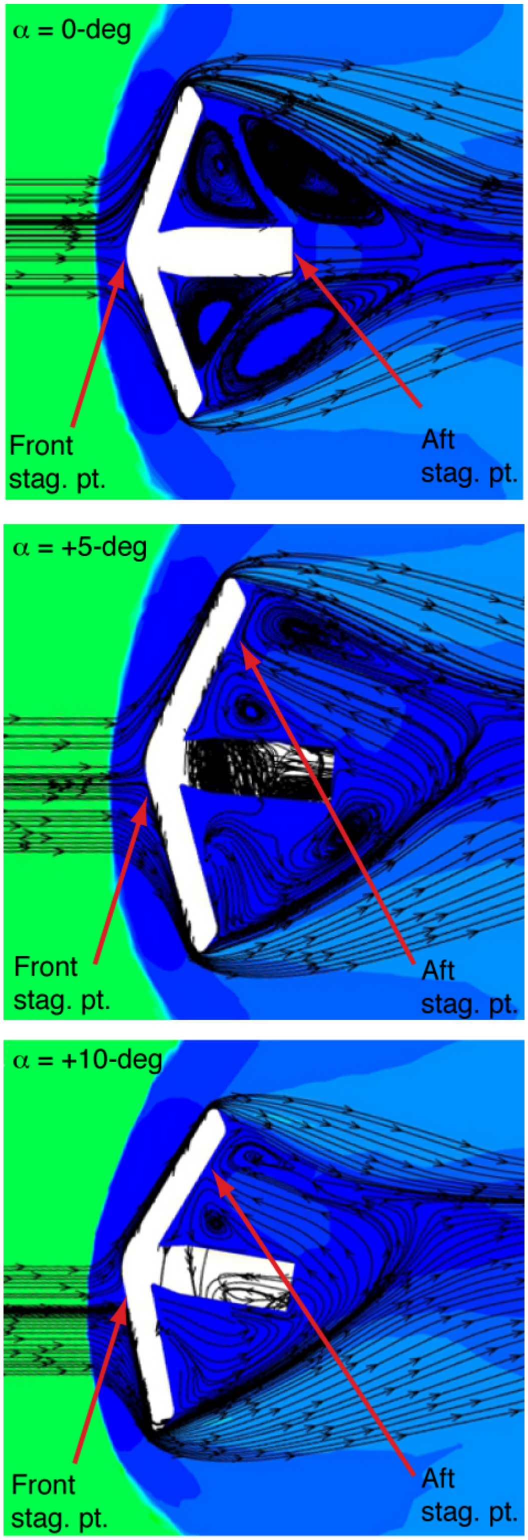

Figure 74. CFD predictions for flight-like vehicle wake structure.

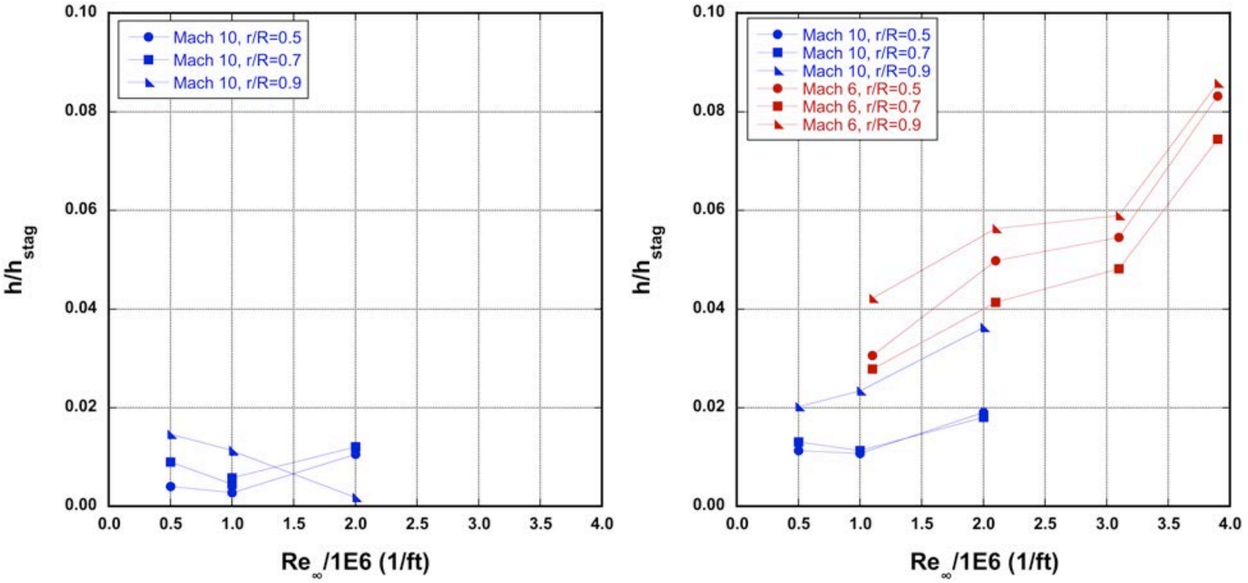

α = –10 deg α = –5 deg

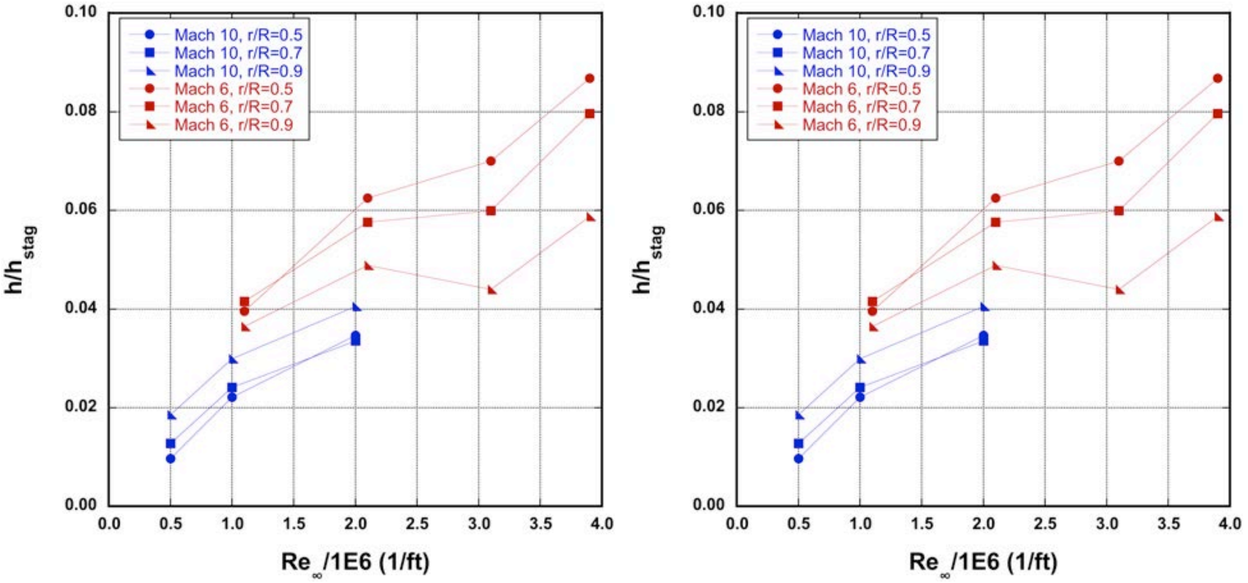

α = 0 deg α = +5 deg

Data averaged from φ = –20 deg to +20 deg rays

Figure 75. Back-face heating trends vs. Reynolds number at Mach 6 and 10.

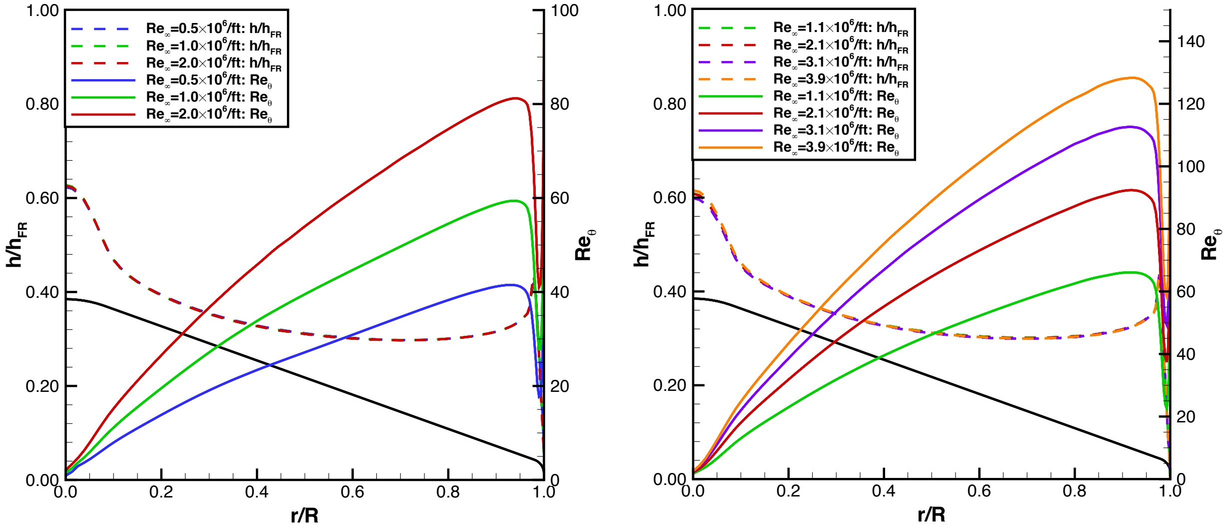

Mach 10 conditions

Mach 6 conditions

Figure 76. Front-face Re_θ distributions for $M_\infty = 10$ and $M_\infty = 6$ at $\alpha = 0$ deg.

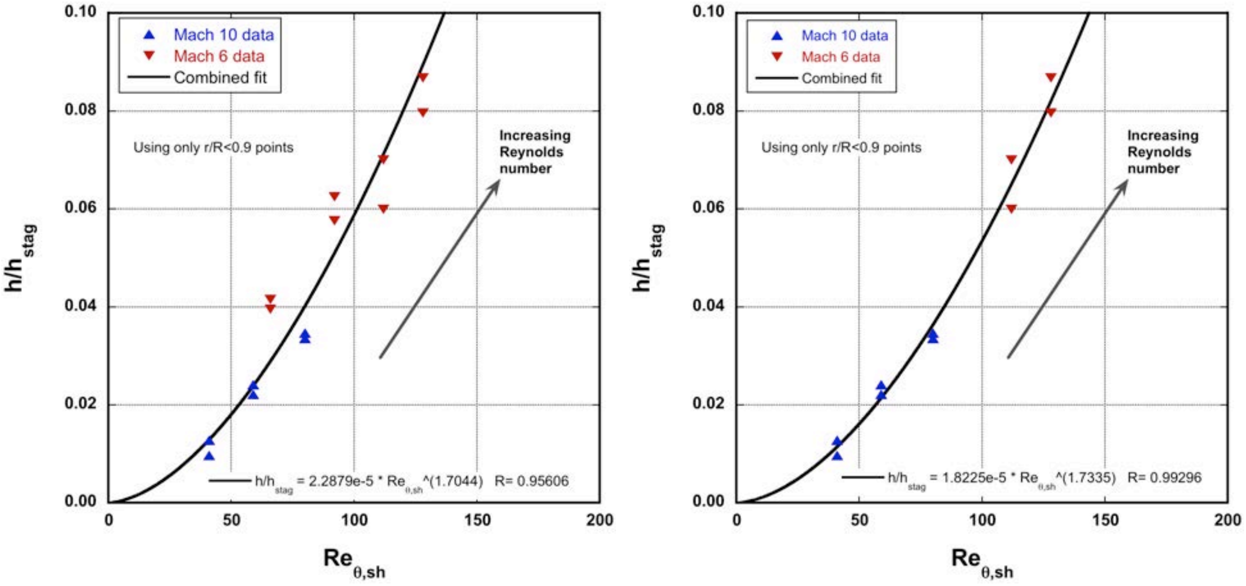

All data points without low Reynolds number Mach 6 data points

Data averaged from ϕ = –20 deg to +20 deg rays

Figure 77. Aeroshell back-face heating trends vs. $Re_{\theta,sh}$ at α = 0 deg.

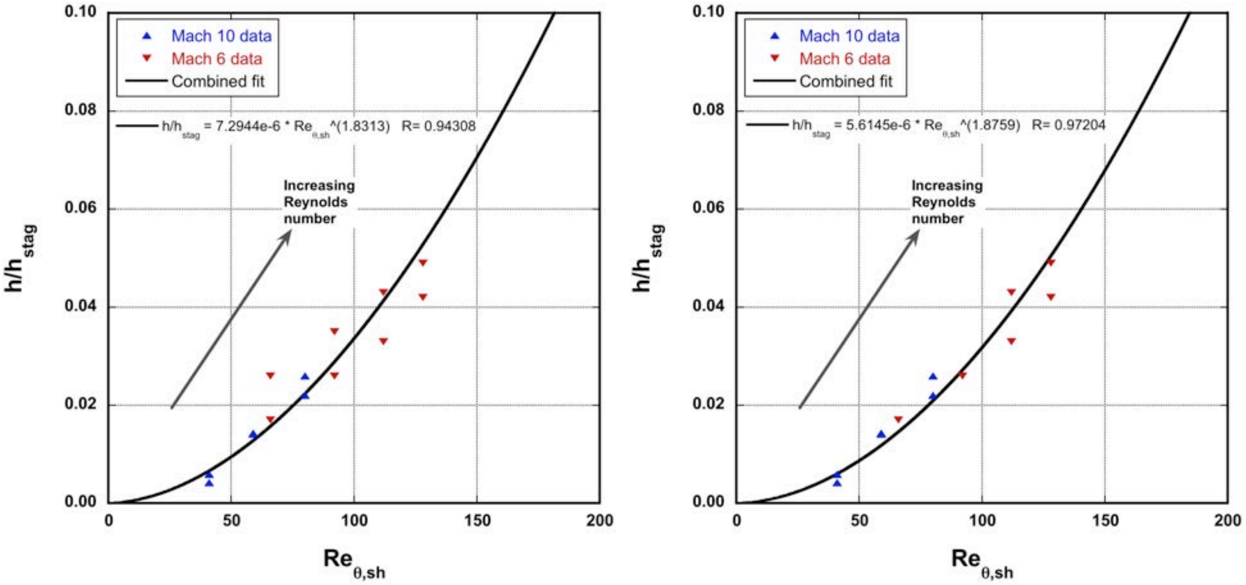

All data points without low Reynolds number Mach 6 data points

Data from leeward side centerline

Figure 78. Payload heating trends vs. $Re_{\theta,sh}$ at α = 0 deg.

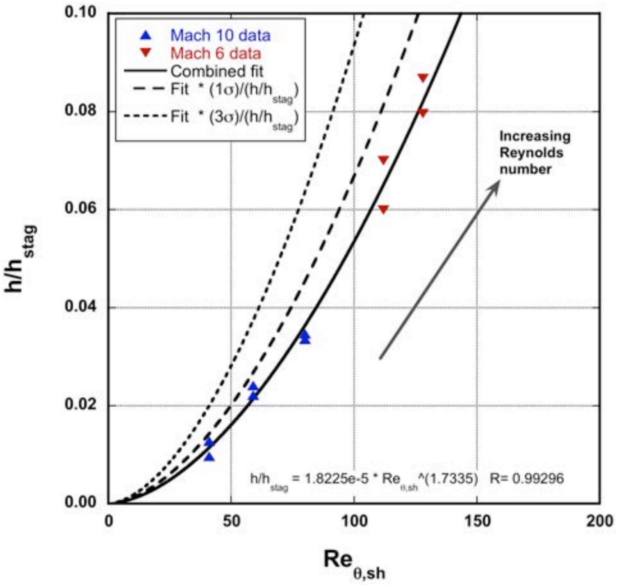

Figure 79. Aeroshell back-face heating vs. $Re_{\theta,sh}$ with uncertainty at α = 0 deg.

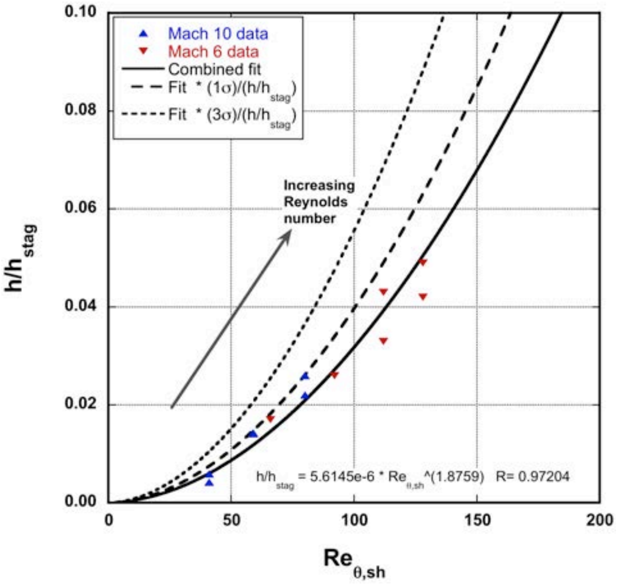

Figure 80. Payload heating vs. $Re_{\theta,sh}$ with uncertainty at α = 0 deg.

Appendix A. Mach 10 Global Heating Images

Global heating images from Test 504 in the 31-Inch Mach 10 Air Tunnel are presented in this appendix in Figure 81 through Figure 98.

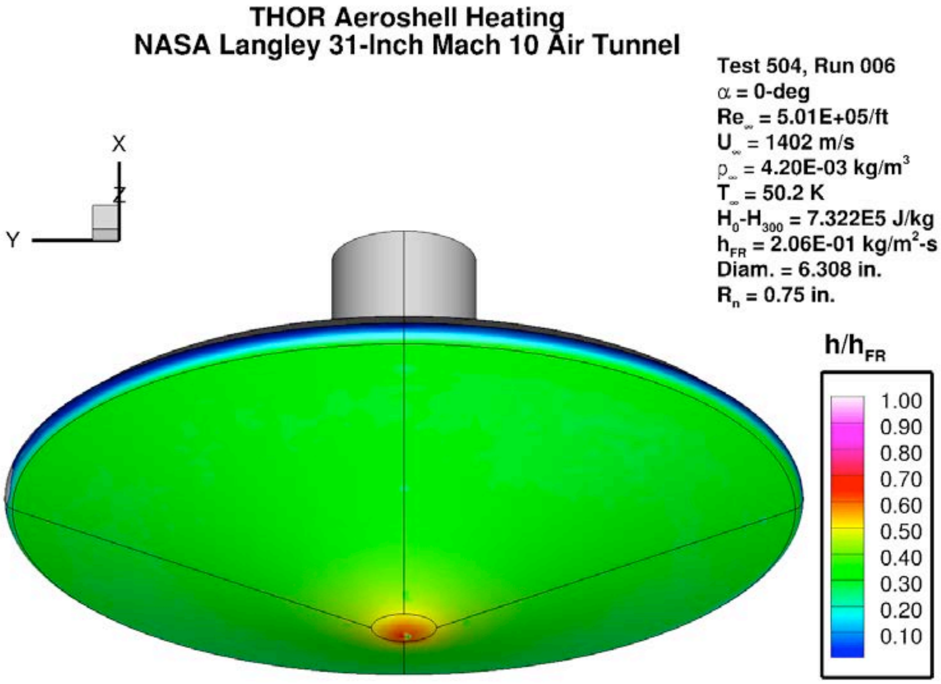

Figure 81. Test 504, Run 06 heating data: $M_\infty = 10$, $\alpha = 0$ deg, $Re_\infty = 0.50\times10^6$/ft

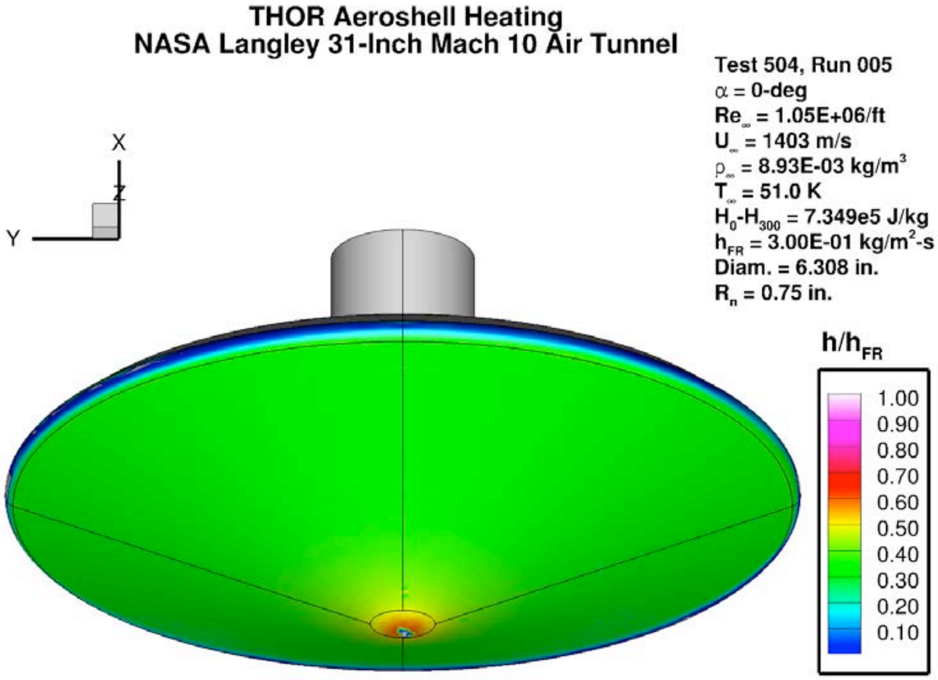

Figure 82. Test 504, Run 05 heating data: $M_\infty = 10$, $\alpha = 0$ deg, $Re_\infty = 1.05\times10^6$/ft.

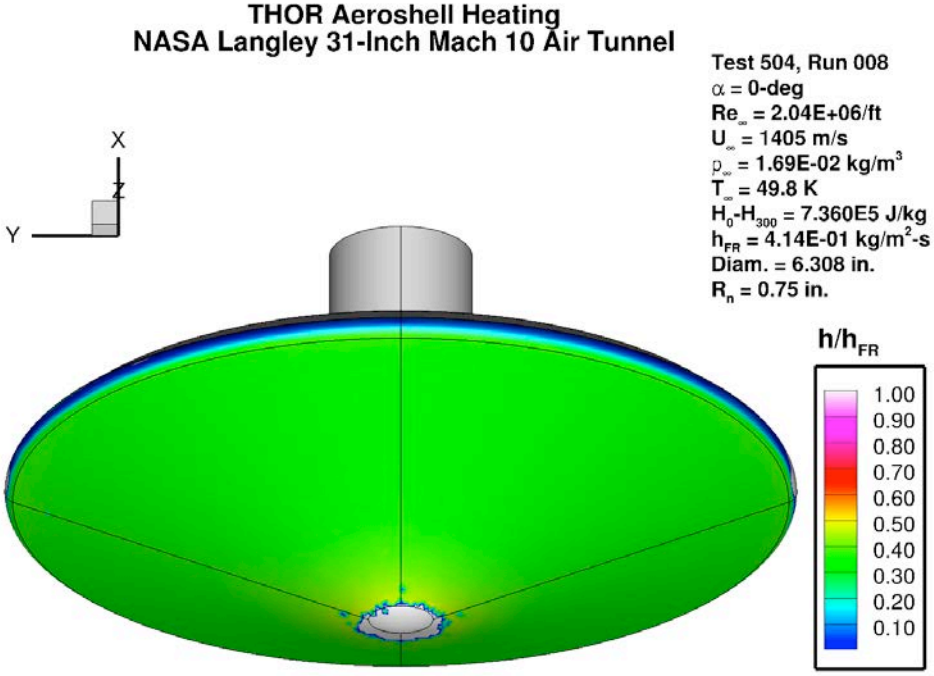

Figure 83. Test 504, Run 08 heating data: M_∞ = 10, α = 0 deg, $Re_\infty = 2.04\times10^6$/ft.

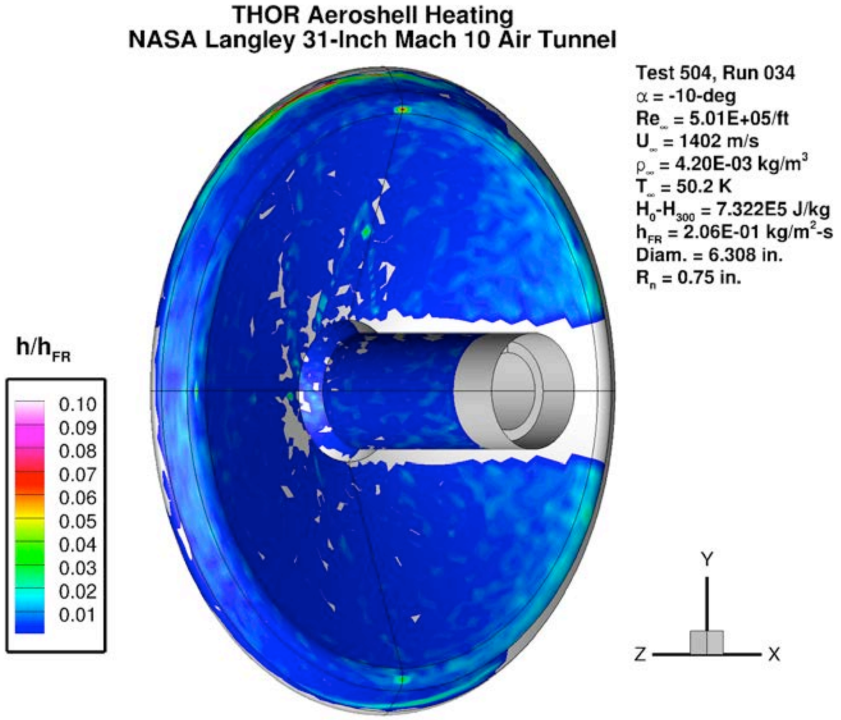

Figure 84. Test 504, Run 34 heating data: M_∞ = 10: $\alpha = -10$ deg, $Re_\infty = 0.50\times10^6$/ft.

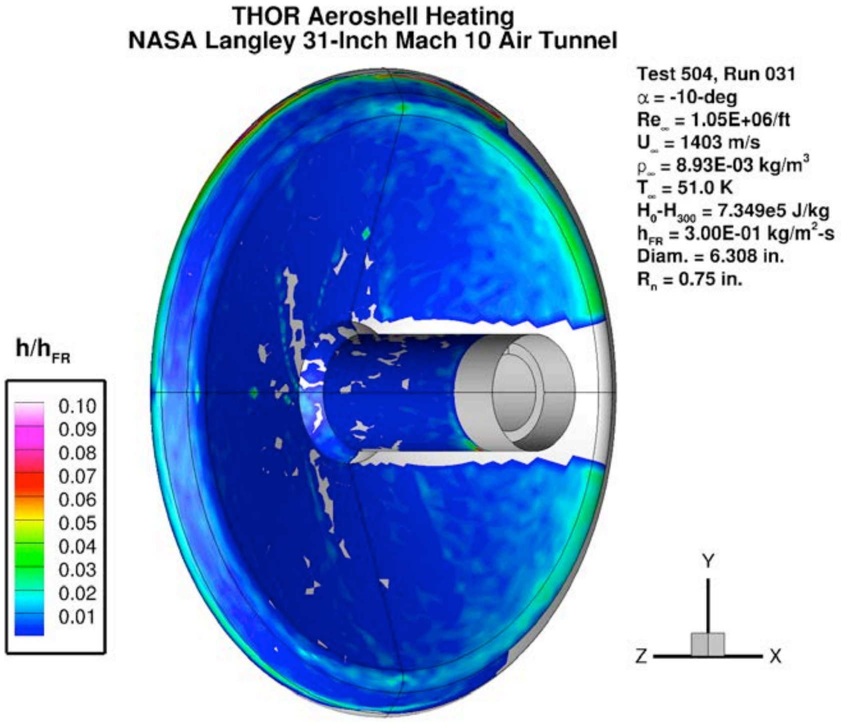

Figure 85. Test 504, Run 31 heating data: M_∞ = 10, $\alpha = -10$ deg, $Re_\infty = 1.05\times10^6$/ft.

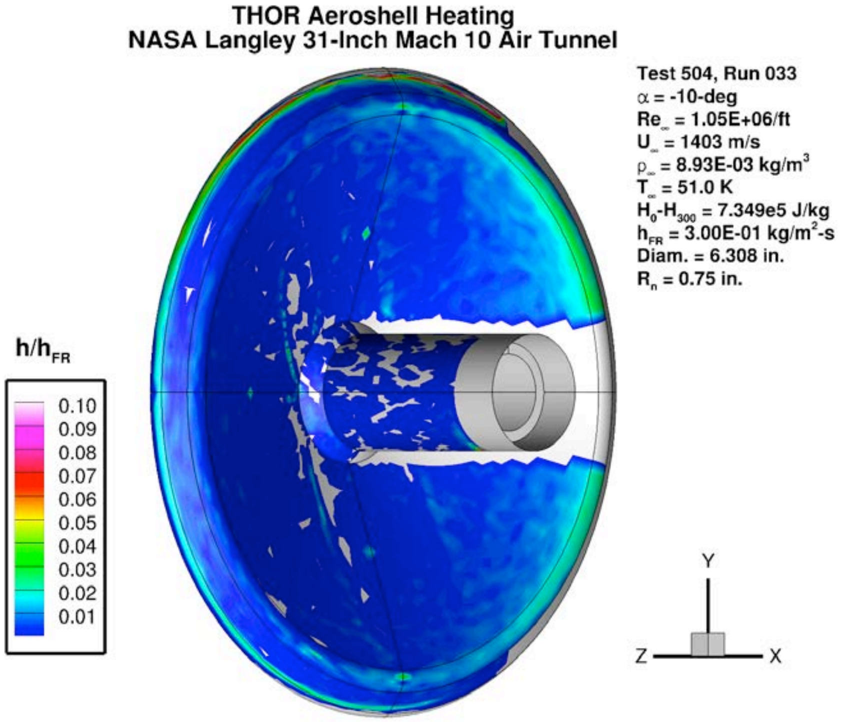

Figure 86. Test 504, Run 33 heating data: M_∞ = 10, α = –10 deg, $Re_\infty = 1.05\times10^6$/ft.

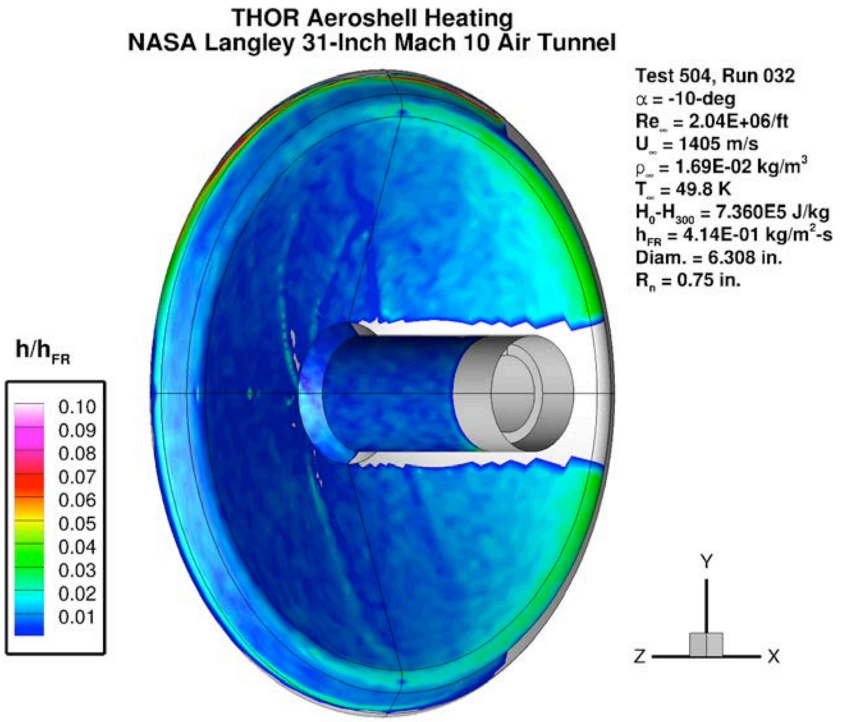

Figure 87. Test 504, Run 32 heating data: M_∞ = 10, α = –10 deg, $Re_\infty = 2.04\times10^6$/ft.

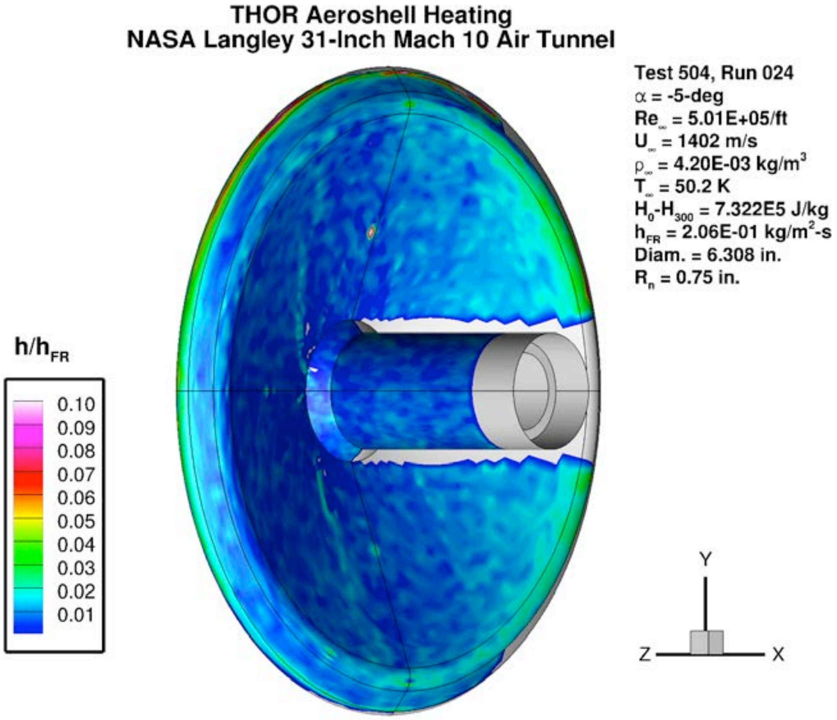

Figure 88. Test 504, Run 24 heating data: M_∞ = 10, α = –5 deg, $Re_\infty = 0.50\times10^6$/ft.

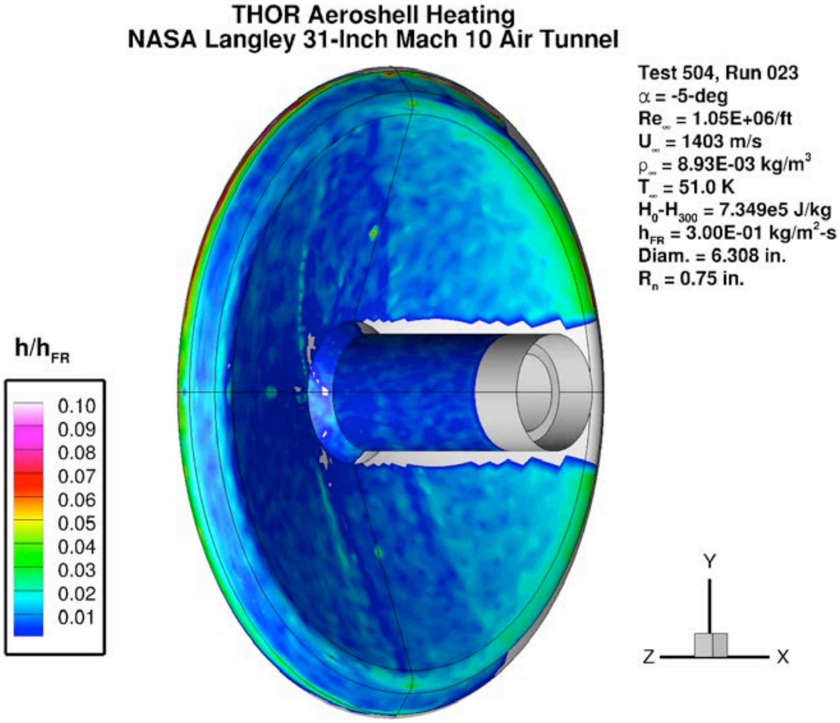

Figure 89. Test 504, Run 23 heating data: M_∞ = 10, α = –5 deg, $Re_\infty = 1.05\times10^6$/ft.

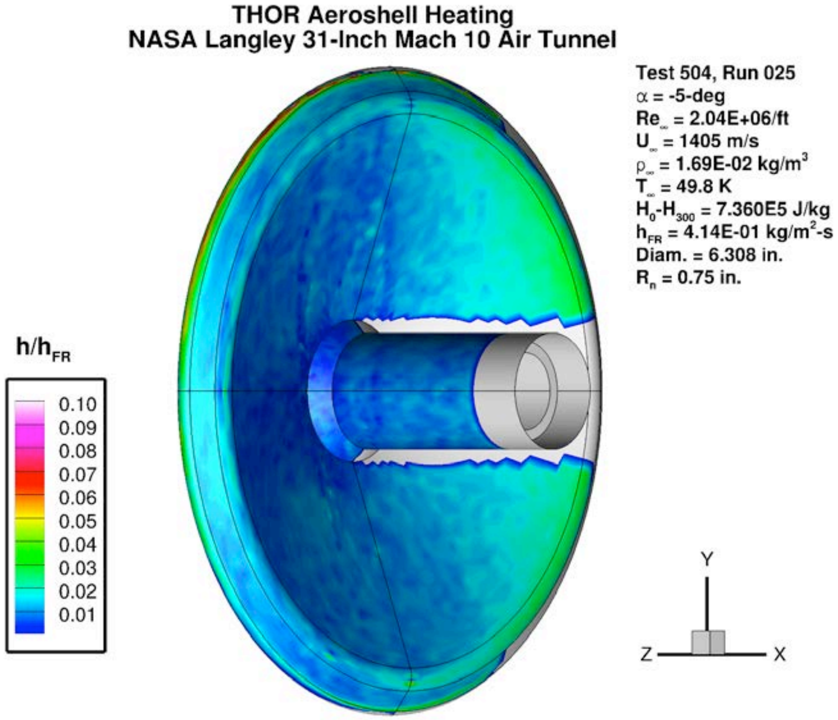

Figure 90. Test 504, Run 25 heating data: M_∞ = 10, α = –5 deg, $Re_\infty = 2.04\times10^6$/ft.

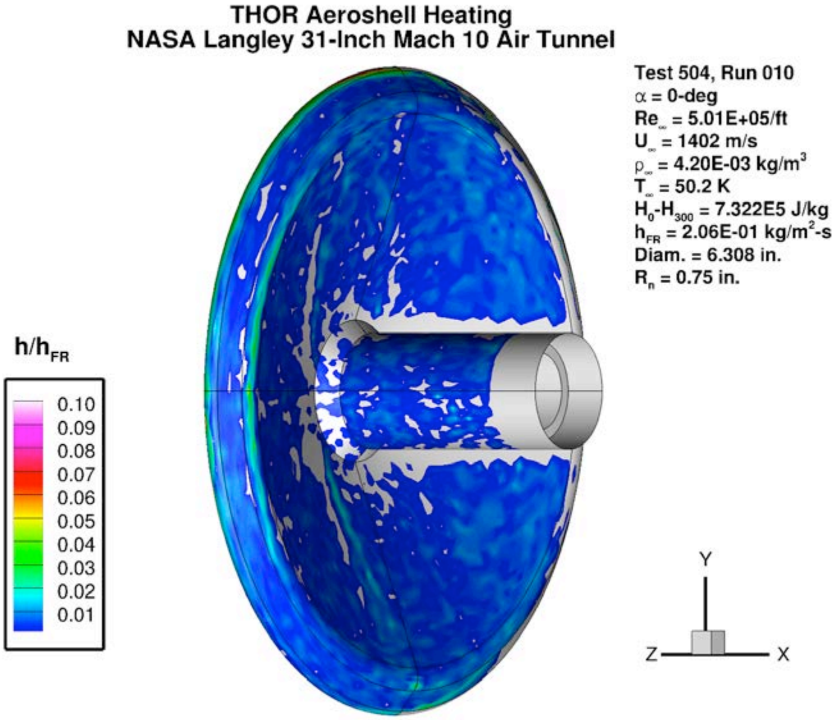

Figure 91. Test 504, Run 10 heating data: M_∞ = 10, α = 0 deg, $Re_\infty = 0.50\times10^6$/ft.

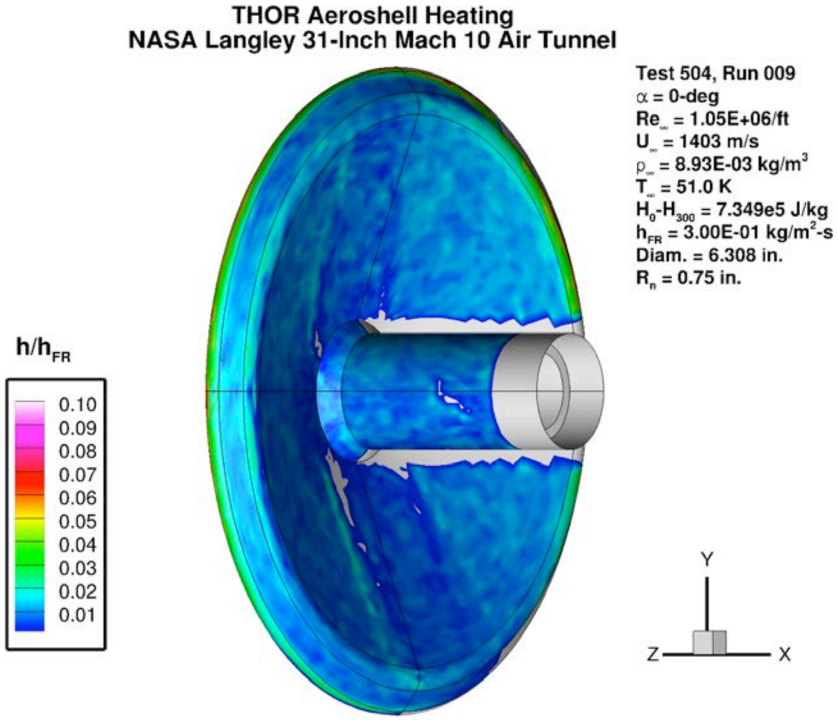

Figure 92. Test 504, Run 09 heating data: $M_\infty = 10$, α = 0 deg, $Re_\infty = 1.05 \times 10^6$/ft.

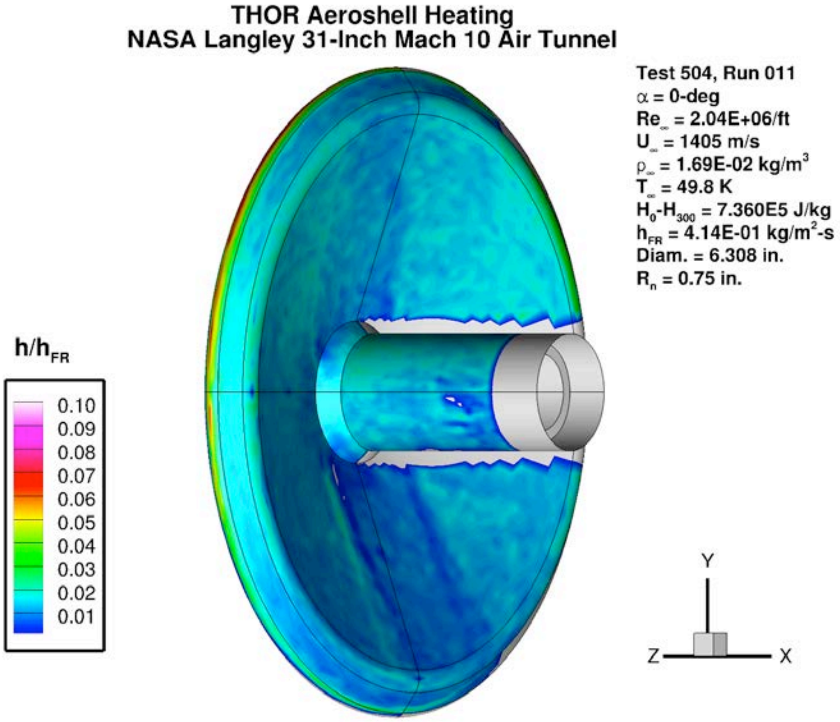

Figure 93. Test 504, Run 11 heating data: $M_\infty = 10$, α = 0 deg, $Re_\infty = 2.04 \times 10^6$/ft.

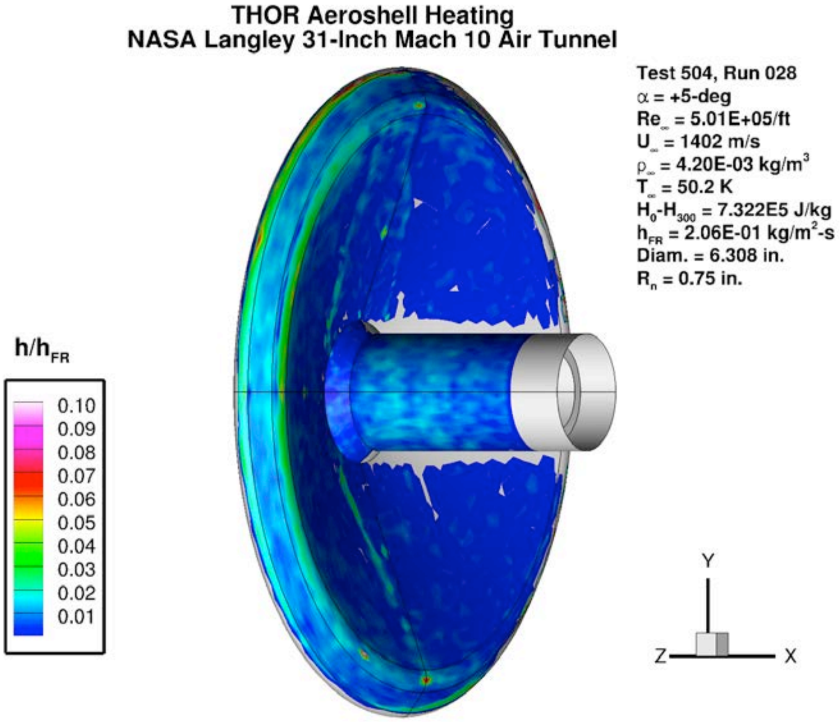

Figure 94. Test 504, Run 28 heating data: M_∞ = 10, α = +5 deg, $Re_\infty = 0.50\times10^6$/ft.

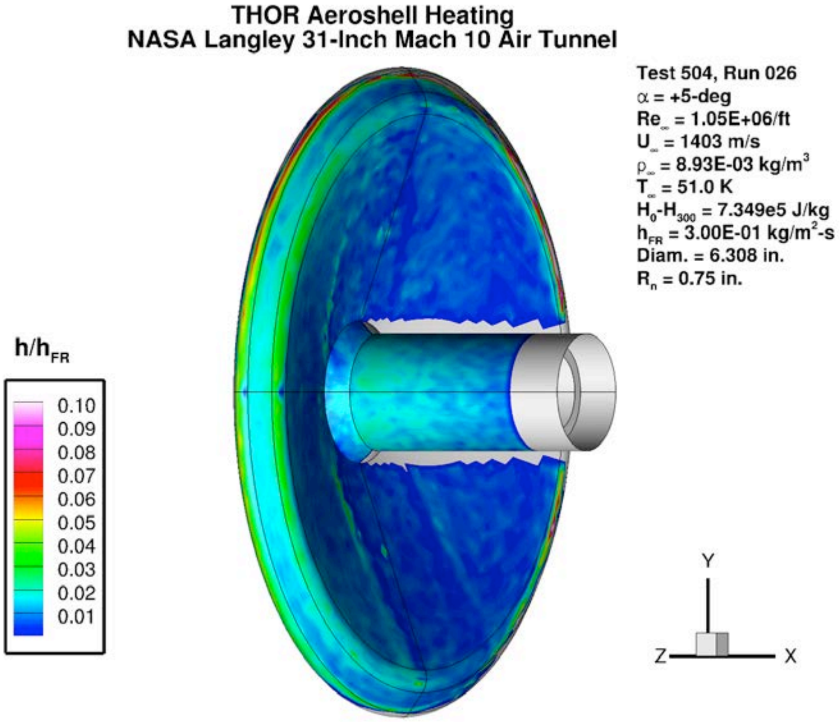

Figure 95. Test 504, Run 26 heating data: M_∞ = 10, α = +5 deg, $Re_\infty = 1.05\times10^6$/ft.

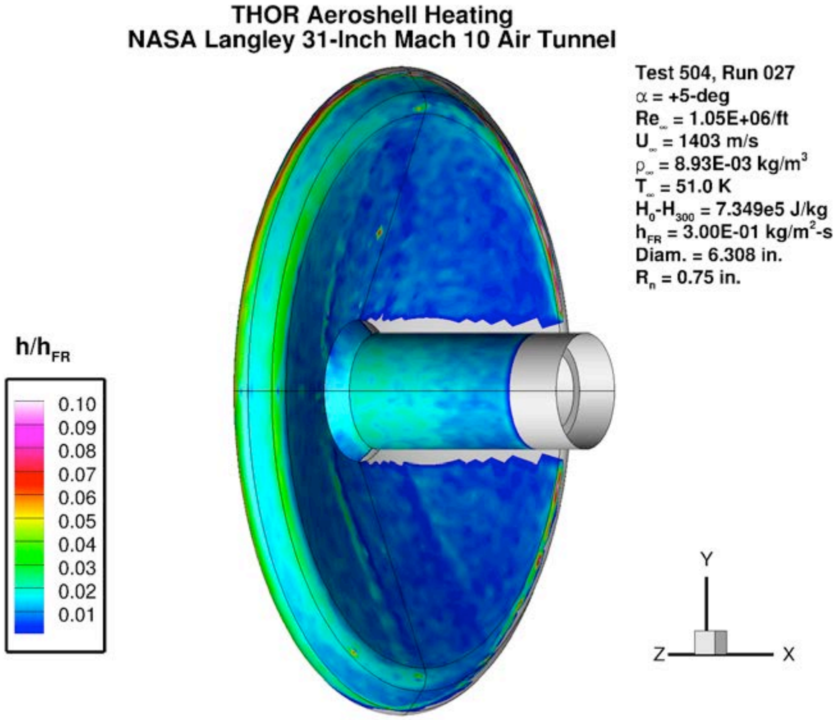

Figure 96. Test 504, Run 27 heating data: M_∞ = 10, α = +5 deg, $Re_\infty = 1.05\times10^6$/ft.

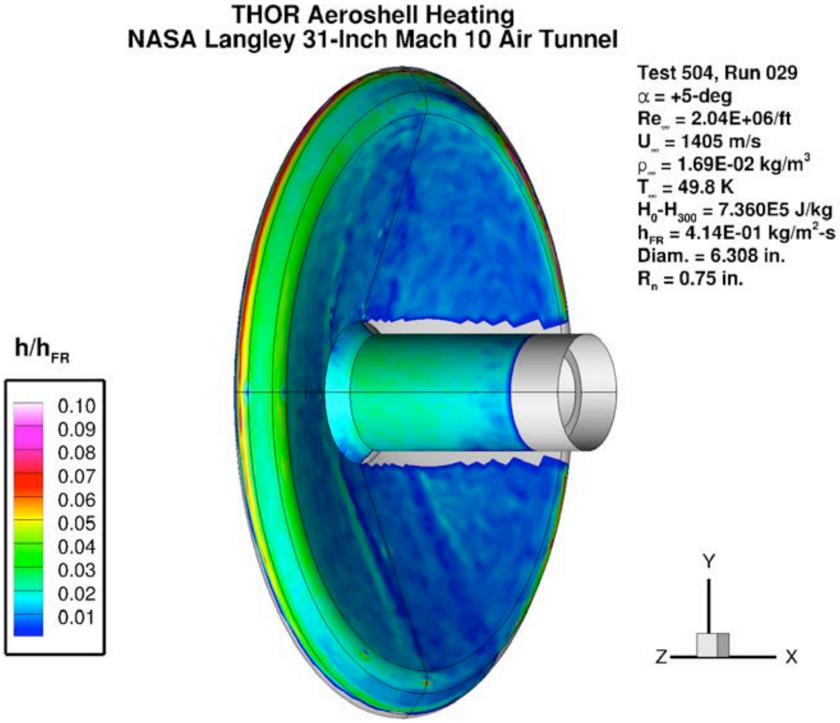

Figure 97. Test 504, Run 29 heating data: M_∞ = 10, α = +5 deg, $Re_\infty = 2.04\times10^6$/ft.

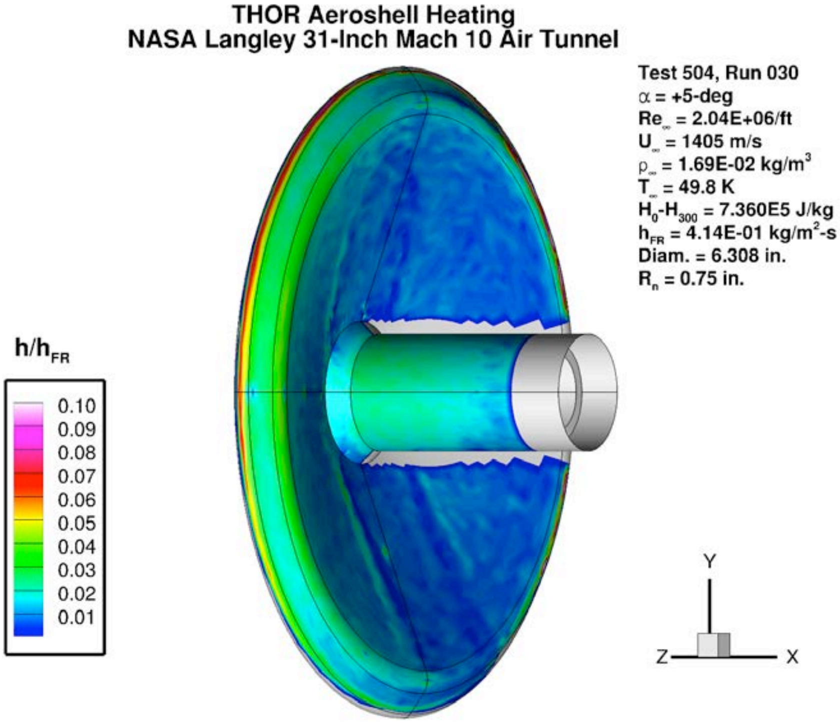

Figure 98. Test 504, Run 30 heating data: $M_\infty = 10$, $\alpha = +5$ deg, $Re_\infty = 2.04\times10^6$/ft.

Appendix B. Mach 6 Global Heating Images

Global heating images from Test 7002 in the 20-Inch Mach 6 Air Tunnel are presented in this appendix in Figure 99 through Figure 111.

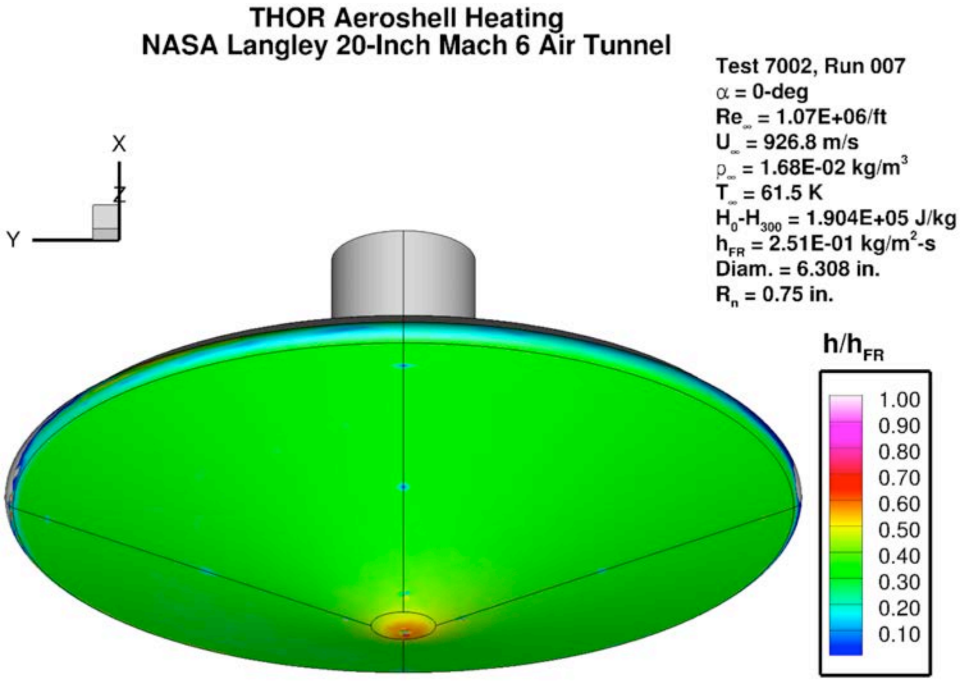

Figure 99. Test 7002, Run 07 heating data: M_∞ = 6, α = 0 deg, $Re_\infty = 1.07\times10^6$/ft.

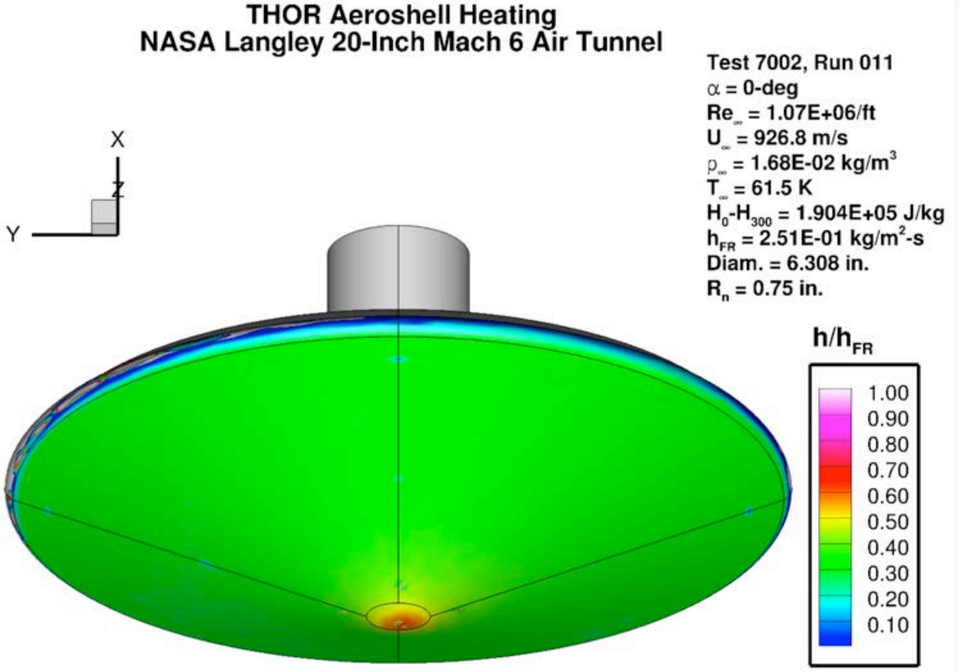

Figure 100. Test 7002, Run 11 heating data: M_∞ = 6, α = 0 deg, $Re_\infty = 1.07\times10^6$/ft.

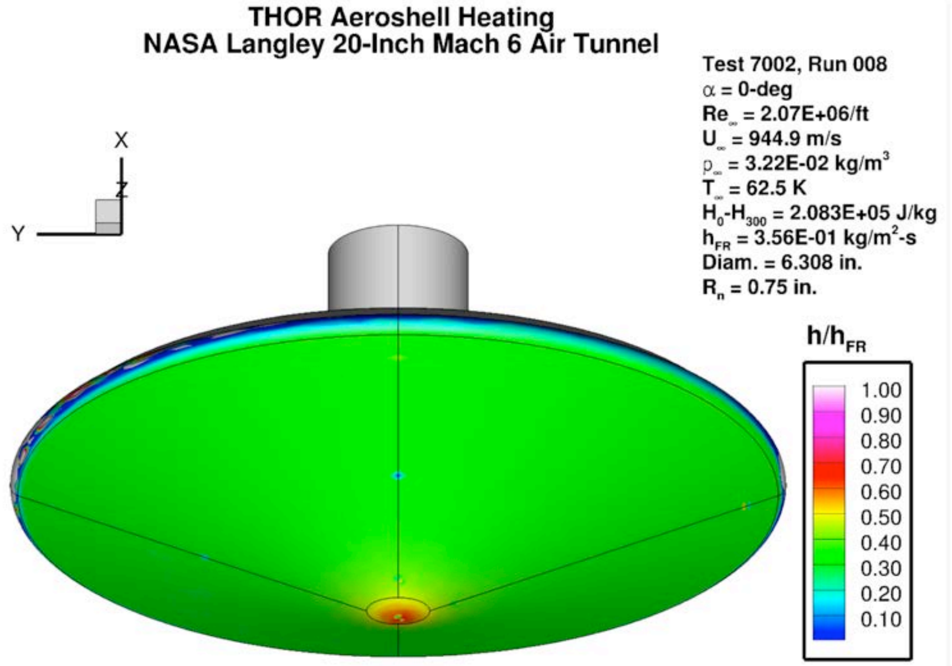

Figure 101. Test 7002, Run 08 heating data: M_∞ = 6, α = 0 deg, $Re_\infty = 2.07\times10^6$/ft.

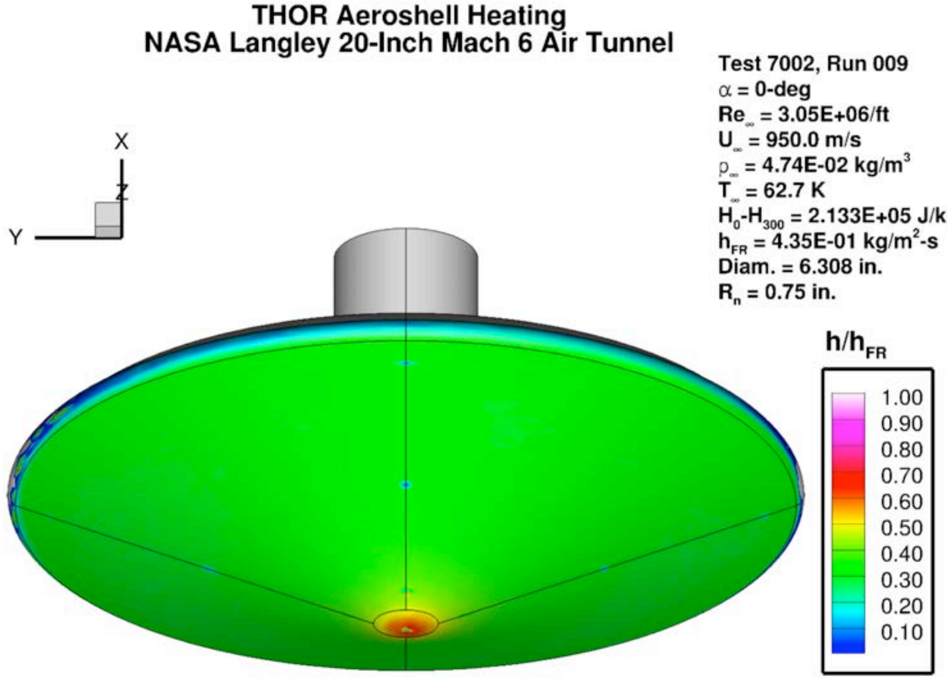

Figure 102. Test 7002, Run 09 heating data: M_∞ = 6, α = 0 deg, $Re_\infty = 3.05\times10^6$/ft.

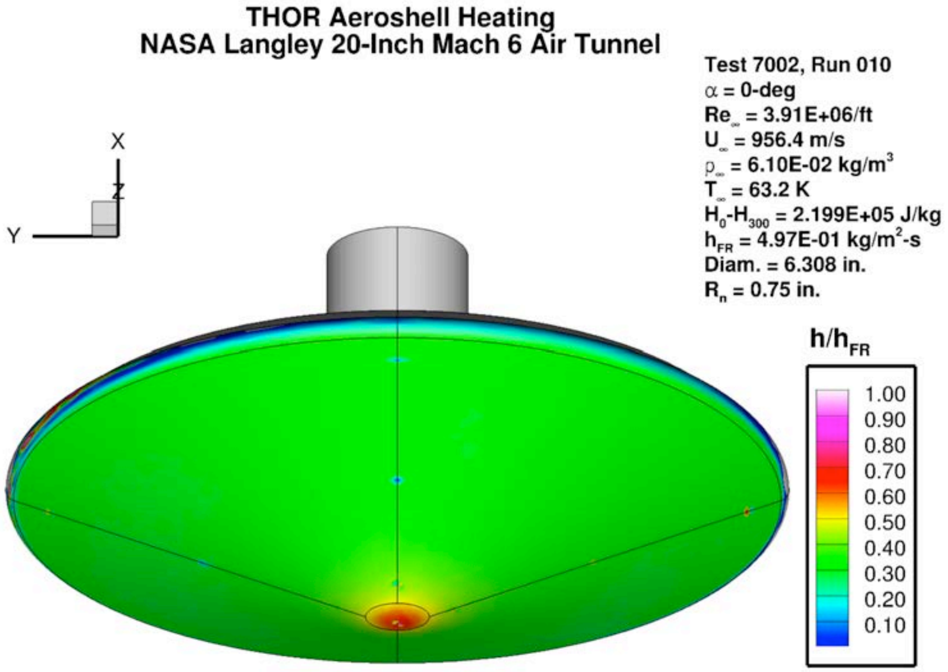

Figure 103. Test 7002, Run 10 heating data: $M_\infty = 6$, α = 0 deg, $Re_\infty = 3.91\times10^6$/ft.

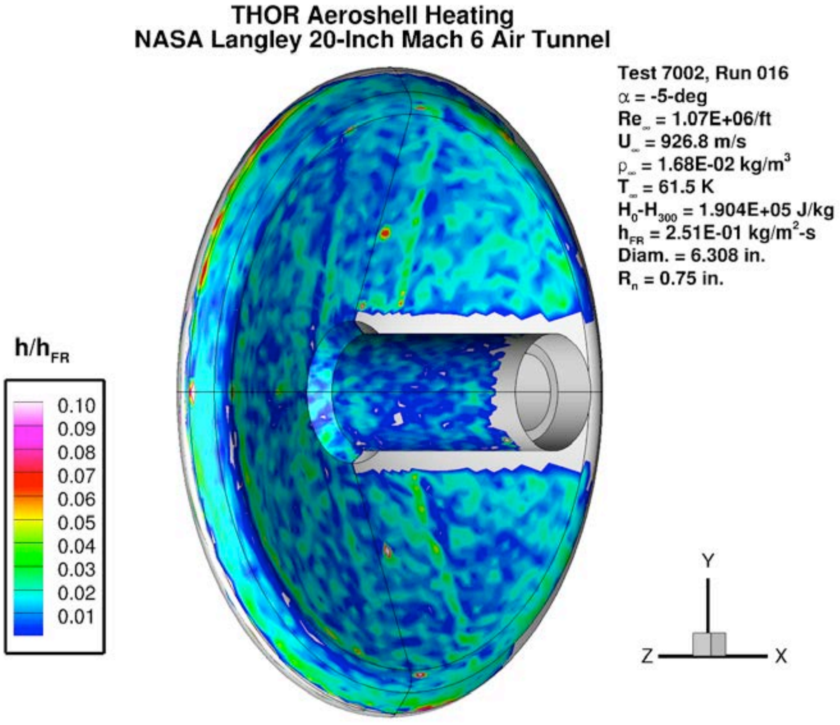

Figure 104. Test 7002, Run 16 heating data: $M_\infty = 6$, $\alpha = -5$ deg, $Re_\infty = 1.07\times10^6$/ft.

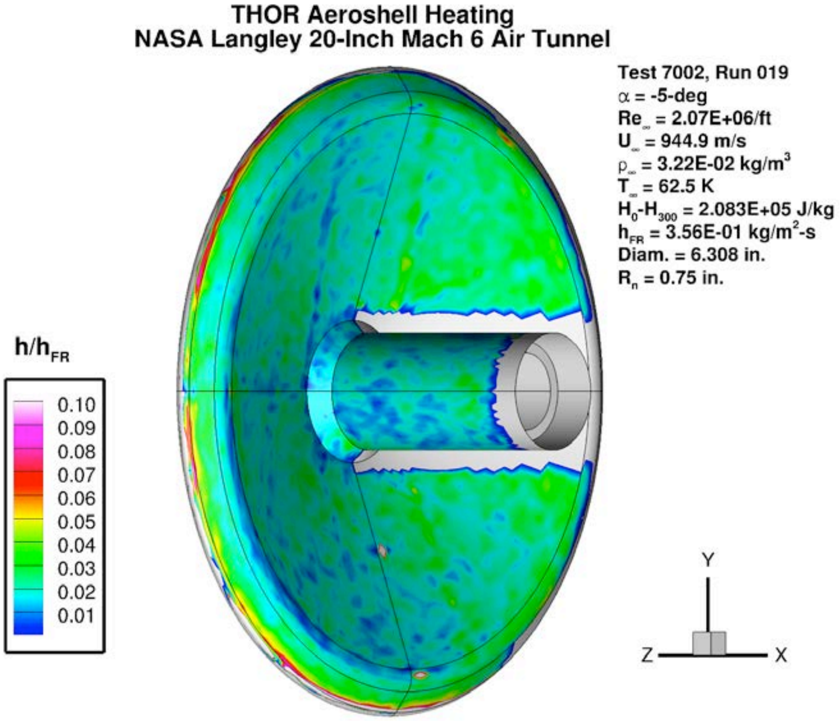

Figure 105. Test 7002, Run 19 heating data: $M_\infty = 6$, $\alpha = -5$ deg, $Re_\infty = 2.07\times10^6$/ft.

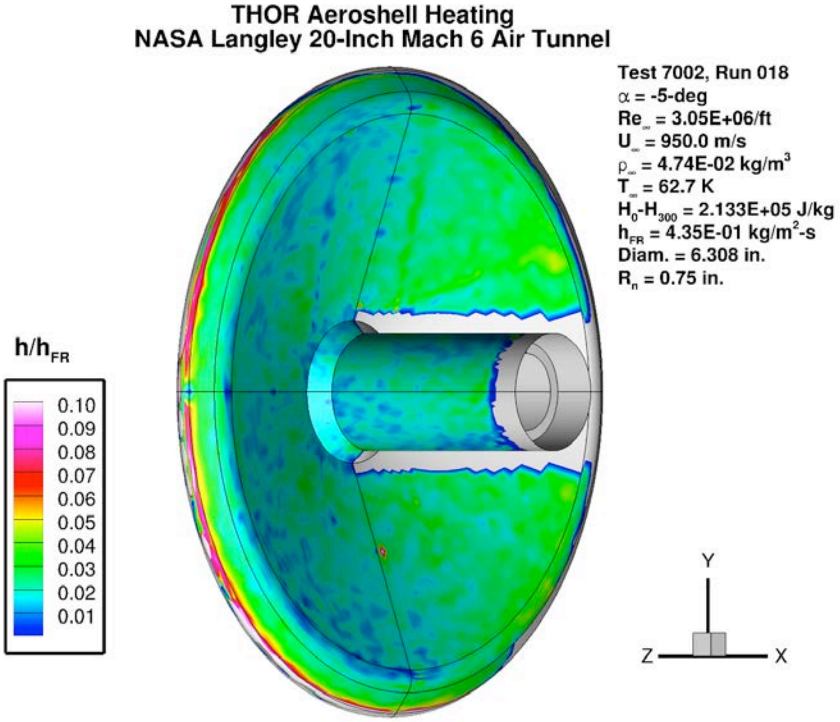

Figure 106. Test 7002, Run 18 heating data: M_∞ = 6, α = –5 deg, $Re_\infty = 3.05\times10^6$/ft.

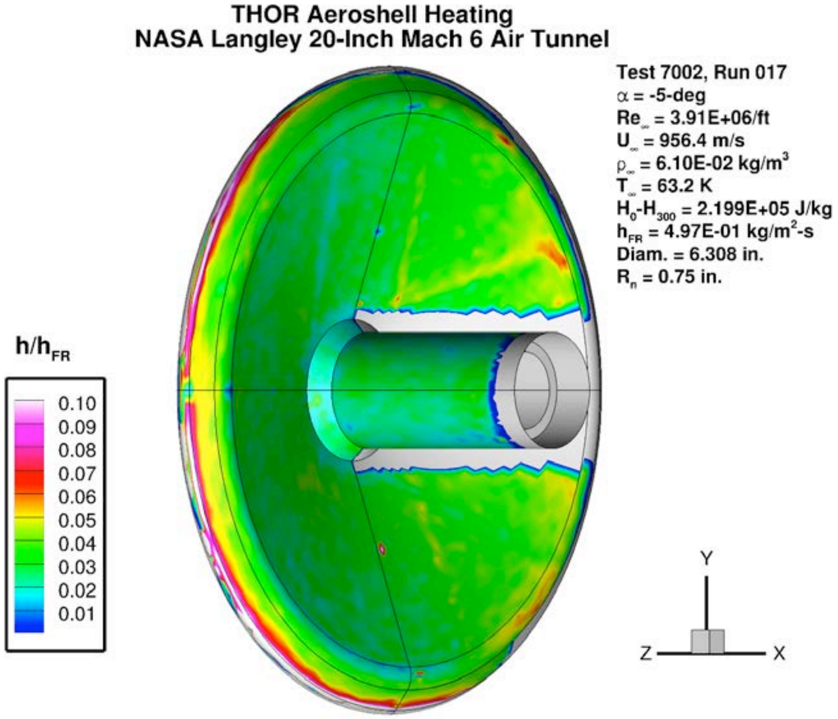

Figure 107. Test 7002, Run 17 heating data: M_∞ = 6, α = –5 deg, $Re_\infty = 3.91\times10^6$/ft.

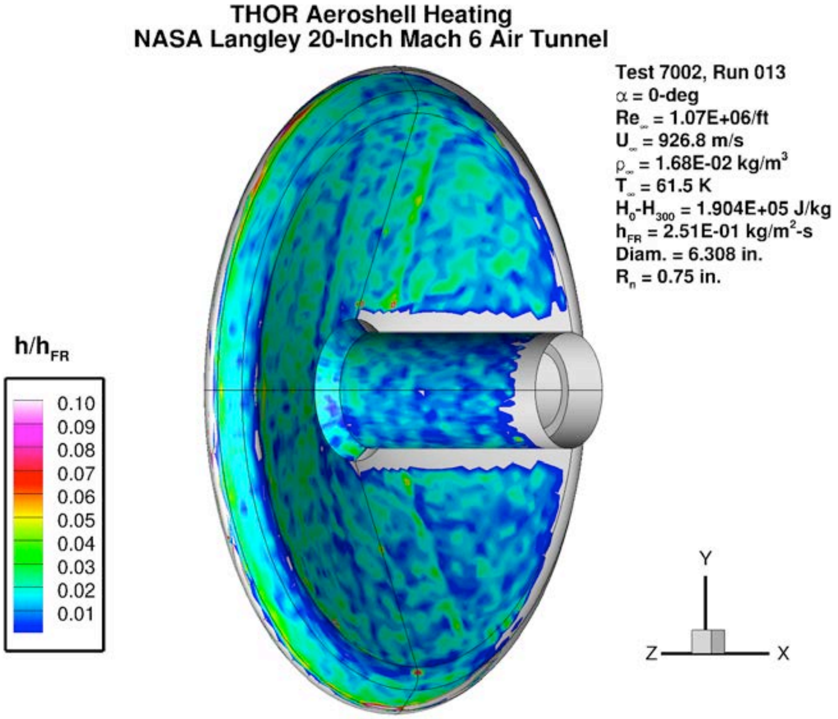

Figure 108. Test 7002, Run 13 heating data: $M_\infty = 6$, $\alpha = 0$ deg, $Re_\infty = 1.07\times10^6$/ft.

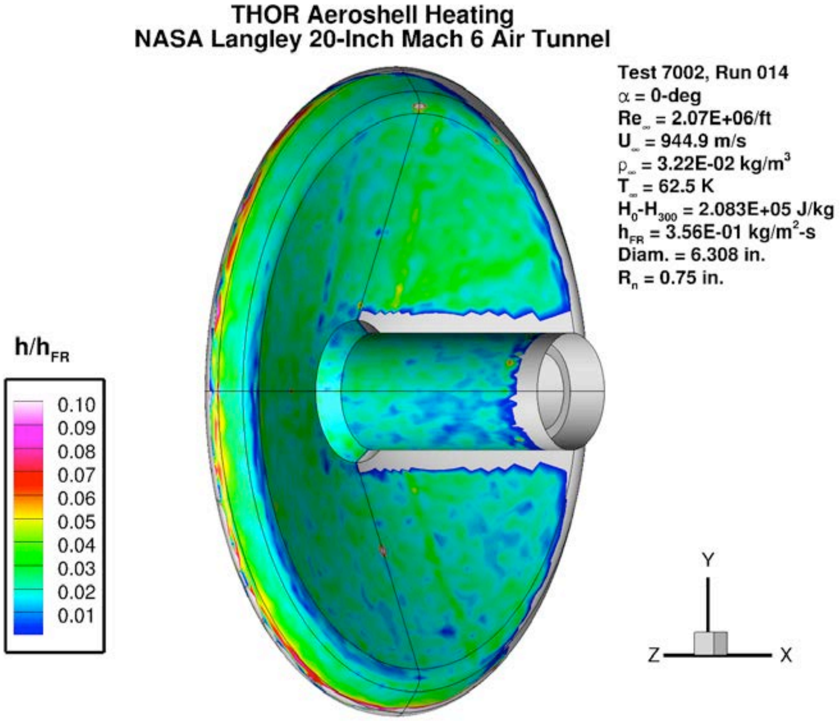

Figure 109. Test 7002, Run 14 heating data: $M_\infty = 6$, $\alpha = 0$ deg, $Re_\infty = 2.07\times10^6$/ft.

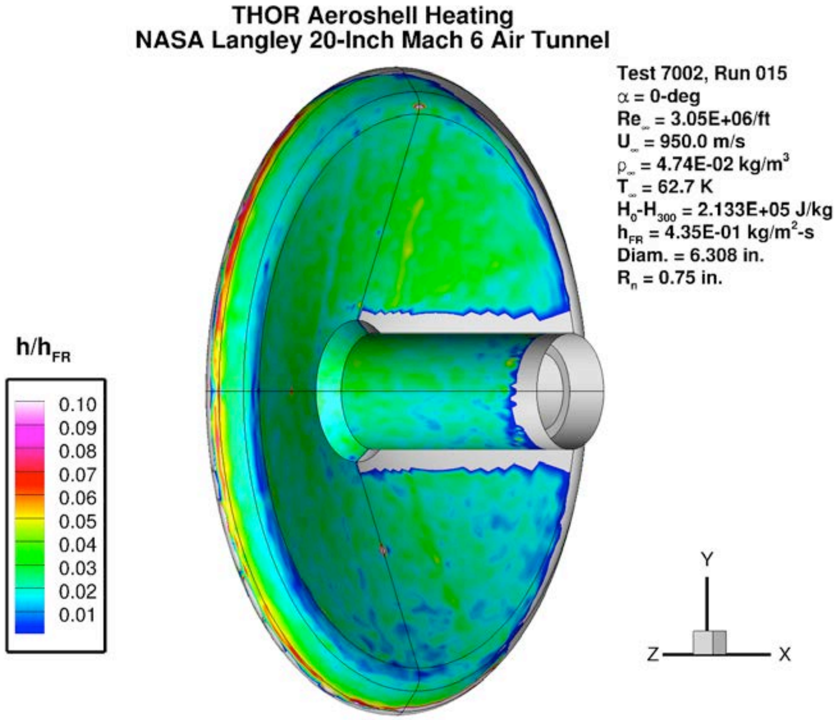

Figure 110. Test 7002, Run 15 heating data: M_∞ = 6, α = 0 deg, $Re_\infty = 3.05\times10^6$/ft.

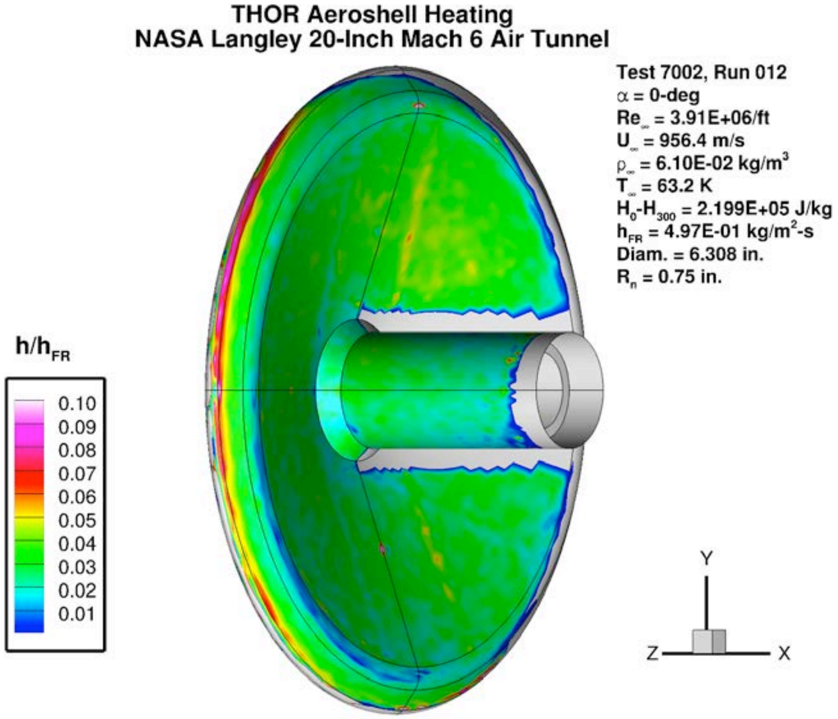

Figure 111. Test 7002, Run 12 heating data: M_∞ = 6, α = 0 deg, $Re_\infty = 3.91\times10^6$/ft.

REPORT DOCUMENTATION PAGE

Form Approved
OMB No. 0704-0188

1. REPORT DATE *(DD-MM-YYYY)*
01- 03 - 2017

2. REPORT TYPE
Technical Publication

3. DATES COVERED *(From - To)*

4. TITLE AND SUBTITLE

Experimental Study of Convective Heating on the Back Face and Payload of a Hypersonic Inflatable Aerodynamic Decelerator (HIAD) Aeroshell

5a. CONTRACT NUMBER

5b. GRANT NUMBER

5c. PROGRAM ELEMENT NUMBER

5d. PROJECT NUMBER

5e. TASK NUMBER

5f. WORK UNIT NUMBER
630154.02.07

6. AUTHOR(S)

Hollis, Brian R.; Berry, Scott A.; Hollingsworth, Kevin E.; Wright, Shelia A.

7. PERFORMING ORGANIZATION NAME(S) AND ADDRESS(ES)

NASA Langley Research Center
Hampton, VA 23681-2199

8. PERFORMING ORGANIZATION REPORT NUMBER
L-20785

9. SPONSORING/MONITORING AGENCY NAME(S) AND ADDRESS(ES)

National Aeronautics and Space Administration
Washington, DC 20546-0001

10. SPONSOR/MONITOR'S ACRONYM(S)
NASA

11. SPONSOR/MONITOR'S REPORT NUMBER(S)
NASA-TP-2017-219581

12. DISTRIBUTION/AVAILABILITY STATEMENT

Unclassified - Unlimited
Subject Category 34
Availability: NASA STI Program (757) 864-9658

13. SUPPLEMENTARY NOTES

14. ABSTRACT

A wind tunnel test program has been conducted to obtain convective heat transfer data to support the design of flexible thermal protection systems for future NASA Hypersonic Inflatable Aerodynamic Decelerator flight tests. Wind tunnel testing was conducted at Mach 6 and Mach 10 at unit Reynolds numbers from 0.5×106/ft to 3.9×106/ft on a 6.3088 in diameter aeroshell model. Global heating data were obtained through phosphor thermography on the aeroshell back face and payload, as well as on the aeroshell front face. For all test conditions, laminar flow was produced on the aeroshell front face, while the separated wake shear layer and aeroshell back-face boundary layer were transitional or turbulent. Along the leeward centerline of the aeroshell back face and payload centerbody, heating levels increased with both free stream Reynolds number and angle of attack. The Reynolds number dependency was due to increasing strength of wake turbulence with Reynolds number. The angle-of-attack dependency was due to movement of the wake-vortex reattachment point on the aeroshell back face. The maximum heating levels on the aeroshell back face and payload were approximately 5% to 6%, respectively, of the aeroshell front-face stagnation point.

15. SUBJECT TERMS

HIAD; Heat-transfer; Hypersonic; Iinflatable aeroshell; Wake flow; Wind tunnel

16. SECURITY CLASSIFICATION OF:			17. LIMITATION OF ABSTRACT	18. NUMBER OF PAGES	19a. NAME OF RESPONSIBLE PERSON
a. REPORT	b. ABSTRACT	c. THIS PAGE			STI Help Desk (email: help@sti.nasa.gov)
U	U	U	UU	115	19b. TELEPHONE NUMBER *(Include area code)* (757) 864-9658